UNIVERSIDADE DE LISBOA
FACULDADE DE CIÊNCIAS
DEPARTAMENTO DE FÍSICA

Wind measurements in Saturn's atmosphere using Doppler velocimetry techniques from ground-based observations

Mestrado em Física
Especialização em Astrofísica e Cosmologia

Miguel Gonçalves Simões Silva

Dissertação orientada por:
Pedro Mota Machado

2016

Acknowledgments

Accomplish a master degree in Astrophysics is not an easy task and certainly a little harder than some might think. The fact that I choose to do my dissertation about a new and promising approach, being one of the pioneers on it, certainly made the pressure to succeed grow up. Study the winds and atmosphere behavior of another planet has its cons and its tricks. During the past 9 months I stumbled at many walls and challenges, some of them I had to seek help from a couple friends who had more programming abilities. So, I had to improve a lot of my skills, put my knowledge to the test and even change the way I perceived investigation work. I am very fortunate to have some pillars that gave me support and strength to go trough this quest that I joined.

I am grateful to my supervisor Pedro Machado, that has been a reference and an example of dedication and seriousness as a scientist, always preserving an ethical and responsible attitude. I learned a lot, and I thank him for his patience and availability. It was a privilege working with someone that loves his job ans shares is passion and enthusiasm with me and vice versa. I believe that this experience will be extremely valuable in future works.

I also have to give a special thank to all my teachers from high-school to university that always saw a great potential in my and tried to persuade my to become an increasing better student, a hard worker and, at the same time, a good citizen, a humble, honest, kind person to everyone who deserves my friendship and respect... a Man.

This wouldn't have completed this journey safely and successfully without the unconditional support and motivation of my mother, sister, grandparents, uncles ans cousins, my dear family that I shall forever cherish. My family is very proud of the person I have become. This extends to all my closest friends from high school and university, some of them have been working on their dissertations in the current year too, that have motivated myself to

give my best, ready to listen my good and bad moments and, whenever was possible, kidnapped me to go out and have the special fun that only those friends for life can give.

At last but not at least, I feel blessed to have that one person, who above all, gave me unconditional will to work, joy and love, my boyfriend André, who has been my soul company and know the best my failures and successes, my "Eureka!" moments and my saddest days. He, more than everyone else, never doubted of myself and my capabilities and fills me with certainty that I will get where I want, one step at a time and I wish that I can be by my side on the future landmarks of my life, remaining true yo myself, and I also wish to be there for his bright future, yet to unveil.

"Let the future tell the truth, and evaluate each one according to his work and accomplishments. The present is theirs; the future for which I have really worked, is mine. "

Nikola Tesla

Abstract

The thesis presents ground-based Doppler velocimetry measurements of the zonal winds of Saturn, based on observations carried out with the Ultraviolet and Visual Echelle Spectrograph (UVES) at ESO's Very Large Telescope. Using Doppler-shifted Fraunhofer lines from the solar spectrum, this high resolution spectrograph (R $\sim$ 100,000) allows to measure the velocity of Saturn's cloud layer with a precision of about 5 ms^{-1}. Under the assumption of predominantly zonal flow, this method allows the simultaneous direct measurement of the zonal velocity across a range of latitudes and local times.

The technique, based on long slit spectroscopy, combined with the observations' high spatial resolution, can provide the first ground-based characterization of the latitudinal profile of zonal wind in the atmosphere of Saturn (this is an ongoing work), as well as new constraints on wind variations with local time.

I retrieved the Doppler velocities associated to the Doppler shifts on the spectra, using the Absolute Astronomical Accelerometry (Connes , 1985; Machado et al., 2012). The breakthrough that I aim to achieve with this research project is to take advantage of the instantaneous winds retrieved with Doppler velocimetry technique, in order to measure spatial and time variability/evolution of the winds in Saturn's atmosphere, namely its zonal circulation, more specifically, obtain the latitudinal profile of the winds and the variability of the wind as a function of the local time. In addition, I hope to detect and constrain the spatial and time evolution of atmospheric planetary waves and storms.

Throughout the complex process, I had to carefully treat the data according to the spectroscopy analysis that I became familiar with. That included de-bias and flat-field the data images, compute the master bias and master flats for each set of observations, computed the average of the three spectra obtained at each slit offset position, and I built a dispersion function based on spectra from a Th-Ar lamp, in order to obtain a high-precision wavelength

calibration. Then, I retrieved the 1D high resolution spectra from the raw *echellogramme*.

I re-programmed the scripts from the pipeline, previously used for Venus atmosphere dynamical studies, in order to adapt them to the geometry of this study observations and to the slit's active window, towards the removal of the pixels that will be affected by Saturn's rings. I used spherical geometry in order to de-project the retrieved radial Doppler velocities from the line-of-sight from the Earth observer and to navigate the planetary observed disk, so I could obtain precise locations of latitude and sub-Earth longitude.

I modeled the overall measured Doppler shifts that include planetary rotation velocity, wind velocity and Doppler contributions from the planetary absorption by methane, ammonia and hydrogen, in order to obtain a first order qualitative approximation of the retrieved overall velocities, where is clear the relevant differences between latitudinal System I and II on Saturn. For removing Saturn's rotational velocity, and regarding that, along the slit, there is a significant range of latitudes covered, I used the rotation rate of the planet's magnetic field (System III), affected by the co-sine of the latitude at each pixel position over the planet.

I also evaluated the spurious contribution of the Young effect on the retrieved velocities and, as I suspected, this wasn't relevant for the geometry of our observations.

I calculated the weighted average (where the weight coefficients were the inverse of the variance of each retrieved Doppler velocity) for the pixels along each slit's position and for each detector (MIT and EEV), regarding that they cover different wavelength ranges, and so, have different optical depths, and are differently affected by methane, ammonia and hydrogen absorption lines.

Future Work This is still an on-going work, so, in the next steps, I will work out how to subtract the spectra of the rings from the Saturn's spectra, obtaining a spectra with only Fraunhofer lines; I will study the inclination of the spectral lines, the contributions from chemical species as methane, ammonia and hydrogen in the retrieved high-resolution spectra and sound different pressure levels, in order to constrain the vertical wind sheer.

Keywords: Saturn, Atmospheres, Dynamics, Observational Techniques, Zonal Winds, Spectroscopy, Doppler Velocimetry.

Resumo em Português

O projecto desenvolvido e aqui apresentado, centra-se no esforço para caracterizar a dinâmica atmosférica de Saturno, utilizando observações realizadas a partir do solo, complementando assim as medições obtidas pela missão Cassini. Este mestrado foi realizado sob a orientação do Doutor Pedro Mota Machado, investigador do Instituto de Astrofísica e Ciências do Espaço (IA). Os trabalhos foram realizados no antigo Centro de Astronomia e Astrofísica da Universidade de Lisboa (CAAUL), agora o pólo de Lisboa do Instituto de Astrofísica e Ciências do Espaço, localizado na Tapada da Ajuda.

Os trabalhos desenvolvidos ao longo da primeira fase do meu projecto de investgação basearam-se em observações efectuadas com o *Very Large Telescope (VLT)* do *ESO* (Observatório de La Silla - Paranal - Chile), associado ao espectrógrafo de alta resolução *Ultraviolet and Visual Echelle Spectrograph* (UVES). A partir dos espectros de alta resolução obtidos, foi aperfeiçoada a técnica de medição de ventos a partir dos desvios Doppler nas riscas espectrais da radiação absorvida pela camada de nuvens (a uma altitude onde a profundidade óptica atinge a unidade).

Neste trabalho utilizou-se um processo de medição directa dos ventos planetários baseado em espectroscopia de alta resolução na banda do visível, com comprimentos de onda entre 300 e 1100 nm, designado de velocimetria Doppler. Esta técnica foi originalmente sugerida e desenvolvida em (Connes , 1985) e mais recentemente aperfeiçoada e refinada para o caso do estudo da dinâmica atmosférica de Venus em Machado et al. 2012.

A fim de cobrir uma gama representativa de latitudes e longitudes foi utilizada uma configuração de fenda longa (0,3 segundos de arco de largura e 25 segundos de arco de comprimento). Obteve-se uma resolução espacial de aproximadamente 1100 km no centro do disco planetário. Foi usada uma configuração de observação com a fenda espectroscópica alinhada perpendicularmente relativamente ao eixo de rotação planetário, com a posição da

fenda inicialmente alinhada com um paralelo sobre o disco de Saturno. Para esta geometria foi possível fazer o cálculo directo da magnitude dos ventos zonais, velocidade instantânea, para cada latitude observada.

As observações das quais provieram os dados tratados realizaram-se entre os dias 18 de Abril e 3 de Maio de 2004. A escolha das datas das observações permitiu combinar a necessidade de maximizar o diâmetro angular de Saturno (resolução espacial sobre o disco planetário) e minimizar o ângulo de fase da observação.

A técnica, com base na espectroscopia de fenda longa combinada com a alta resolução espacial permitida pelo VLT, poderá proporcionar, pela primeira vez, a caracterização do perfil latitudinal do vento zonal na atmosfera de Saturno a partir de observações a partir da Terra. Permitirá também a realização de um mapa de ventos em Saturno, assim como a obtenção de novas restrições sobre a variabilidade do vento em função da hora local. O perfil de vento zonal obtido é consistente com medições anteriores realizadas pela sonda espacial Cassini, com base no seguimento de nuvens, introduzindo informação relevante sobre a variabilidade do vento em hora local e latitude (dado o carácter inovador das medições serem instantâneas e simultâneas ao longo de uma vasta região sondada).

O processo de tratamento dos dados provenientes do UVES foi feito com recurso a um pacote de scripts MATLAB (explicado em detalhe no Apêndice B) fornecido pelo Doutor Pedro Machado e que ele havia apereiçoado para o estudo da dinâmica atmosférica de Venus.

Ao longo deste complexo processo, eu tive de, cuidadosamente, tratar os dados de acordo com a análise espectroscópica com a qual me familiarizei. Tal incluiu o processo de "be-bias" e "flat-field" das imagens, obter of ficheiros de "master bias" e "master flat" para cada conjunto de observações, calcular a média dos três espectros obtidos para cada configuração da posição da slit, e construir uma função de dispersão baseada no espectro de uma lâmpada de Tório-Árgon, por forma a conseguir uma calibração em comprimento de onda de grande precisão. Daí, obtive o espectro de alta resoluç ao, a uma dimensão, a partir do *echellogramme* puro.

De seguida, reprogramei os scripts previamente usados para o estudo da atmosfera de Vénus, de modo a adaptá-los à geometria das observações em estudo e ao tamanho da janela activa da slit, com vista a remover os pixéis que terão sido afetados pelo sistema de anéis de Saturno. Utilizei geometria esférica com ista a efectuar a de-projeção das velocidades radiais Doppler

obtidas, em relação à linha de visão do observador terrestre e procedei à navegação do disco planetário, com vista a obter as localizações precisas da latitude e da longitude sub-terrestre.

Modelei os desvios de Doppler globais, que incluiam a velocidade de rotação planetária, a velocidade dos ventos e as contribuições Doppler provenientes da absorção planetária de compostos químicos como metano, amónia e hidrogénio, com o intuito de obter uma aproximação qualitativa de primeira ordem das velocidades generalizadas, onde é claro que existem diferenças significativas entre as latitudes dos Sistemas I e II em Saturno. Para poder remover a velocidade rotacional de Saturno e tendo em conta que, ao longo da slit, temos uma banda de latitudes significativa que é abrangida, usei a velocidade de rotação do campo magnético do planeta (Sistema III), afetada pelo co-seno da latitude da posição de cada pixel em todo a parte disco do planeta que foi coberta.

Eu avaliei igualmente a contribuição espúria do Efeito de Young nas velocidades Doppler obtidas e, tal como suspeitei, não se mostrou relevante para os dados tratados. Calculei também a média ponderada (na qual os coeficientes de ponderação eram o inverso da variância de cada velocidade Doppler obtida) para os pixéis ao longo de cada slit e para cada detetor (MIT e EEV), tendo em atenção que estes sondam diferentes gamas de comprimentos de onda, e portanto, diferentes profundidades ópticas, e que são afetados de modos diferentes pelas riscas de absorção das moléculas acima mencionadas.

Os resultados obtidos por melhor ajuste revelam magnitudes para as velocidades Doppler que estão em concordância geral com resultados prévios de *cloud tracking* mais recentes. Nas etapas seguintes ter-se-á que quantificar e retirar os efeitos causados pelas riscas de metano e de amoníaco e as altitudes em que estes mais se fazem sentir nos dados recolhidos.

No mês de Abril do corrente ano participei na Assembleia Geral da *European Geosciences Union* (EGU), em Viena, onde, juntamente com o meu orientador, submeti e apresentei um poster no qual dispunha alguns dos resultados preliminares dos dados obtidos para as velocidades Doppler obtidas até à data da conferência. O *feedback* da comunidade científica presente foi bastante positivo, reconhecendo o potencial desta técnica de velocimetria Doppler para medir ventos instantâneos, constitiuindo igualmente uma ferramenta que poderá vir a ser utilizada no estudo dos exoplanetas.

Permanece essencial a necessidade de proceder à integração de medições de vento a differences altitudes, i.e. utilizando radiação de diferentes com-

primentos de onda, de modo a compreender melhor a dinâmica da atmosfera de Saturno e os fenómenos meteorológicos de curta e longa duração que nela decorrem.

Esta técnica pioneira apresenta perspectivas bastante promissoras, pelo que poderá permitirá a caracterização do vento zonal a nível latitudinal, em termos do seu perfil em função da hora local e da sua variabilidade espacial e temporal.

O trabalho futuro contemplará o estudo das velocidades do sistema de anéis de Saturno, a inclinação das linhas espectrais e as contribuições das espécies químicas (metano, amónia e hidrogénio) têm nos espectros de alta resolução conseguidos.

Contents

List of Figures

List of Tables

Chapter 1

Thesis Overview

1.1 Scientific Context

Throughout the past decades, the study of the Saturn's atmosphere has grown as a theme of major interest amongst the astrophysics scientific community. Yet, the last *in situ* measurements were taken from the Cassini probe, that arrived to its ring-moon system in 2004 ,and we still do not know very much about the planet's global circulation processes and the intensity of the zonal winds as a function of the latitude and local time. For the last years, astronomers have made many efforts to collect increasingly higher quality data using the top instruments installed in the best Earth-based telescopes that have been built to date.

A complete characterization of this dynamical phenomenon is crucial for understanding its driving mechanisms. The rationale for the Saturn observations is concentrated in two approaches: a) the complementarity with Cassini, thus providing an independent set of observations to compare results with; b) to monitor the time variability to better understand the dynamics of Saturn's zonal winds, which Sánchez-Lavega et al. 2003 have found to have changed strongly in the last decade.

1.2 Objectives

The main goals of this study are to investigate the behavior of the atmosphere of Saturn using ground-based observations taken with VLT-UVES and Doppler velocimetry techniques, thereby complementing measurements by orbiter instruments.

Ground-based coordinated observation campaigns also have an important

role in the characterization of the winds, for the adequate determination of the dynamic regime that rules the atmosphere's circulation, and, in this way, achieving a better characterization of the variables involved and, ultimately, a higher understanding on the subject.

The main purpose of this thesis is to contribute to a better understanding of the dynamics of Saturn's atmosphere, constraining its characterization at the 70-mbar pressure level, hoping to complement, in the future, the observations of the Cassini spacecraft with ground-based observations. We measured the zonal wind velocity and its spatial and temporal variability, by means of high precision spectroscopy and Doppler velocimetry. The observations were made with the high-resolution spectrograph UVES with ESO's Very Large Telescope (VLT). We used a method of direct measurement of the planetary winds based on high resolution spectroscopy in the visible range.

This method allowed us to search for jet-like structures at high latitude and its variation with time; study the variation of the wind according to the local time and search for a meridional wind component. Due to the fact that the errors on absolute wind velocity measurements on Saturn are on order of 10-100 ms^{-1}, this implies that $\Delta\lambda/\lambda \sim 10^{-6}$, if the Doppler shift of a single spectral line is used. In that case the spectral resolution would have to be R $\sim 10^6$, which is manifestly impractical with currently available instruments.

This spectral resolution points to the need of a method based on Absolute Astronomical Accelerometry (AAA) (Connes , 1985), which uses the full spectral information available in individual line shifts. As the sunlight dispersed by clouds of Saturn contains several thousands Fraunhofer absorption lines in the wavelength domain covered by the spectrograph, AAA provides, in this case, an accuracy of the order of a few m s^{-1} for determining radial velocities of atmospheric air, at a spectral resolution of R $\sim$ 100.000.

ESO's Very Large Telescope (VLT) with the long-slit spectrometer UVES has been used. The advantage of this instrument is threefold: (i) the availability a large wavelength coverage (the entire 480-670 nm range is covered at once), making it possible the use of hundreds of Solar lines for the Doppler shift measurements (ii) the large collecting area of the telescope (iii) the small pixel size ($\sim$ 0.3") and the 1-D instantaneous spatial dimension of the instrument.

The first two aspects allow a large gain in accuracy in the wind field, while the third allows both an instantaneous comparison of wind velocities measured in different regions of the planet and an excellent, seeing-limited

spatial resolution on the planet. Thus, both short-term variations and small-scale structures can be studied. In particular, the latitudinal dependence of the zonal wind at cloud level and the existence of wave patterns can be investigated and correlated with winds determined from cloud tracking in the Cassini-VIMS images.

Given the results obtained by the orbiter *in situ* observations, those obtained from the ground have the important task of confirming (or refuting) the values obtained by space missions, using different and independent techniques, contributing to a cross-validation of both techniques. Furthermore, another relevant question relates to the assistance that can be provided in the preparation of future space missions. Finally, another important factor is the rather smaller financial effort that these observations implies compared to the high costs of space missions. So, all the contributions that ground-based techniques can offer are a great help for the integrated planetary research.

The main goal of this research program is therefore, to provide direct, and instantaneous (the velocities retrieved for each pixel sounding the planet are obtained simultaneously) wind measurements using visible Fraunhofer lines scattered at Saturn's clouds, which allows spatial wind variability studies and will make possible to obtain a latitudinal profile of the zonal wind. This will also contribute for cross validation of both methods, the Doppler wind velocimetry and the cloud tracking method, which measure winds independently.

1.3 Thesis Structure

This master thesis is organized as follows:

Chapter 2 gives a brief and introductory description of the Saturn (structure, composition, chemistry and some important atmospheric phenomena), a brief history of exploration (focusing more on the 20th century space missions) and its atmospheric dynamics state of the art.

Chapter 3, firstly describes the UVES high-resolution spectrograph that is coupled to the 8-meter class telescope VLT, and with which the observations that are the basis for the first part of this work research program, were carried out. The observations, the data analysis method and the corrections of the Young and geometric projection effects are described in the following.

Next, we present the details of the observations from which the data were

selected, namely dates, geometry of the slit's positioning, sky conditions, methodology/strategy.

The complete data reduction process will be analyzed, including the adaptations, step by step, made to the computer programs used in this work and some sensitivity studies of the data analysis method were performed in order to assure the robustness and reliability of the Doppler velocimetry used.

The results of wind measurements are then presented. The interpretation of the results, in particular their comparison with previous Cassini observations by the VIMS instrument, and with the cloud tracking technique are presented in this chapter's last section.

Finally, chapter 4, summarizes and discusses the results and gives an outlook on possible future work.

Chapter 2

Introduction

2.1 A brief analysis of the planet

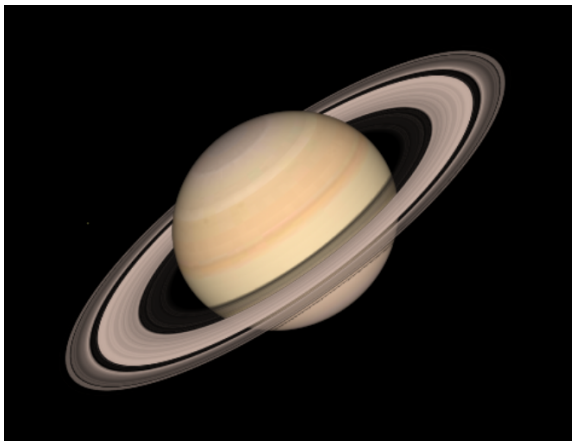

Figure 2.1: Sample image of Saturn and its ring system, taken from Stellarium planetarium software.

Saturn, named after the Roman god of the agriculture is the sixth planet from the Sun and the second-largest in our Solar System, after Jupiter. It is classified as a gas giant, with an average equatorial radius nine times that of the Earth, ninety-five times its volume and one-eighth of the density. As much as the scientific community knows, Saturn's core might be made of iron-nickel and rock (silicon and oxygen compounds), surrounded by a deep layer of metallic hydrogen, an intermediate layer of hydrogen and helium, both in the liquid state and a gaseous outer layer. The magnetic field (which

is weaker than Earth's) is thought to be generated by an electrical current within the metallic hydrogen.

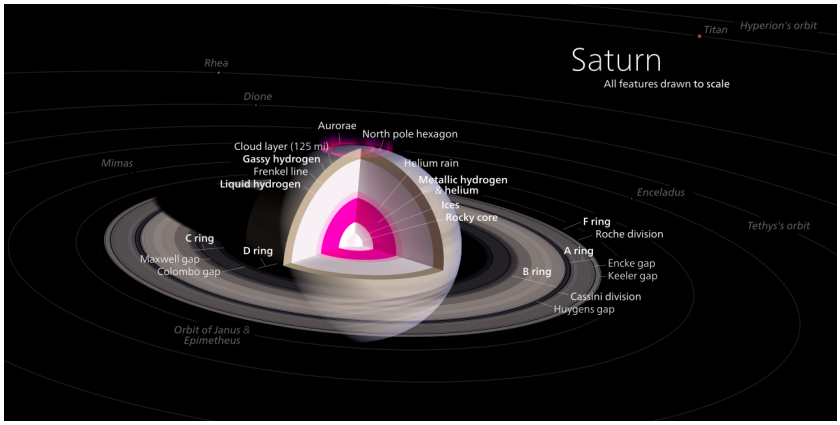

Figure 2.2: Diagram of Saturn's interior, atmosphere, ring system and closer moons. (Source: https://en.wikipedia.org/wiki/Saturn)

Saturn in composed predominantly by molecular hydrogen (∼96%), helium (∼3%) and trace amounts of methane (∼0,4%), ammonia (∼0,01%), hydrogen deuteride (∼0,01%) and ethane (0.0007%). It was also detected the presence of ices of ammonia, water and ammonium hydrosulfide (NH_4SH). Saturn has a pale yellow hue due to the ammonia crystals in its upper atmosphere.

Saturn's atmosphere exhibits a banded pattern similar to Jupiter's, but Saturn's bands are much fainter and are much wider near the equator. Saturn's finer cloud patterns were not observed until the flybys of the Voyager spacecraft during the 1980s. Since then, Earth-based telescopes improved to the point where regular observations can be made (Orton , 2009).

The composition of the clouds varies with depth and increasing pressure. In the upper cloud layers, with the temperature in the range 100 - 160 K and pressures extending between 0.5 - 2 bar, the clouds consist of ammonia ice. Water ice clouds begin at a level where the pressure is about 2.5 bar and extend down to 9.5 bar, where temperatures range from 185 - 270 K. Intermixed in this layer is a band of ammonium hydrosulfide ice, lying in the pressure range 3 - 6 bar with temperatures of 290 - 235 K. Finally, the

lower layers, where pressures are between 10 - 20 bar and temperatures are 270 - 330 K, contains a region of water droplets with ammonia in aqueous solution(Dougherty et al., 2009).

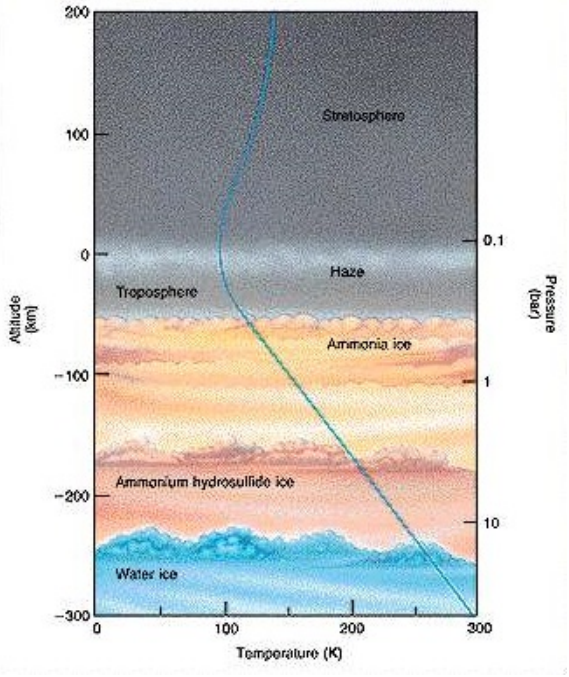

Figure 2.3: Diagram showing the structure of Saturn's atmosphere and the evolution of the temperature with altitude and pressure. (Source: http://hendrix2.uoregon.edu/∼imamura/121/lecture-13/jupiter_atmosphere.html)

Saturn's atmosphere is usually uniform, occasionally exhibiting long-lived oval-shaped storms and other features common on Jupiter. In 1990, the Hubble Space Telescope imaged an enormous white cloud near Saturn's equator that was not present during the Voyager encounters. In 1994 another smaller storm was observed. The 1990 storm was an example of a Great White Spot, a unique but short-lived phenomenon that occurs once every "saturnian" year, roughly every thirty Earth years, around the time of the northern hemisphere's summer solstice. Previous Great White Spots were observed in 1876, 1903, 1933 and 1960, with the 1933 storm being the most famous. If the periodicity is maintained, another storm will occur in about 2020 (Moore , 1992).

The winds on Saturn are the second fastest among the Solar System's planets, after Neptune's. Voyager data indicate that the winds on the equator can reach up to 500 ms^{-1} (1800 kmh^{-1})(Hamilton , 1997). Thermography has shown that both poles are surrounded by warm-core vortices with associated cyclonic circulations with thick high clouds, especially at the north pole - the Hexagon, that was named this way due to its hexagonal shaped storm, that has swirled around for more than 30 years. This is the only known example of such a phenomenon in the Solar System. Whereas average temperatures on Saturn are normally -185 °C, temperatures on the north vortex often reach as high as -122 °C, suspected to be the warmest spot on the planet.

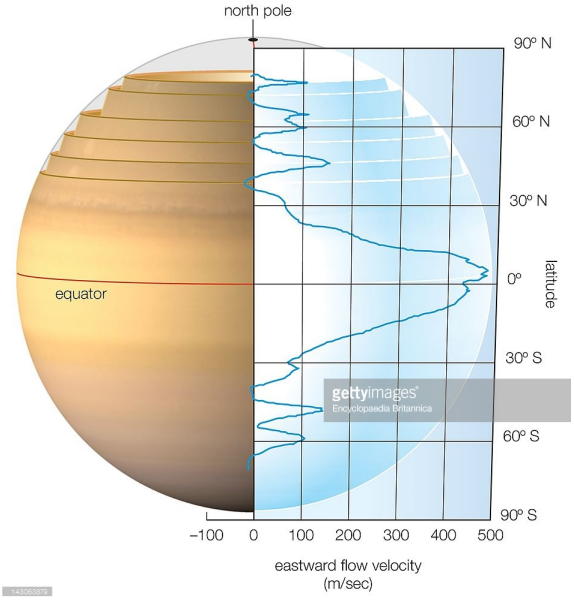

Figure 2.4: Approximation of the latitudinal profile of the wind speeds in the Saturn's atmosphere. (Source: http://www.gettyimages.pt/fotos/saturn-wind-speed)

2.2 Exploration of Saturn from ancient times to modern NASA and ESA probe missions

Saturn has been known since prehistoric times. In ancient times, it was the most distant of the five known planets in the Solar System (excluding Earth)

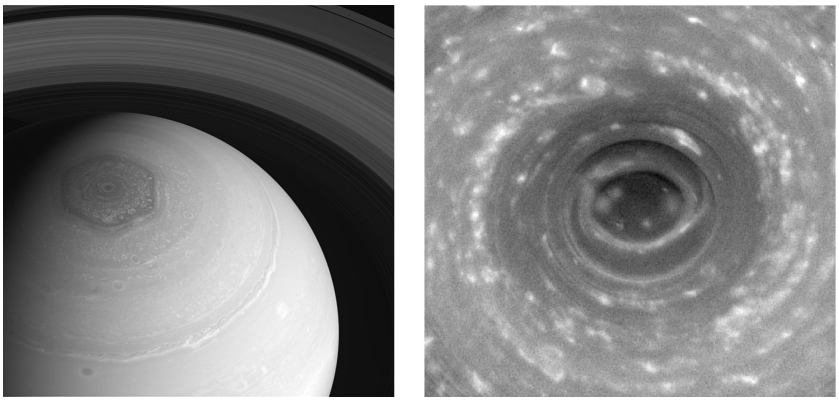

Figure 2.5: Views of the storms at Saturn's north (left) and south (south) polar regions. (Sources: https://lightsinthedark.com/2013/12/04/cassinis-best-look-yet-at-saturns-crazy-hexagon/ ; http://www.jpl.nasa.gov/images/)

and thus a major character in various mythologies. Babylonian astronomers systematically observed and recorded the movements of Saturn(Sachs , 1974). In ancient Roman mythology, the god *Saturnus*, from which the planet takes its name, was the god of agriculture.

The Romans considered *Saturnus* the equivalent of the Greek god *Kronos*. The Greeks had made the outermost planet sacred to *Kronos*, and the Romans followed suit (Evans , 1998). The Greek scientist Ptolemy based his calculations of Saturn's orbit on observations he made while it was in opposition.

Saturn's rings require at least a 15 mm-diameter telescope to resolve and thus were not known to exist until Galileo first saw them in 1610 (Cain , 2008). He thought of them as two moons on Saturn's sides. It was not until Christiaan Huygens used greater telescopic magnification that this notion was refuted. Huygens discovered Saturn's moon Titan; Giovanni Domenico Cassini later discovered four other moons: Iapetus, Rhea, Tethys and Dione. In 1675, Cassini discovered the gap in the ring system now known as the Cassini Division.

No further discoveries of significance were made until 1789 when William Herschel discovered two further moons, Mimas and Enceladus. The irregularly shaped satellite Hyperion, which has a resonance with Titan, was discovered in 1848 by a british team.

2.2.1 Pioneer 11 flyby

Pioneer 11 carried out the first flyby of Saturn in September 1979, when it passed within 20.000 km of the planet's cloud tops. Images were taken of the planet and a few of its moons, although their resolution was too low to discern surface detail. The spacecraft also studied Saturn's rings, revealing the thin F-ring and the fact that dark gaps in the rings are bright when viewed at high phase angle (towards the Sun), meaning that they contain fine light-scattering material. In addition, Pioneer 11 measured the temperature of Titan.

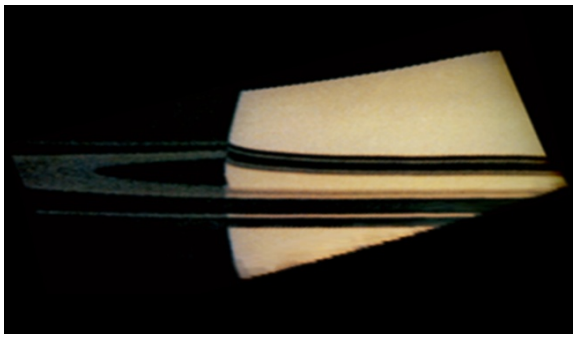

Figure 2.6: Pioneer 11 image of Saturn taken on 1979/09/01. Re-processed image to reduce noise and correct color balance. (Source: https://en.m.wkipedia.org - Pioneer 11 image of Saturn)

2.2.2 Voyager sisters

In November 1980, the Voyager 1 probe visited the Saturn system. It sent back the first high-resolution images of the planet, its rings and satellites. Almost a year later, in August 1981, Voyager 2 continued the study of the Saturn system. More close-up images of Saturn's moons were acquired, as well as evidence of changes in the atmosphere and the rings. Unfortunately, during the flyby, the probe's turnable camera platform stuck for a couple of days and some planned imaging was lost.

2.2.3 Cassini-Huygens spacecraft

On 1 July 2004, the Cassini-Huygens space probe performed the SOI (Saturn Orbit Insertion) maneuver and entered orbit around Saturn. Before the SOI, Cassini had already studied the system extensively. In June 2004, it had conducted a close flyby of Phoebe, sending back high-resolution images

and data. Cassini's flyby of Saturn's largest moon, Titan, has captured radar images of large lakes and their coastlines with numerous islands and mountains. The orbiter completed two Titan flybys before releasing the Huygens probe on 25 December 2004. Since early 2005, scientists have been tracking lightning on Saturn.

In April 2013 Cassini sent back images of a hurricane at the planet's north pole twenty times larger than those found on Earth, with winds faster than 530 kmh^{-1}. In the 21st century observations continue from the Earth (or Earth-orbiting observatories) and from the Cassini orbiter at Saturn.

2.3 Saturn's atmospheric dynamics

Saturn is characterized by a dynamical regime of rapidly rotating, internally heated atmosphere, with zonal winds that obey to a differential rotation in latitude. These winds have remained steady for decades, slightly stronger winds at deeper levels and eddies that supply energy to the eastward equatorial jets, with velocities up to 500 ms^{-1} in the upper cloud level. In Sánchez-Lavega et al. 2003, it was reported a decrease of 200 ms^{-1} of the speed of Saturn's equatorial zonal jet from 1996 (450 ms^{-1}) to 2002 (250 ms^{-1}), as the planet approached the southern summer solstice. Given the long Chronian year of 29.5 terrestrial years, and the still unknown mechanisms driving Saturn's general circulation, it is important to follow the evolution of its winds now and in the coming years.

Through its seasonal cycle, Saturn develops planetary scale convective storms at the equator and tropical latitudes, called Great White Spots (GWS) that encircles the planet at a certain latitude band, and are characterized by a very high level of electrical activity. The last GWS occurred between December 2010 and June 2011 and was centered at $41.1 \pm 1.1^\circ$ N (Hueso et al., 2012). The meridional circulation at and below the visible cloud level consists of upwelling (downwelling) convective clouds at cyclonic (anti-cyclonic) shear latitudes (DelGenio et al., 2009). Planetary waves are also a useful diagnostic of the background state of the atmosphere, as their propagation relies on the static stability and vertical shears on zonal winds.

2.3.1 Spectroscopic studies of the atmospheres of gas giants

In the spectra of gas giant planets, we can observe some important absorption lines due to the presence of elements like methane, ammonia and

Figure 2.7: A global storm (Great White Spot or *GWS* encircles the planet in 2011. The head of the storm (bright area) passes the tail circling around the left limb. Image captured by the Cassini probe. (Source: http://www.jpl.nasa.gov/news/news.php?release=2011-203)

hydrogen in the atmosphere that absorb part of the solar radiation according to their chemical behavior. The spectroscopic study of gas giants (Jupiter and Saturn) rises the issue of a stable reference spectra due to the fast rotation rate of this planetary bodies.

As we can see in figure 2.8 clearly show the presence of absorption bands in the wavelength range that it will be covered with UVES/VLT. In the present work, I obtained an overall Doppler shift from all the lines but in the follow up of this work I intend to remove this wavelength absorption bands that I will explain in the chapter "Conclusions and Outlook" in order to obtain spectra just with the Fraunhofer lines. We also can see that this planets have a quite different visible spectra showing absorption bands from different chemical compounds. In the case of Saturn, the most relevant molecules are methane, by far the most prominent, ammonia and hydrogen.

In image 2.9 of the Saturn's retrieved spectra, we can observe telluric lines coming from the Earth's atmosphere and absorption lines originated on Saturn's atmosphere, due to the presence of molecules like methane, ammonia and hydrogen; beyond those solar Fraunhofer lines coming from solar back-scattered radiation. It is clear that there is some tilt of the absorption lines from Saturn and the Fraunhofer lines. We can also see in the upper part of figure 2.9 that the receding part of the rings produces velocities (just keplerian velocities), containing only Fraunhofer lines, and where the tilt of the line is due to the spatial resolution that allows sounding the rings across

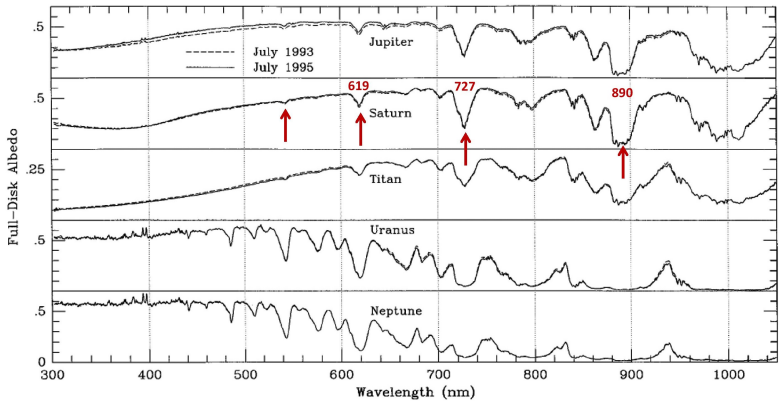

Figure 2.8: Visible spectra of the gas giants. Here we can see the prominent absorption bands from methane. We can find that a small absorption band from methane is in the range of the wavelengths covered by UVES in this work, which will affect considerably the retrieved Doppler velocities. (Courtesy of Sánchez-Lavega, June 2016)

its width, producing, as expected (see top of the figure for the receding limb and the bottom for the approaching limb), velocities from 16.6 kms^{-1} on the outer part of the rings to 20.5 kms^{-1} in the inner part of the rings.

Obviously, the tilt is reversed for the receding and approaching limbs, because the pixels that are sounding the rings, across the slit's direction, are measuring velocities that increase from the outer ring to the inner ring, for the case of the approaching limb but the velocities are negative for the receding limb, which produces Doppler shifts in the opposite direction.

We can also note that we have three kinds of tilt in the spectral lines: the vertical lines come from telluric lines from Earth's atmosphere and the most tilted ones come from Fraunhofer lines, because we are measuring a back-scattered radiation and so, there is, in a first approximation, a Doppler shift in the absorption and another Doppler shift in the re-emission. The intermediate tilted lines are due of pure absorption lines, not an echo, mostly from methane but also, in minor scale, from ammonia and hydrogen.

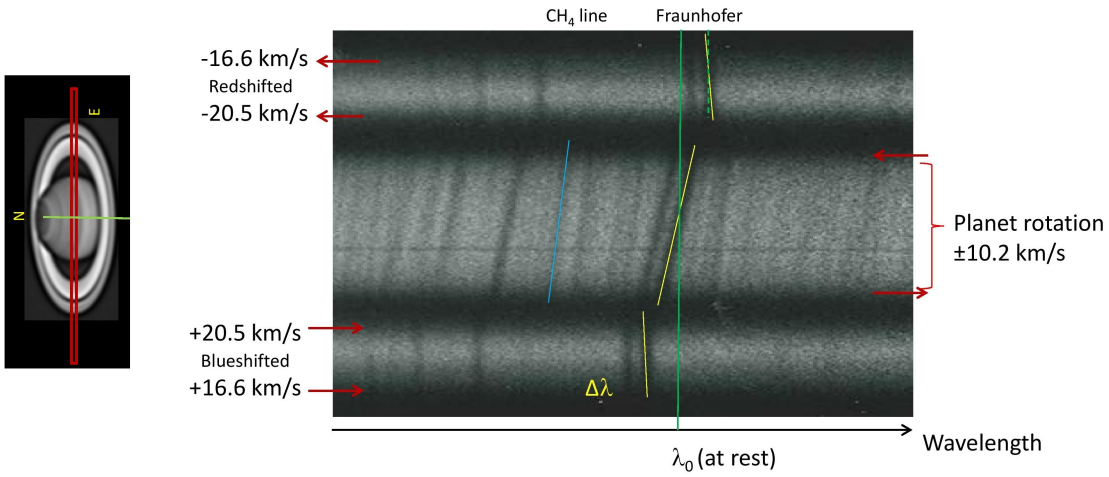

Figure 2.9: Example of a Saturn spectra, where we can see lines with different tilts. The vertical ones are due to telluric lines produced in Earth's atmosphere; the lines with a higher tilt are due to the solar radiation backscattered in Saturn's atmosphere and the increase of the tilt is due to the fact that dispersion, in a first approximation, is an absorption followed by a re-emission, with a double Doppler shift (one in the absorption and one in the re-emission). The intermediate lines are due to absorption from methane, ammonia and hydrogen in Saturn's atmosphere, with a single Doppler absorption in the process. In general, lines are tilted because the spectral border is a set of super-imposed spectra with spatial resolution along the slit, measuring points with different velocities, which produces slightly different Doppler shifts. (Courtesy of Sánchez-Lavega, June 2016)

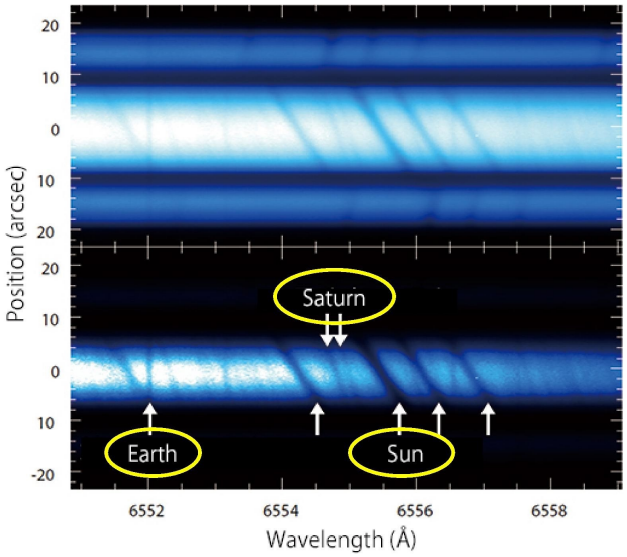

Figure 2.10: In this figure we can see the receding ring in the top of the image and the approaching limb in the bottom of the image, where is notorious the tilt of the lines due to the increase keplerian velocity with approximation of the planet.The receding limb shows negative values and the approaching limb has positive values. In the middle of the figure, we have the spectra coming from Saturn itself, where we can see tilted lines with a high tilt due to the back-scattered radiation (it is an echo, so the Doppler is doubled) and less tilted lines due to pure absorption by molecules in Saturn's atmosphere. (Courtesy of Sánchez-Lavega, June 2016)

2.3.2 Addressing the issue of Saturn's rotation rate

As a gas giant, Saturn does not have a solid surface, making it difficult to define a rotation period for the planet as a whole, and as such, it has been historically difficult to measure this quantity. Its hazy atmospheric features shift with respect to each other and cannot be used to clock the spin rate of the planet's interior. For Saturn's rotation period and average rotation velocity, it is often given the average values obtained from the Cassini mission: $T \sim$ 10h 45m and $\bar{v} \sim 9690\ ms^{-1}$.

However, due to the fact that Saturn is a gaseous planet and it doesn't behave like a solid body when it rotates, it presents a differential rotation in latitude, which has been puzzling astronomers. Even more, the radio data collected from Cassini suggest that the planet is rotating slower (by 6 minutes, or one percent) than two decades before, when Voyagers 1 and 2 flew by in 1980 and 1981.

Dr. Don Gurnett, principal investigator for the Cassini Radio and Plasma Wave Science Instrument said that "although Saturn's radio rotation period has clearly shifted substantially since the Voyager measurements, I don't think any of us could conceive of any process that would cause the rotation of the entire planet to actually slow down".

One possible explanation is that the electrically charged ionosphere surrounding Saturn is "slipping" relative to the planet's rotation. This ionosphere influences the shape of the magnetic field (which controls the charged particles responsible for the radio emission), so a change in the friction between the ionosphere and upper atmosphere, due perhaps to seasonal variations in solar illumination, might account for the difference between the Voyager and Cassini data. Gurnett suggests the solution may be tied to the fact that Saturn's rotational axis is nearly identical to its magnetic axis. Jupiter, with a more substantial difference between its magnetic axis and its rotational axis, shows no comparable irregularities in its radio rotation period.

Dr. Alex Dessler, a senior research scientist at the University of Arizona, Tuscon, said that "(...) this finding is very significant. It demonstrates that the idea of a rigidly rotation magnetic field is wrong". In that way, the magnetic fields of gas planets may resemble that of the Sun. The Sun's magnetic field does not rotate uniformly. Instead its rotation period varies with latitude, so Saturn's magnetic field has more in common with the Sun that with

the Earth. "The measurement can be interpreted as showing that the part of Saturn's magnetic field that controls the radio emissions has moved to a higher latitude during the last two decades," continued Dressler.

Different portions of its "visible surface" represent different circulation systems in its atmosphere and move around its axis at different rates, depending on whether they have westward or eastward motions relative to the overall rotation of the planet. One can distinguish three different regimes, according to the latitude, that we will refer to henceforth (Benton , 2006; Stevenson , 2006; Anderson , 2007):

- System I, which encompasses the equatorial region and low latitudes (the North and South Equatorial Belts), with a period of 10h 14min;
- System II - which refers to high latitude (or non-equatorial) regions assigned with a rotation period of 10h 38min 25.4sec;
- System III - which refers to the rate of rotation of the planet's radio emissions (retrieved by Voyager flybys at the 1980's), of about 10h 39min 22.4sec. When approached Saturn in 2004, the Cassini's Radio and Plasma Wave Science instrument detected that the radio rotation period had increased appreciably, to approximately 10h 45min 45sec ($\pm$36sec), which means that the rotation had slowed about 6 minutes, which is one percent. This finding indicates that this rotation period is not associated with the "real" rotation of the planet, since there is no conceivable way that such an immense object could have its real rotation change so rapidly. The polar regions are considered to have rotation rates similar to System I.

In March 2007, it was found that the variation of radio emissions from the planet did not match Saturn's rotation rate. This variance may be caused by geyser activity on Saturn's moon Enceladus. The water vapor emitted into Saturn's orbit by this activity becomes charged and creates a drag upon Saturn's magnetic field, slowing its rotation slightly relative to the rotation of the planet.

Chapter 3

VLT/UVES observations

3.1 Ultraviolet-Visual *Echelle* Spectrograph (UVES)

Figure 3.1: ESO's telescopes at Paranal, Atacama desert, Chile. (Figure: ESO's *website*).

The UVES (Ultraviolet-Visual Echelle Spectrograph) is an *echelle* spectrograph, mounted in one of the four telescopes of the VLT (Very Large Telescope), namely the UT2. It is one of the facilities of the European consortium ESO, and is located at Cerro Paranal in the desert of Atacama, Chile. The spectral resolution (nominal) designed for this unit, with an 1-arcsec (") slit was 40,000 (D'Odorico et al., 2000). *Echelle* spectrographs are tools of great importance in all projects involving large telescopes, since high-resolution spectroscopy is one of the modes of observation that most benefit from a large light collecting area, which makes the telescope resolve the absorption lines and helps to detect the chemical species present in the atmospheres, allowing to map its composition with high detail.

UVES addresses the following scientific objectives:

- Study gas and stars' kinematics in the galactic center.
- Kinematics and mass distribution of stellar clusters.
- Composition, kinematics and physical conditions of the interstellar medium in our galaxy and surrounding systems.
- Study of stars' seismology and stellar oscillations.
- Structure, physical conditions and abundances of the interstellar and intergalactic gas. Especially for gas near QSOs (quasi-stellar objects or *quasars*) absorption spectra with high redshift.

3.2 VLT and UVES description

The UVES is a two-arms cross-dispersed instrument (with one cross disperser for each arm), with a typical order separation of 10", covering wavelength bands of 300 - 500 nm for the "blue arm" and 420 - 1100 nm in the "red arm" (see figure 3.2), being able to elaborate spectroscopy studies involving compact and large objects, such as Saturn. This separation also allows a good sampling of the sky's scattered light at red wavelengths band, also enabling an accurate estimation of the background radiation at spectral inter-orders.

The versatility of the tool allows the use of each arm separately or in parallel, through the use of a prism that separates the incoming light into two beams of different wavelength ranges. The maximum spectral resolution that can be achieved by using a narrow slit, or using one image slicer, is about 110,000 in the red-arm and about 80,000 with the blue-arm. In this case the numerical resolution of the instrument is of 2 pixels.

For radial velocities studies, the device basic precision is about 50 ms^{-1}, however the inclusion of a iodine cell in the beam-pass increases the precision in a decisive way, as we shall see in the next section of this chapter. The two arms of the telescope (blue and red) are equipped with large science CCD's : the red-arm shows a two chips mosaic while the blue arm has a unique chip (Dorn et al., 2000).

The calibration unit contains a 45° mirror, lamps to perform the flat field exposures and a Thorium-Argon (Th-Ar) lamp for high-resolution wavelength calibration. As an alternative calibration process, it is also possible to mount, on the transverse mirror, a iodine lamp (I_2), which can be coupled

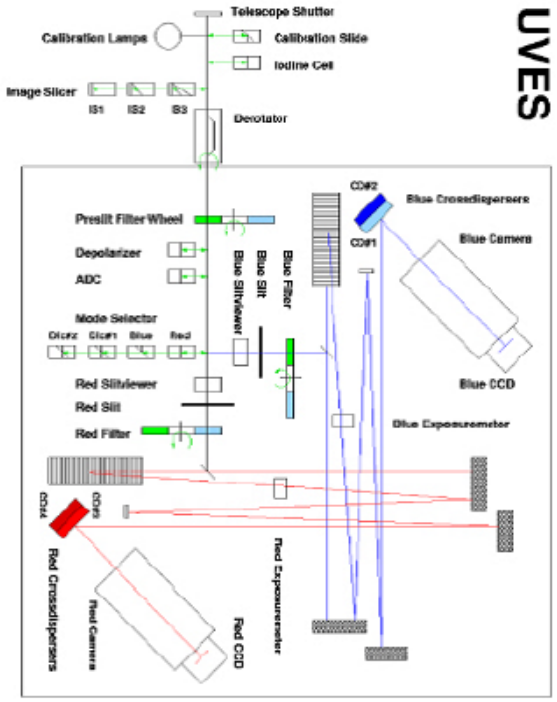

Figure 3.2: UVES optical path, from the incoming radiation entry untill its acquisition by the detector's CCDs. (UVES User Manual - *Paranal Science Operations*).

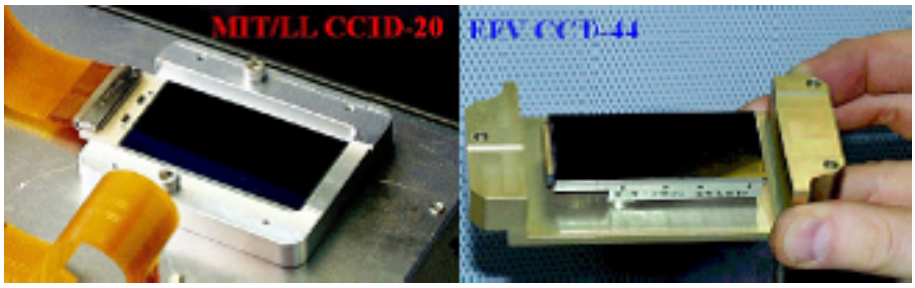

Figure 3.3: The two CCD detectors in UVES (Dorn et al., 2000).

to the optical path, in order to insert in the spectrum a set of calibrated absorption lines for precise wavelength calibration, and thus enabling a very stable radial velocities measurement, but with the inconvenience of mixing the spectrum with an overlapping "forest" of iodine absorption lines.

The UVES *echelle* grating, at the construction date, was the largest monolithic diffraction device developed. The importance of this technological development resided in the possibility to increase the spectrograph spectral resolution until stellar absorption lines became resolved . Some years later, in December 2002, when the high-precision HARPS spectrograph (High Accuracy Radial Velocity Planetary Search object) came into operation on the 3.6 meters telescope at La Silla (Chile), with the aim of finding extrasolar planets, has been chosen the same kind of UVES' *echelle* to equip it.

The readout noise is less than 2 electrons for the EEV detector and less then 3 electrons for the MIT/LL detector, that for a 50 kpixel/s reading speed at each gate. The EEV CCD has a capacity of 225.000 electrons, with high quantic efficiency at ultraviolet range; while the MIT CCD has a capacity of 130.000 electrons and presents high quantum efficiency at the near infrared band. The first physical 50 pixels are assigned to, at each CCD output gate, pre-scan operations.

The UVES spectrograph's blue arm has an optical field of 30,7×30,7 mm, while for the detector's red arm system an 61,4×61,4 mm optical field is required, which implies that most of the two CCD pixels will receive radiation, and so, it must be active in the read out mode.

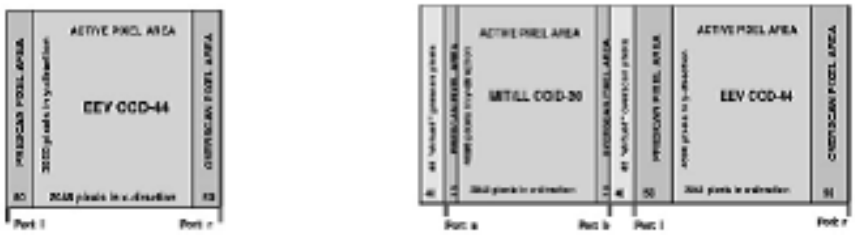

Figure 3.4: Observed images *setup* for blue arm configuration CCD (on the left), and for the two-CCD mosaic that compose the red arm's detector. (Dorn et al., 2000).

The CCDs used in astronomy have to be cooled until 140 - 160 K in order to reduce the noise produced by the *dark current* to negligible values.

Therefore, CCDs are mounted on a vacuum chamber cooled, in turn, by liquid nitrogen. The cooling and thermal stability of CCDs is assured by a cryostat unit(CFCs) developed by ESO.

The detection efficiency is the key parameter in evaluating the overall efficiency of an instrument, relative to its ability to collect scientific data. Another vital parameter is the size of the spectral range covered by a single exposure. The two basic configurations of the UVES cover spectral ranges of 90 nm (λ_{center} = 346 nm) + 200 nm (λ_{center} = 580 nm) and of 100 nm (λ_{center} = 437 nm) + 400 nm (λ_{center} = 860 nm), i.e. for a single exposure, and respectively for each arm (blue + red arm). Note that the encompassed wavelengths have no intervals, except a 5 - 10 nm loss at the junction of the two CCDs that compose the detector's mosaic for the red arm.

	Blue, EEV	Red Mosaic
Quantum efficiency	49% at 320 nm 56% at 350 nm 82% at 400 nm 88% at 500 nm	89% at 450 nm (EEV) 89% at 600 nm (EEV) 81% at 800 nm (MIT-LL) 46% at 900 nm (MIT-LL)
Number of pixels	2048 × 3000 (2048 × 4096, used in windowed readout)	4096 × 4096 (2048 × 4096 2 × 1 mosaic)
Pixel size	15 μm	15 μm
Gain (MIT-LL values in brackets)	low: 1.84 e^-/ADU high: 0.54 e^-/ADU	low: 1.6(1.5) e^-/ADU high: 0.57(0.57) e^-/ADU
Read-out noise fast read-out, low gain (slow read-out, high gain) Ultrafast readout, low gain	4.1 (2.1) e^- rms	EEV 3.4 (2.0) e^- rms MIT 3.8 (3.4) e^- rms EEV 4.6 e^- rms MIT 4.85 e^- rms
Saturation low gain (MIT-LL in brackets)	∼65000 ADU	∼65000 ADU (∼43000 ADU)
Full frame readout (s) at 50 kpix, 2x2 bin at 225 kpix, unbinned at 625 kpix, unbinned	 34 (1-port) 30 (1-port) 6.4 (2-ports)	 45 (2-ports) 40 (2-ports) 10 (4-ports)
Dark current levels	0.4 e^-/pix/h at −120°C	EEV 0.5,MIT 1.1 e^-/pix/h at −120°C
Fringing amplitude at 850nm	-	EEV: up to 40% MIT: up to 20%
CTE	> 0.99993	> 0.99995
Read-out direction	in disp. dir.	in disp. dir.
Prescan, Overscan areas	Pix. 1-50 and 2098-2148	MIT: pix 40-50,2098-3008 EEV: pix 1-50,2098-2148
Flatness	< 15μm peak to peak	< 60μm peak to peak

Figure 3.5: UVES' nominal specifications, (ESO, UVES manual).

Since the signal-to-noise ratio (S/N) increases with the square of the telescope's diameter, it was very important that we used a large diameter

telescope class for these observations, in this case the Very Large Telescope (VLT). In the cases when very bright objects are observed, where the photon noise is dominant, the use of a big aperture telescope is still a very relevant reason in order to achieve high S/N observations in reasonably short integration times.

Figure 3.6: UVES spectrograph's test bench mount of its diverse elements (image: ESO's *website*).

3.2.1 Telescope light path

The light entering the telescope is directed to one of two different gratings by a dichroic mirror (see "mode selector" in figure 3.2). The radiation is then dispersed by these two *echelle* gratings. After passing through a cross-disperser, the radiation is then focused by dichroic cameras in CCD detectors described above, both the single CCD device (EEV) of the blue arm or in the mosaic device (EEV and MIT) from the red arm.

The UVES uses an image *derotator*, an optical device that performs a rotation of the telescope's field of view by an given angle, called the position angle. The *derotator* was used to align the slit with the planetary rotation axis.

The spectrograph slit is adjustable and its aperture ranges from 0.15" to 20" and its length is 30". The verification of the acquisition field and tracking is done using the slit viewer (a camera that "looks" at the blades of the spectral slit, thus providing an image of the target field).

	Blue Arm	Red Arm
Wavelength range	300–500 nm	420–1100 nm
Resolving power-slit product nm/pixel	41,400 0.0019 nm at 450 nm	38,700 0.0025 nm at 600 nm
Max. Resolving power (2-pixel sampling)	~80,000	~110,000
Throughput at blaze (TEL+UVES, no slit, no atm.)	12% at 409 nm	14% at 600 nm
Limiting magnitude (90m exp. time, S/N=10, 0.7 arcsec slit,seeing 0.7)	18 R=58,000 at 360 nm	19.5 R=62,000 at 600 nm
CCDs	2048 × 4096 (windowed to 2048 × 3000)	two 2048 × 4096 (mosaic of different types)
Pixel (15μm) scale disp. dir. (varying along order) along slit (dep. on cross-disp.)	0.215″ ± 20% 0.25″(CD1 and CD2)	0.155″ ± 20% 0.18″ (CD3),0.17 (CD4)
Echelle (R4 mosaic)	41.59 g/mm	31.6 g/mm
Cross dispersers Blaze wavelength Blaze wavelength	CD1: 1000 g/mm 430 nm CD2: 660 g/mm 460 nm	CD3: 600 g/mm 560 nm CD4: 312 g/mm 770 nm
Typ. wavel. cov. CD1 and CD3 (CD2 and CD4 in parenthesis)	85 (126) nm in 33 (31) orders	200 (403) nm in 37 (13) orders
Min. order separation (standard setup)	10 arcsec (40 pixels)	9 arcsec (51 pixels)

Figure 3.7: Characteristics and observing capabilities of the UVES spectrograph. UVES' manual - *Paranal Science Operations*.

3.2.2 Opto-mechanical design

The instrument consists of two main parts: the first is mounted on the rotor, which remains stationary while the telescope adapter turns to track the motion in the sky of the target field. This part includes the calibration system, a removable iodine cell, the image slicers, one optical *derotator* (permanently installed in the optical beam path). The second part consists on the spectroscopic *echelle* and the two cross-disperser arms.

The perturbations imposed by the environment were seized by installing the instrument in a controlled environment and the mobile components in the optical path were minimized to the extreme. Beyond the two slits of the spectrograph, the unique moving parts found in the optical path are the cross disperser and cameras.

3.2.3 High-precision wavelength calibration

In a first approach the wavelength calibration is made by matching the positions of spectral lines obtained from the source and the position of well known wavelength from a calibration exposure's spectral lines. Such preliminary wavelength determination is not precise enough to obtain the precision needed to perform the high-resolution spectroscopy required. For observations analyzed in this work, a special request was made in order to perform

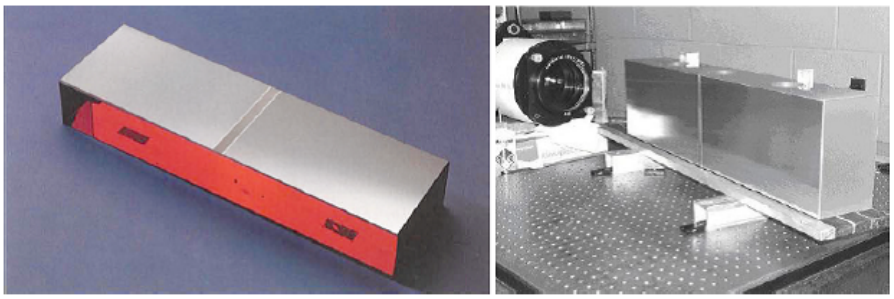

Figure 3.8: UVES monolithic *echelle* grating. This device is a piece of the highest technology in the field of high precision spectroscopy at the service of astronomy and astrophysics, (Dekker et al., 2000).

specific Th-Ar calibration observations, together with each block of observations.

The wavelength calibration technique based in exposures of a Thorium-Argon lamp, has the advantage of no longer "consuming" the target source radiation, because it performs a sequential exposure of a Th-Ar calibration lamp. Another advantage is the range of wavelengths covered, which in this case extends from 478 to 680 nm.

This technique relies on the assumption that the two spectra will follow a similar path on the detector, the one from the target and the one from the Th-Ar lamp exposure, so if there is an instrumental drift during the measurement process, both spectra are affected on the same way by the instrumental drift. This technique also has the advantage of high optical stability of the Th-Ar calibration source.

In order to be able to measure Doppler wind velocities at Saturn, from the ground, it is necessary to obtain high precision measurements of radial velocities (RV). This required the use of a spectrograph, such as UVES, a very broad spectral window and very stable reference spectra (obtained by means of the already explained calibration methods), supplemented by an effective data reduction process. These techniques are also used in the demanding field of exoplanet detection where it is crucial to obtain the highest possible spectral resolution in order to obtain accurate radial velocities.

In the case of very faint stars or in the case of large target fields (such as the study of Saturn's atmosphere), the use of large mirrors in order to collect the radiation from the target source, become fundamental to increase

the spatial resolution at extended sources (case of the Saturn's atmosphere) or to improve the detection capability (case of weak sources).

The method of radial velocity is limited to establishing the observer's line-of-sight component of the velocity, and is not sensitive to inclinations of the orbit or the transverse components of velocity relative to the line-of-sight. For these reasons, the measurements obtained by my work, are the global Doppler velocity of Saturn's atmospheric winds and must be de-projected from the line-of-sight. So, the measured Doppler velocity retrieved must be compensated from a geometric factor in order to correct it from its intrinsic projection.

3.3 Doppler Velocimetry

The methods developed in recent planetary wind measurements in the visible range using high-resolution spectroscopy (Civeit et al., 2005; Luz et al., 2006; Widemann et al., 2008; Machado et al., 2012, 2014) address the fundamental problem of maintaining a stable velocity reference. There are systematic errors involved in trying to measure absolute wavelengths or Doppler shifts with grating spectrographs.

The reason is that, for single line shifts, the dispersion law and instrumental uncertainties cannot achieve an absolute accuracy better than about 100 ms^{-1}, while in measuring the global wind circulation at the sounded pressure level, we are addressing wind amplitude variations or wind latitudinal gradients of the order much smaller than 100 ms^{-1}, projected on the line-of-sight, regarding that line shifts for this velocity magnitudes will produce a line shift much smaller than the line width.

One possible solution is therefore to measure relative Doppler shifts between two sets of absorption lines, for that we used the spectra coming from the slit's central pixel as a reference spectra for each slit's offset position. The Doppler velocimetry method used is an adaptation of the Absolute Astronomical Accelerometry (AAA) developed by Connes, 1985.

The Doppler measurement is based on an optimal weighting of the Doppler shifts of all the lines present in the spectrum, with relation to a reference spectrum. In this work the measured and reference spectra are taken *simultaneously*, with the latter being taken at the center of the slit. The algorithm generates line-of-sight Doppler shifts as a function of pixel number along the slit length, which is converted as a function of latitude or longitude, for each exposure. We then computed the average of the set of two or three velocity

profiles associated with each slit position offset.

For the data analyzes procedures I adapted a software package previously developed and validated in (Civeit et al., 2005) and subsequently used for retrieving Venus winds (Machado et al., 2012, 2014). The scripts are in MATLAB programming language. The detailed description of this package is given in Appendix B.

I adapted the method to long-slit measurements of a large target body and to perform several corrections, in particular:

a) by introducing a geo-referencing correspondence between pixel location and geographic coordinates;

b) to change the size of the active sounding window of the slit, which means, that the number of pixels of the slit that will be used by the pipeline to produce the spectra;

c) to correct for slit image curvature, since the slit image produced on the CCD is slightly banded, and when one normalizes the spectra in order to obtain 2D spectra, this tilt produces relevant spurious Doppler shift, and so, is mandatory to correct the referred curvature before normalizing the spectra;

d) to evaluate for the systematic shift known as the Young effect (Y);

e) to correct for the specific geometry of the observations, as I explain in section 3.5;

f) to remove telluric lines from the spectra (though this correction proved negligible in comparison to other effects).

A batch of new tests were also performed. All this items will be discussed in detail in the following.

Due to a gap of 10 nm between the two CCD chips in the red arm detector, the spectra recorded in the EEV and MIT chips need to be extracted and treated separately, in order that the final spectra doesn't show discontinuities. Spectra of different spectral orders were also extracted and analyzed separately (see figure 3.9). The extraction has been performed by a spline interpolation along the central order, in order to obtain a continuous level of the continuum in the final 1D retrieved spectra, and using the central order as a baseline, regarding that this central order is the one which where the wavelength calibration is more stable .

In order to avoid overlaps of spectral orders, the active sounding window of the slit was restricted to a size of 97 pixels on the detector, with a spatial

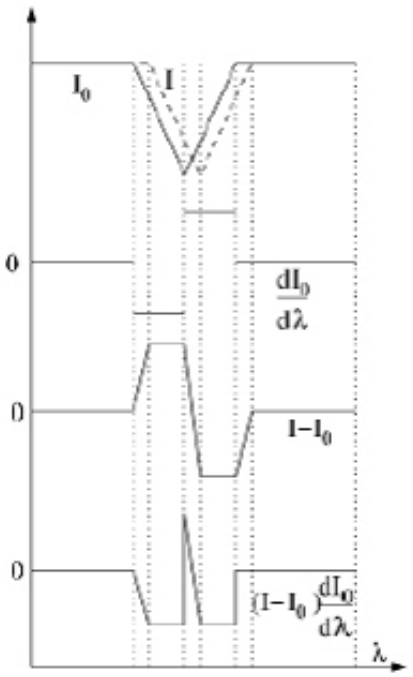

Figure 3.9: Scheme of the measurement process in case of pure photon noise. (Luz et al., 2005a)

resolution of $\sim$ 1100 km/pixel at the disk center. Since the average pixel scale for the UVES red arm is 0.183"/pixel, the spatial extension on the planetary disk corresponds, in fact, to a rectangle with dimensions 0.18"$\times$0.3".

At the extraction stage, bad pixels in the detector (pixels with an abnormal response, called hot pixels) and pixels with an outlier response (probably hit by cosmic rays), were discarded by using a pre-prepared mask.

In a grating *echelle* spectrometer, the monochromatic image of a long slit will appear slightly curved, as explained before. This slit image curvature, on the order of a fraction of a pixel, induces non-negligible errors in the wavelength calibration and velocity retrieval. This effect has been corrected using the Th-Ar spectrum. Both shifts were measured using the velocimetry algorithm described in Connes, 1985. On this way, the spectral lines deviations were corrected from the spurious shifts due to the *echelle* image's curvature.

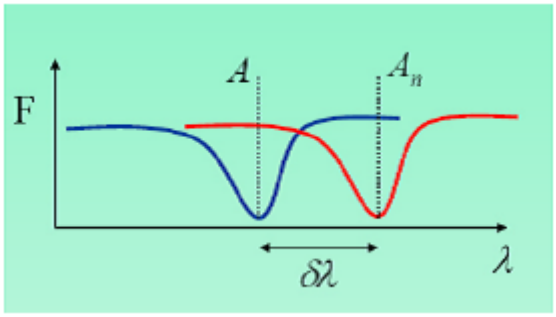

Figure 3.10: Algorithm for obtaining the radial velocity using only a single spectral line shift. (Luz et al. 2009).

3.4 The algorithm behind the method

This section presents a short description of the algorithm, which is at the basis of the process adapted by me for the Doppler velocities retrieval in this work. Let us start assuming that wind velocities were retrieved based in the shift of just one line's Doppler deviation, with the basic Doppler shift equation

$$\frac{\delta V_n}{c} = \frac{\delta\lambda}{\lambda} \tag{3.1}$$

where V is Doppler velocity associated to a specific line in the spectra, n is

the index of that line and c is the light speed in the vacuum. Here, Taylor's first order approximation can be used for the deviation of the spectral lines, since the shifts are much smaller then the line widths.

$$I_n - I \approx \frac{\partial I}{\partial \lambda}\delta\lambda \tag{3.2}$$

where I_n is the location of the shifted line and I the position of the same line in the reference spectrum. Combining the two previous equations yields the relative velocity between the reference spectrum and the shifted spectrum.

$$\frac{\delta V_n}{c} = \frac{I_n - I}{\lambda \frac{\partial I}{\partial \lambda}} \tag{3.3}$$

Or, considering the same result at the location of the pixel "i", which is more convenient to the data analyses:

$$\delta v_i = \frac{c}{\lambda(i)}\delta\lambda_i = \frac{I(i) - I_o(i)}{\frac{\lambda(i)}{c}(\frac{\partial I_o}{\partial \lambda})_{\lambda=\lambda(i)}} \tag{3.4}$$

The index "i" refers to each pixel along the slit and the index "o" refers to the reference spectra (along this work the reference is the one coming from the slit's central pixel).

However, the Doppler shifts associated with single-line wind velocities to be measured (on the order of a few ms^{-1}) implies a spectral resolution (R) of about 10^6, as we can infer from equation 3.2, that from a δV_n of around 10 ms^{-1}, it implies a $\delta\lambda$ of around 10^{-6} or a spectral resolution R of about 10^6, which is impossible with current instruments.

3.4.1 Uncertainties related to the Doppler velocity retrieval process

By analyzing the whole spectral range, rather than line by line, namely using the Absolute Astronomical Accelerometry (AAA) technique, allows to achieve a theoretical precision of a few ms^{-1}. This is done by performing a weighted average of the single-line Doppler shifts, using the inverse of the variance as a weighting factor:

$$\delta v = \frac{\sum \delta v_i \omega_i}{\sum \omega_i} \qquad where \qquad \omega_i = \frac{1}{\sigma^2[\delta v_i]} \tag{3.5}$$

The shift of solar Fraunhofer lines scattered by cloud tops is measured simultaneously on the full high-resolution spectrum between 480 - 570 nm (blue region, EEV CCD) and 580 - 680 nm (red region, MIT CCD). The visible solar spectrum contains around 4400 solar lines.

The weights (ω_i) are the inverse of each individual line velocity contribution variance. For that we must rely on the assumption that the representative noise is only of photonic origin, so $\sigma^2[I] = I$, which allows us to obtain $\sigma^2[\delta v]$ in 3.4.

The overall uncertainty in the differential velocity determination comes:

$$\sigma[\delta v] = \frac{1}{\sqrt{\sum \omega_i}} \tag{3.6}$$

For each exposure, the velocity profile has been measured as a weighted average of the shifts for the various spectral orders. The target acquisition and guiding were done automatically, based on ephemeris data provided in advance to the telescope operator. After acquisition, the position of the slit was also visually confirmed in an image of the slit viewer camera, and maintained via pointing corrections performed by the secondary guiding system. The dispersion of the measurements obtained from the different orders is the main source of uncertainty for Doppler shifts.

VLT pointing and UVES offset uncertainties are both equal to 0.1" (nominal value), and we take as the global positioning error of the slit $\sigma_{tot} = \sqrt{\sigma^2_{pointing} + \sigma^2_{offset}}$, or 0.14". The detector pixel dimension is 15 μm and the measured pixel scale in our observations presented an average of 0.183"/pixel. The slit's active sounding window correspond of 97 detector's pixels that provided an astonishing ground-based spatial resolution, where each pixel had an average equivalent dimension of 1100 km on the planetary surface (at disk center).

3.4.2 Doppler Shifts

The profiles of Doppler shift are impacted by two observational biases affecting the measurement of the zonal winds: the geometric projection factor (F) and the Young effect (Y), which result from the observational geometry and the finite solar angular diameter as seen from the target. Furthermore, the line-of-sight Doppler shift at each pixel on the planetary disk results from

the combination of the relative Earth-Saturn orbital motion, the planetary rotation (around 9690 ms^{-1} at the equator) and the cloud particles' motion relative to the ground. Orbital velocities were retrieved from the NASA Horizons ephemerids website. Overall, the absolute Doppler shift measured along the line-of-sight at any given point in the slit is:

$$\Delta V = F \cdot V + Y + OS. \tag{3.7}$$

The orbital shift (OS) induced by the relative Earth-Saturn orbital motion is the same for every point of the slit and cancels when relative Doppler shifts are computed between two spectra acquired simultaneously at different points, at the sounding point and at a reference point at the center of the slit. The remaining effects (the geometric projection factor (F) and Young effect (Y) are described below.

3.4.3 Geometric Projection Factor

The goal of this work is to measure the Doppler shift due to the motion of cloud particles in the direction of the line-of-sight, in order to subsequently determine the wind velocity. The problem can be reduced to an understanding of the interaction between solar radiation and cloud particles embedded (in the rotating atmosphere) during the scattering process.

We use the single-scattering approximation and in this framework consider the scattering process as a sequence of absorption and re-emission of the solar radiation by cloud particles in the upper cloud deck. This simplification allows computing a correction factor as a function of longitude.

Assuming, for the sake of simplicity, pure zonal motion in the retrograde sense and a 90° phase angle, two extreme cases can be considered (see figure 3.12). One, at the sub-solar point, where there is no Doppler shift in the absorption (null incidence angle) but there is a blueshift in re-emission towards Earth, see an example on figure 3.11. The other, at the sub-terrestrial point, is the converse situation where there is a redshift at absorption (90° incidence angle), but no shift in the emission towards the Earth (direction normal to the surface).

The exact geometric projection factor (F) affecting the Doppler shift can be calculated using the bisector theorem (equation 3.8, see Gabsi et al., 2008 for a detailed explanation). It is a function of the specific observing geometry and of the longitude. The line-of-sight Doppler shift is proportional to the

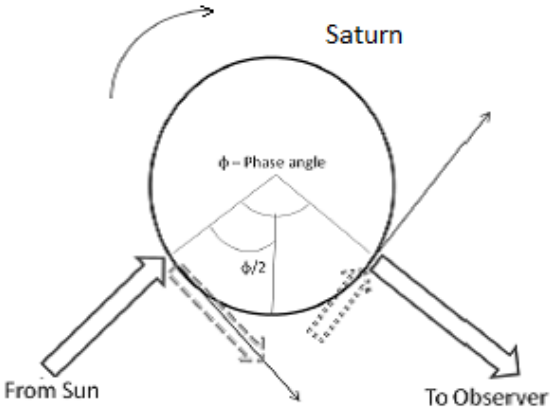

Figure 3.11: Schematics of the Doppler effect in the single scattering approximation. The dotted arrow at the sub terrestrial point indicates a redshift in the absorption of solar radiation by the atmospheric aerosols in this region, due to the atmosphere's retrograde rotation. The dashed arrow at the sub solar point indicates a blueshift in the solar radiation scattered towards the observer. Thin arrows indicate the direction of the zonal wind. Adapted from (Machado et al., 2012)

projection of the wind velocity on the bisector phase angle.

$$\Delta V = F \cdot V = V \cdot 2cos(\Phi/2)sin(\varphi - \Phi/2)cos\beta \tag{3.8}$$

where Φ is the phase angle at which the observation was made, β is the latitude of the sub-terrestrial point and φ is the longitude of the point being measured (note that the convention applied to planetary longitude is that it increases in the direction of the rotation).

The F quantity will be designated throughout this work as the geometric projection factor. Given the geometry of the observations, the projection factor vanishes at a longitude close $\Phi/2$, where the redshift produced in the absorption of incoming solar radiation and the blueshift in the emission towards Earth cancel each other (see figure3.12).

3.4.4 The Young Effect

Due to the large angular size of the Sun as seen from a planet, such as Saturn for example, and its fast rotation, for Solar System's planets, in some particular geometry of observations, where the Sun is far from the zenith, that could exist a defect in the solar illumination with an unbalance illumination

between light coming from the approaching solar limb (blue shifted radiation) and from the receding solar limb (red shifted radiation); the geometry of the solar illumination in such that the excess of one or the other will affect the apparent line Doppler shifts measured across the Venus disk (Widemann et al., 2007; Machado et al., 2014), depending on the planetocentric latitude and longitude.

This results in a spurious Doppler shift that has to be taken account. This systematic effect was first discussed by Young (1975), having proposed the empirical relation Y = 3.2 tan(SZA), where SZA is the "solar zenith angle". This effect can be modeled by averaging this expression over the aperture for each target point.

For the case of Saturn, due to the Doppler compensation from the Sun's receding and approaching limbs, the Young effect is negligible, with a contribution nearly null (less than 1 ms^{-1}) and so the account for the equation 3.7 is zero. The unbalanced solar illumination is not relevant in the case of exterior planets, relative to Earth, which is the case for Saturn.

3.5 Observations

The data used in this study was retrieved between April 18th and May 3rd of 2004, during a set of observation nights granted by ESO (Luz et al., 2004). The main purpose of these observations was to detect the differential Doppler shift introduced by the zonal wind flow in the back-scattered solar radiation from the opposite limbs (East and West) of Saturn.

Given the predicted and observed wind speed about 100 - 400 ms^{-1} (Sánchez-Lavega et al., 2003; Ingersoll et al., 1984), an absolute detection of the Doppler shift on individual solar lines is out of the question has was discussed in the previous section. At this resolution, the solar lines are well resolved. Therefore, we can make use of the wide spectral range covered by the instrument (from 480 to 680 nm) and the many solar lines it contains to apply a retrieval scheme developed for stellar accelerometry (Connes, 1985).

The observations consisted of four blocks of 15 exposures of 90 seconds each, plus two shorter blocks of nine exposures totaling 7.3 hours of telescope time. A long (25"- long) 0.3"- wide slit was positioned perpendicularly to the central meridian, moving along it at 1" intervals successively from the South pole to the northernmost observable part of the disk (since most of the northern hemisphere is occulted by the rings), in order to sample the

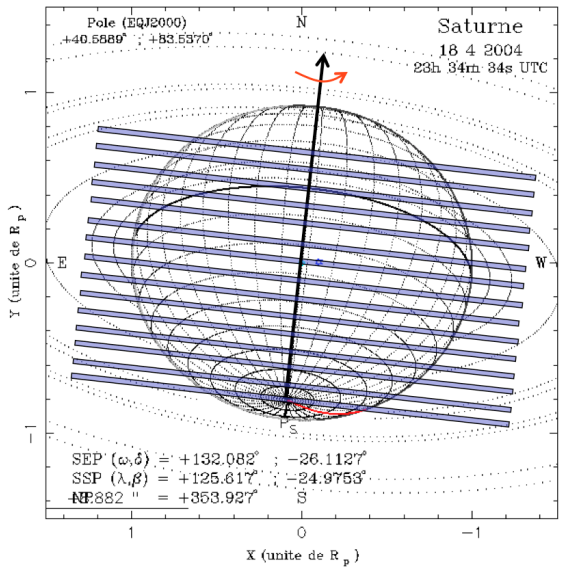

Figure 3.12: Geometry of the slit positions at the observation days. Saturn's diameter is 17.4", and the slit aperture is 0,3"×25" . The aperture offset between consecutive exposures is 1". The sub-terrestrial point is at 26.1°S.

latitudinal variation of the winds, as seen in figure 3.13.

The choice of observing dates offered the maximum angular diameter for the target and spatial resolution on the disk. It was intended to measure the latitudinal profile of the meridional and zonal winds at the cloud layer and to detect the presence of wave motions.

Night of observations	Seeing (min - max)	Airmass (min - max)	Latitudes (on central meridian)
18-04-2004	1.02 - 1.64	1.82 - 2.20	69S - 38N
19-04-2004	0.57 - 0.90	1.87 - 2.28	69S - 38N
20-04-2004	0.47 - 1.00	1.87 - 2,29	90S - 16N
21-04-2004	0.56 - 0.96	1.94 - 2.59	90S - 16N
29-04-2004	1.31 - 1.86	1.90 - 2.21	60S - 6S
01-05-2004	0.69 - 1.09	1.89 - 2.07	60S - 6S

Table 3.1: Summary of Saturn's main observations.

For Saturn, the small width of the UVES slit (and of the pixel-projected field of view), compared to the size of the disk, allows a series of high-spatial

resolution observations to be made either in the latitude or the longitude direction. Since instantaneous spatial information is preserved along the slit, the spatially varying wave motions can be separated from the zonal component (which is constant along the latitude circles) if the slit is aligned perpendicularly to the rotation axis. North-South alignment of the slit, on the other hand, allows to observe different latitude bands and will enable to retrieve an instantaneous latitudinal profile of the zonal wind.

It was used the instrument derotator in order to align the slit perpendicularly to the planetary rotation axis, starting with an exposure at one pole and to displace the slit parallel to itself, by small amounts between consecutive observations, until the other pole (or desired latitude) is reached. Along the half phase meridian, due to a compensation between the Doppler shift on the absorption solar radiation and the Doppler shift in the reemission towards the Earth-based observer, it is not possible to measure the Doppler winds parallel to the equator (zonal winds). This fact allows to measure the meridional wind along this meridian with a one-wind system approximation.

In this approach we choose as a reference, for each slit's offset position, the spectrum coming from the central pixel, which is located at the central meridian (which contains the sub-Earth point), seen that, for the points along this meridian, the zonal winds attains a zero, as was explained before. The slit was located crossing the equator at the half phase angle meridian and intersecting this meridian at a second point, either in the northern or southern hemisphere. After the slit was positioned in order to conserve a point on the same reference point and intersecting the half phase meridian at another latitude, the process was repeated for obtaining a latitudinal profile of the meridional wind measured along the half phase angle meridian.

3.6 Data Reduction

All files were produced in FITS format. Calibration files consist of *Flat Field* and *Bias* files, as well as wavelength calibration (Th-Ar lamp) files and spectral orders definition files (*Order definition frame*). All these files will be used in the data reduction process described in detail below.

From the observations described in (Luz et al., 2004) I had at my disposal five observation days: April 20th, 21st and 29th, and May 1st and 2nd. The *science* fits files of the fourth day (May 1st) shows that they are over-exposed, and due to that, they were discarded from this study. On the

last day, the slit was positioned in parallel to the planet's rotation axis in three positions, for validations purposes, as explained in section 3.5. So, for this work, I choose to select the first three days.

One important aspect I had to deal with at the very beginning was the size of the slit's active window, and so, the number of pixels (within the total size of 97 pixels, or 25", in each slit) I would effectively use in this approach. That was due to the fact that, as we can see in figure 3.13, the motions seen at the edges of the slit are affected by the presence of the rings that leads to a severe order superposition, even for the 25" aperture used. Therefore, I had to, carefully, discard a certain number of outer pixels, according to the latitude of the slits.

On the other hand, defects in the response of the UVES slit in the upper part excludes its use for accurate Doppler measurements such as these. After navigating the slit position over the planetary disk, I discarded the pixels on the detector that were sounding out of the planet, and, in the northern hemisphere, at high latitudes, we had the issue of rings super-imposing the planetary disk image. Those pixels sounding rings+planet were discarded because calculating Doppler velocities over rings is out of the framework of the study.

Another matter is the influence that the south polar vortex had and how it could distort the data for the southern slits (with a planetocentric latitude above $\sim 75^\circ$ S). In order to minimize the effect that this might have, I opted to discard the three slits that were near the polar region (slit positions 1, 2 and 3), working with the other twelve (from slit position 4 to 15).

On the table 3.2 I summarize the number of pixels of the slit's active window for each position.

Slit position	No of pixels
4	51
5	81
6	81
7	91
8	97
9	97
10	97
11	91
12	81
13	81
14	51
15	41

Table 3.2: Number of pixels of the slit's active window at each position, as is explained above.

3.6.1 Spectra Obtainment

From the raw fits *echellogramme*, I retrieved the high resolution spectra from the MIT and EEV CCD detectors (their properties are shown on table 3.3), according to the sequence of steps shown in figure 3.13.

CCD	Number of spectral orders	Wavelength coverage (nm)
MIT	16	478 - 575
EEV	23	584 - 680

Table 3.3: Specifications of the UVES's ccd detectors

3.6.2 *Bias, Flat and Lamp*

The data were first de-biased and flat-fielded based on sets of five bias and five flat-field images obtained on each night of observation. Master bias and master flats were constructed by computing the median of each set. Then that median was subtracted from the science images. Wavelength calibration observations were made with a built-in Thorium-Argon lamp. I fed the pipeline with those observations in order to obtain a 1D spectra, where the lines from Th-Ar are well known. This allowed producing a dispersion

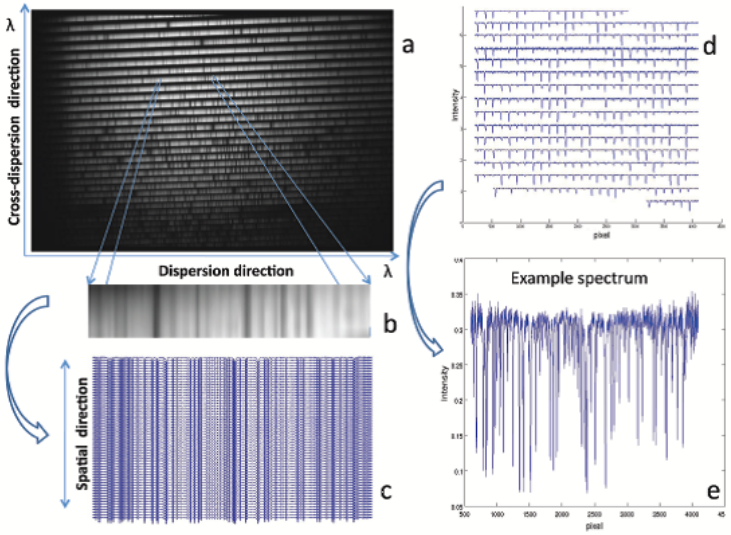

Figure 3.13: Steps for obtaining spectra from a UVES *echellogramme*. (a) Raw *echellogramme* showing the spectral orders for one of the detectors. (b) Magnification of part of one order, where absorption lines (dark vertical bands) are visible. From each order, a stack of 61 spectra are extracted. (c) Set of 61 spectra, with each one corresponding to one pixel in the slit's active window. (d) Each spectrum is divided into 16 orders in the MIT detector and 23 orders in the EEV detector. The plot shows an example of the 16 components of an MIT spectrum, each coming from one spectral order. (e) Example spectrum from one order and one location in the Venus disk(Machado et al., 2012).

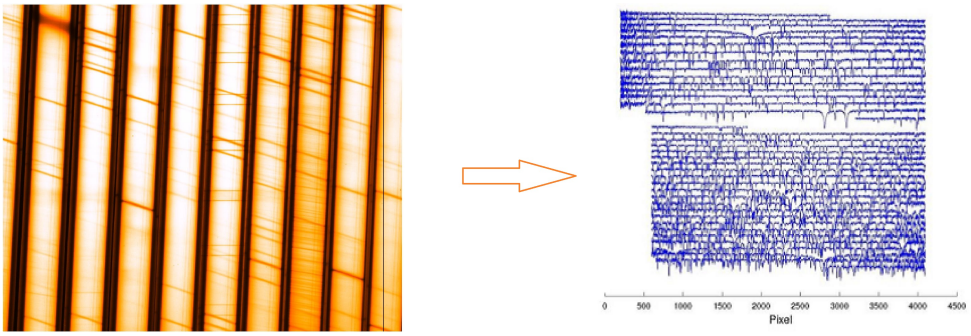

Figure 3.14: Example of a high resolution spectrum that I obtained from the *echellogramme* (on the left side of the image). We can see the 16 spectral orders from the EEV detector (right and above in the figure), and the 23 spectral orders from MIT detector (bottom right).

relation function through an interpolating process, yielding a high resolution correspondence between each pixel along the 1D retrieved spectra, from *science* observations, and its respective wavelength given by the dispersion relation function.

3.6.3 Doppler Retrieval

Having constructed the spectra for each slit position from the *science* data files, I used the scripts from the MATLAB package mentioned before, to extracted the Doppler shifts at each pixel of each slit (see figure 3.15). Once that was complete I converted the pixel positions of the slit in longitude (see figure 3.16), according to the convention used by Machado et al. 2012.

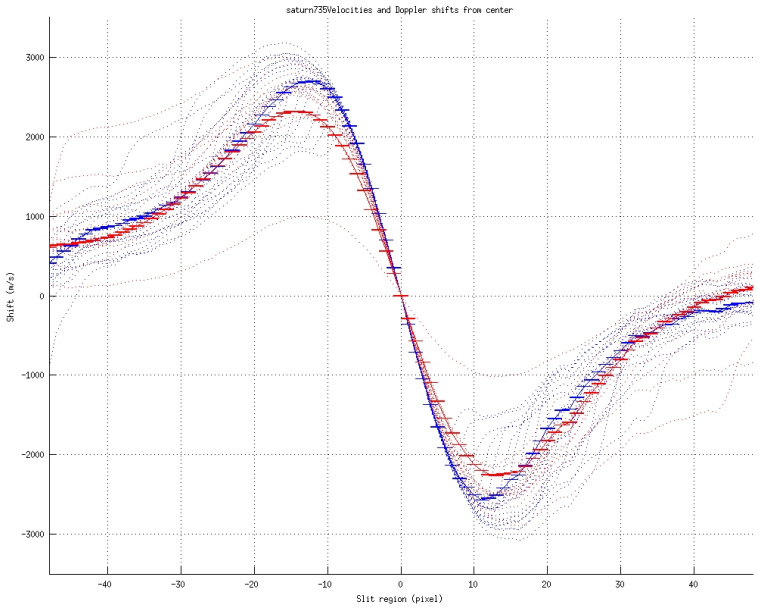

Figure 3.15: Retrieved relative Doppler shift for each pixel surveying the long slit, with the central pixel passing on the planetary equator. EEV detector on blue and MIT detector on red in the figure. The measured Doppler shifts are along the line-of-sight from Earth.

I used the pipeline I adapted from Machado et al. 2012 (based on the Connes (1985) method) in order to obtain the Doppler velocity at each location sounded upon the planetary disk (equations 3.4 and 3.5). Then I applied equation 3.8 to make the de-projection of the shifts from the line-of-sight of

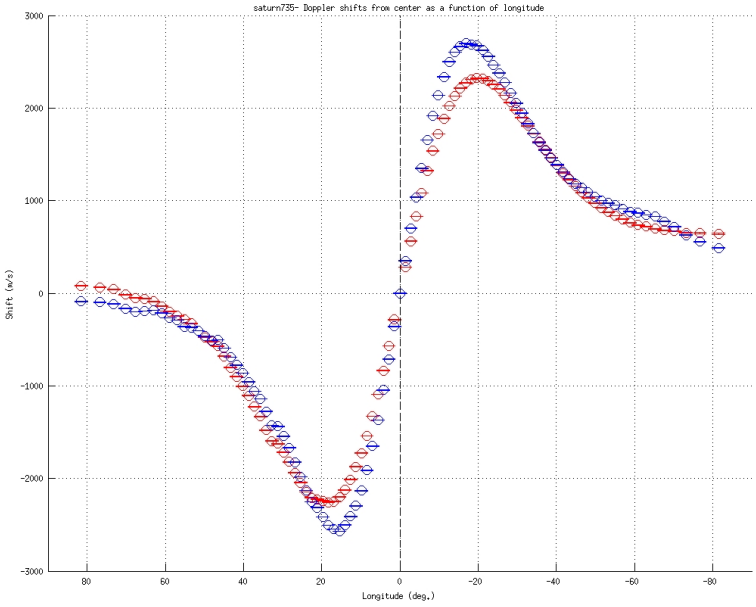

Figure 3.16: This figure shows the Doppler shifts obtained in the previous step, but now as a function of the sub-Earth longitude of Saturn. The correspondence pixel-longitude was made based on the spherical geometry of Saturn. In one of the scripts (*getlatton.m*) I used the specific observations' geometry for yielding the correspondence between each detector's pixel (along the slit) at each offset, in order to calculate the latitude and sub-Earth longitude of each pixel upon the planetary disk. The zero longitude is by convention at the sub-Earth point meridian, that is in the middle of the disk.

the observer, in order to compute the overall planetocentric Doppler shifts (the values obtained include the account for the rotation velocity of Saturn) from both MIT and EEV CCD detectors. This was also done to the average of the two CCD contributions. The following crucial step was to subtract the approximated contribution of the rotation velocity along the slits and its variation throughout the large range of latitudes used.

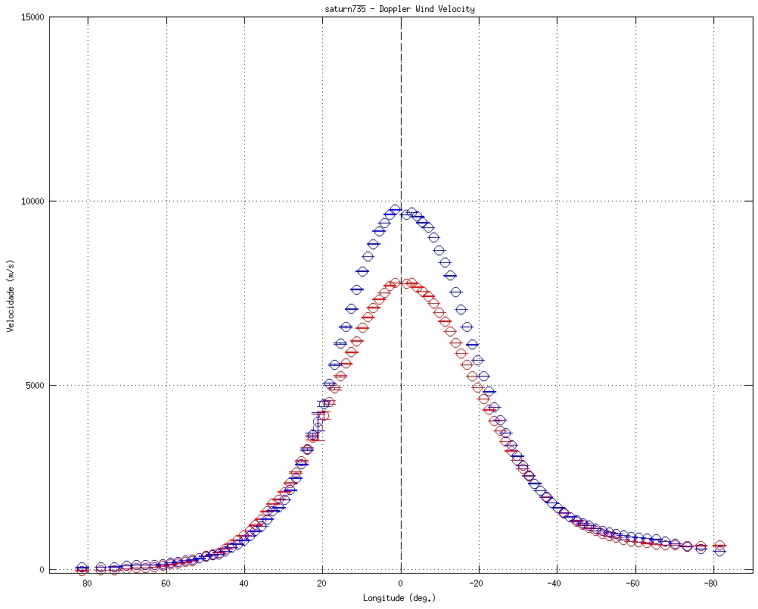

Figure 3.17: Overall planetocentric Doppler shifts for each CCD detector, de-projected from the line-of-sight. EEV detector on blue and MIT detector on red in the figure.

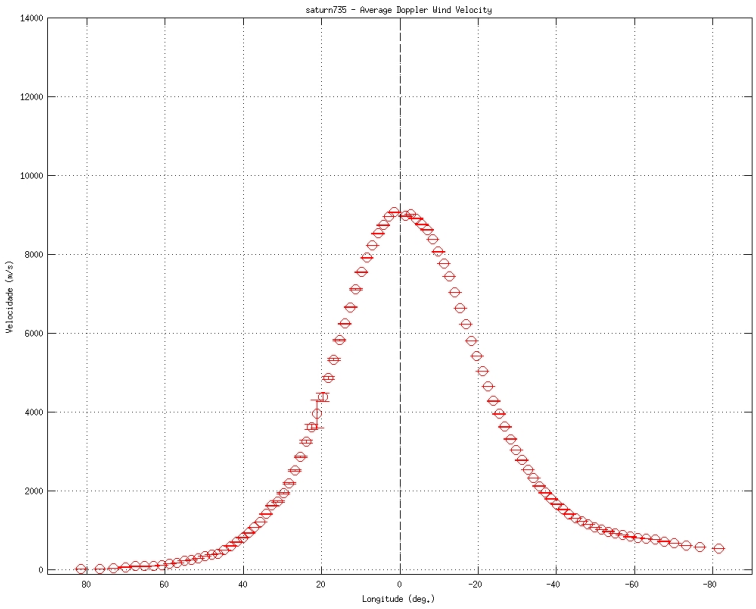

Figure 3.18: Overall planetocentric Doppler shifts, due to body rotation and wind motions, averaging the two CCD contributions. Note that, in both images, the rotation velocity that dominates the retrieved overall velocity.

3.6.4 Modeling the retrieved planetocentric Doppler shifts

The reason for modeling the overall retrieved Doppler shift came from the spatial and temporal variability of Saturn's rotation, as discussed in subsection 2.3.1, namely the fact that Saturn presents a significant difference at the rotation rate between Systems I and II. I thought I might address the issue of Saturn's rotation rate (in fact, a major issue in the planet's global dynamics, and in constant re-analysis). For that, I modeled the best fit for the retrieved overall planet, for both the MIT and EEV detectors and also for their weighted average, at each slit position at each observation day used.

Besides the fact that the Doppler velocities obtained are due to Saturn's rotation rates and wind motions simultaneously, that will be impossible to completely disentangle the two Doppler shift sources. Nevertheless, I thought that it will be important, at this stage, to have a first order approximation to the combined velocities of the Doppler wind and the body's rotation rate along the slit's position.

3.6.5 Correction of the retrieved overall Doppler shifts from the rotation rate

I used the bulk rotation rate provided by Cassini (System III), as discussed, and I subtracted the line-of-sight planetary rotation velocity, taking into account the latitude and sub-Earth longitude at each pixel on the slit. This correction had to be done pixel by pixel, regarding the variability of the latitude and the high variability of the sounded sub-Earth longitude along the slit's active window. The values obtained for the Doppler velocities, as I described in section 3.4 (and based on Machado et al. 2012 method), can be higher than 500 ms^{-1} near the equator and lower than 300 ms^{-1} at high latitudes as we can see in figure 3.19.

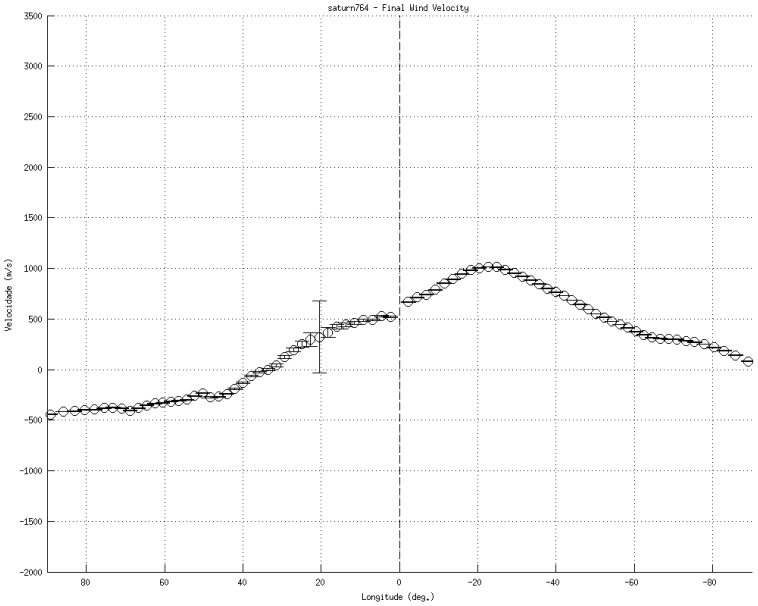

(a)

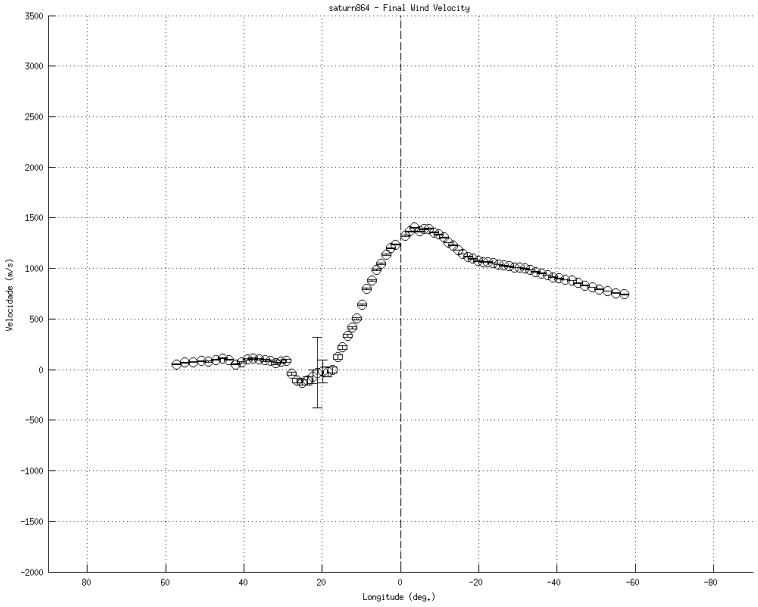

(b)

Figure 3.19: Average of the Doppler wind velocities at two slits on the first day of observations. (a) low latitude: $\overline{v} \sim 270 ms^{-1}$ (b) high latitude, near equator: $\overline{v} \sim 664 ms^{-1}$.

3.6.6 Sensitivity Tests (synthetically reconstructed spectra tests)

In order to test the robustness, reliability and sensitivity of the Doppler velocimetry algorithm used, I performed additional sensitivity tests. The factors studied were: the line's density, depth and asymmetry level, the accuracy in the retrieved velocities as a function of the size of the deviations imposed and the algorithm wavelength sensibility response.

With the aim of improving the quality and increase the confidence in the results obtained, I built synthetic spectra to which I imposed artificial shifts corresponding to known velocities. Then we ran the algorithm to produce the respective velocity curves and compared the velocities retrieved and the imposed ones. The tests included the modeling of fully synthetic spectra as well as modified actual observational data to which artificial Doppler shifts were imposed (from now on denominated "synthetically reconstructed spectra").

With the goal of testing the robustness of the data reduction algorithm, I used synthetic spectra (Machado et al., 2012), in order to study the pipeline response to the imposed velocities on the synthetic spectra. I then obtained the velocity curves for these changed spectra.

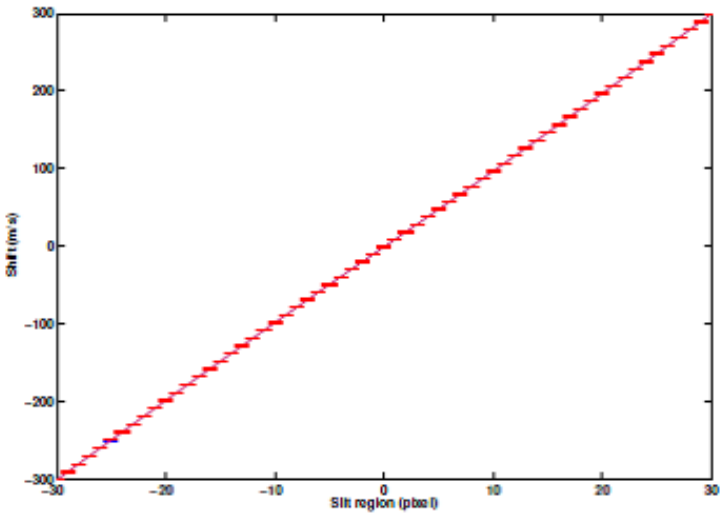

Figure 3.20: Doppler shift curve for spectra shifted with an ∼10 ms^{-1} step relative to the central spectrum, between -300ms^{-1} and 300ms^{-1}. This curve has been retrieved from a synthetic spectrum.

First of all, I obtained the dispersion relation which gave us the correspondence of each pixel position at each slit's offset, in the 1D retrieved spectra and its correspondent calibrated wavelength. I chose an observation (with high signal to noise ratio), and then, I replaced all the spectra coming from all the pixels, from the one coming from the pixel at slit's center (to confirm that the algorithm produces the zero relative velocity in relation of the central pixel). I then used these reconstructed data as input to the pipeline's algorithm.

In the first test, the initial step consisted of replacing all the 61 spectra by the central spectrum, to ensure a relative null velocity between each of the spectra and the reference spectrum. The algorithm retrieved null Doppler shifts, as expected. In the second test all the spectra except the reference one were shifted by a prescribed shift. The spectra were shifted with $10 \sim ms^{-1}$ increments, between $\sim$ -300 ms^{-1} and $\sim$ 300 ms^{-1} from top to bottom of the slit. Then I have produced the velocity curves for these changed spectra. This test confirmed that the velocity curves for the reconstructed spectra were consistent with the imposed deviations (see figure 3.20).

To test the algorithm's response to the wavelength range, reconstructed spectra were also produced in which only one of the spectral orders was reconstructed as previously described, while all other orders were replaced by an average of the continuum level. Since there was no significant discrepancy between velocity curves obtained from different spectral orders, I concluded that the method is robust with respect to the wavelength range of the data. This is not surprising since the density of spectral lines has little variation between spectral orders.

3.6.7 Results

As we can see in figure 3.16, where is shown the Doppler shift as function of the sub-Earth longitude, at west from sub-Earth point, the Doppler shifts are negative (which means that they are blue-shifted in relation to the central meridian) and in the eastern direction, we have positive Doppler shifts (red-shifted relatively to the reference central meridian).

This is obviously in agreement with the prograde Saturn's rotation and seeing that the rotation rate is, by far, the most prominent contribution to the overall Doppler shift retrieved (9690 ms^{-1} at equator). Obviously, at that stage, the measured Doppler shifts were from the line-of-sight of ground-

based observations on Earth (VLT, Atacama desert).

As was explained previously, on the next data reduction steps, I deprojected from the line-of-sight, considering a zonal wind motion, which means a wind parallel to the equator, as the planet's rotation velocity is also parallel to the equator, and the subsequent step was the subtraction of the planet's rotation velocity at each latitude sounded (i.e. the planetocentric coordinates associated to each pixel along the slit, sounding the planet).

In this section, I present the results from the first day of observations (April 20th) for two different slit's offset upon the planetary disk. I used data from the MIT detector, the EEV detector and a weighted average of both, displayed in sets of four images for each slit position at each of the three days that were analyzed. I decided to present on this way regarding that the Doppler velocities measured can't be yet considered wind velocities because there is still a lot of work to do until I can state that. The related considerations are explained in "Conclusions and Outlook".

Comparing the results from the first set of presented results from the first day, at slit positions 5 (see the scheme of observations at figure 3.21 (b) - System II, where the slit's central point is at 60° S), and the second set of observations are from the slit's offset number11, near the equator (see the scheme of observations at figure 3.22 (b) - System I, where the slit's central pixel is at 15° S), it is clear the higher average velocity for the slit position in System I than in System II. This is consistent with the literature and previous observations (Sánchez-Lavega et al., 2007), and, as expected, we can note the presence of an equatorial jet at low latitudes (System I), and considerably lower velocities at higher latitudes (System II). This considerations are qualitative ones, at this stage.

On figures 3.21 (b) and (c) as well on figures 3.22 (b) and (c), we can see the Doppler velocities retrieved, respectively with the MIT and EEV CCD detectors. On figures 3.21 (a) and 3.22 (a), I present the weighted average from the two CCDs.

We can observe that the EEV CCD detector (that covers the wavelength range from 478 - 575 nm) shows systematically higher velocities than the MIT CCD detector (that covers the wavelength range from 584-680 nm). The measured Doppler shifts along the slit show relevant spatial variability and, more than that, a different behavior measured from each detector CCD (this issue will also be addressed in the next section). The average wind ve-

locities obtained for each slit are consistent with cloud tracked wind results coming from Cassini mission (Sánchez-Lavega et al., 2007; García-Melendo et al., 2011; Hueso et al., 2012; Mousis et al., 2014).

However, the average results from this work, presented in table 3.4 are, in general, slightly higher than the cloud tracked results. Nevertheless is clear, that the average Doppler velocities coming from the equator and low latitudes (slit positions from 11 to 15) are striking higher than the ones coming from higher latitudes (slit positions from 4 to 10). These issues will be addressed in the next section.

The complete set of Doppler velocity results (zonal winds) for the three days of observations (April 20t, 21st and 29th) are presented in an appendix to this work (Appendix A). The overall set of results are presented with the same approach than in the ones presented in this section. I invite the reader to confirm that the Doppler velocities measured in the second day of observations are significantly higher than in the first and third days, which are consistent with each other. The reason for that will be discussed in the following section.

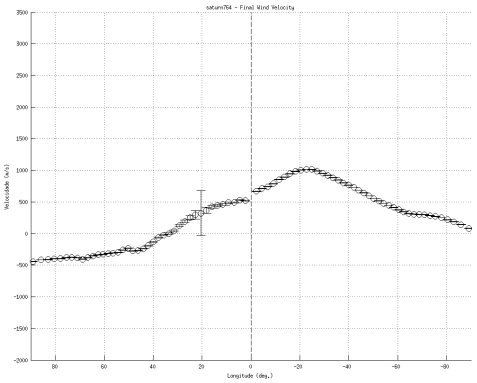

(a)

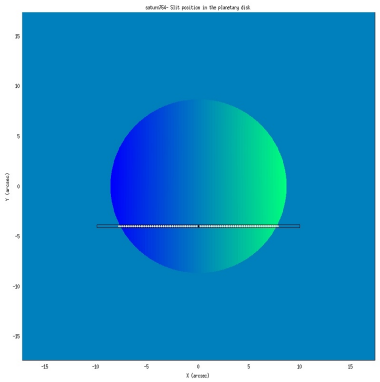

(b)

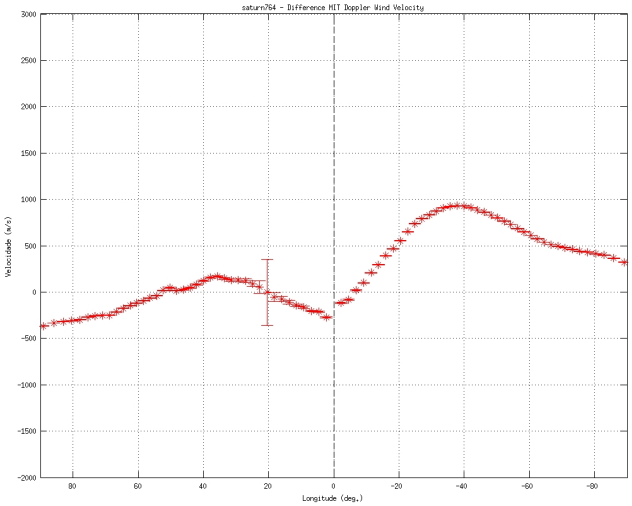

(c)

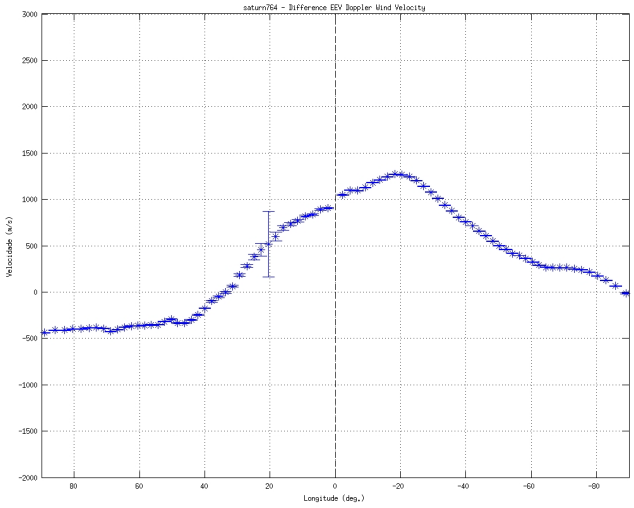

(d)

Figure 3.21: (a) Weighted average of the MIT and EEV Doppler velocities for a high latitude slit position 5: $\overline{v}_{med} = 270ms^{-1}$; (b) Scheme of the position of the slit on the planetary disk; (c) MIT detector Doppler velocities: $\overline{v}_{MIT} = 231ms^{-1}$; (d) EEV detector Doppler velocities: $\overline{v}_{EEV} = 322ms^{-1}$.

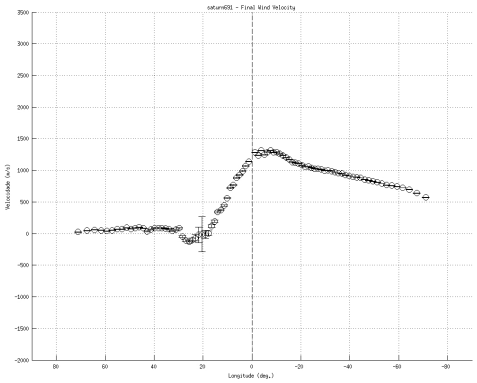

(a)

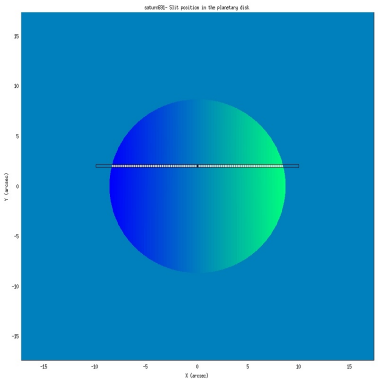

(b)

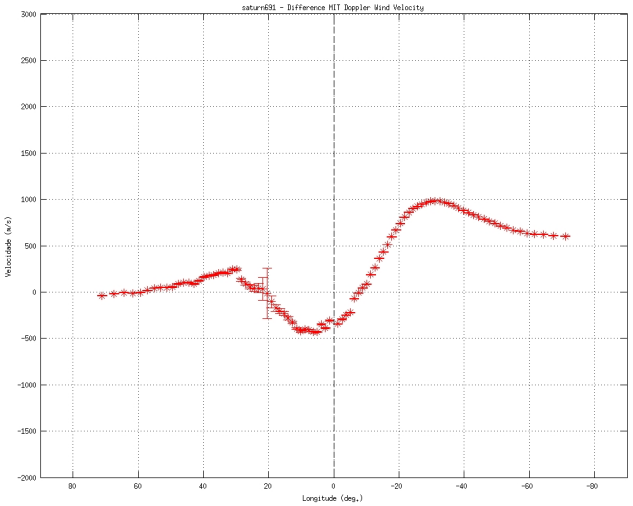

(c)

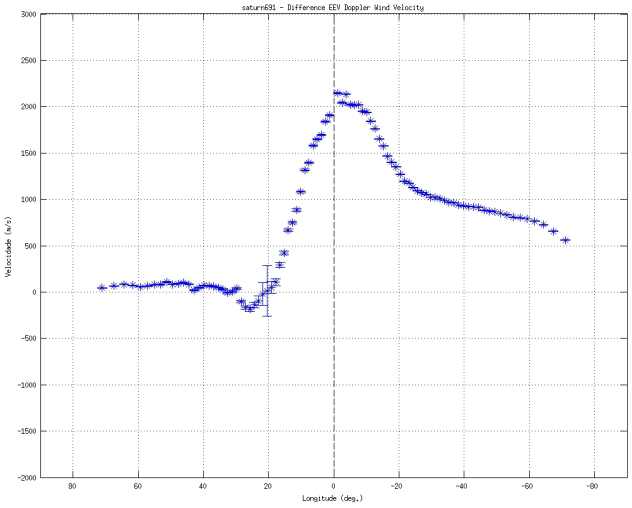

(d)

Figure 3.22: (a) Weighted average of the MIT and EEV Doppler velocities for a low latitude slit position 11: $\overline{v}_{med} = 608ms^{-1}$; (b) Scheme of the position of the slit on the planetary disk; (c) MIT detector Doppler velocities: $\overline{v}_{MIT} = 264ms^{-1}$; (d) EEV detector Doppler velocities: $\overline{v}_{EEV} = 787ms^{-1}$.

For a better understanding of the dimensions of the retrieved Doppler velocities, and for comparison purposes between each day, here I put together all the average velocity values extracted from the images in Appendix A.

	Day 1 (20-4-2004)			Day 2 (21-04-2004)			Day 3 (29-04-2004)		
Slit Position	v_{MIT}	v_{EEV}	v_{med}	v_{MIT}	v_{EEV}	v_{med}	v_{MIT}	v_{EEV}	v_{med}
4	116	222	180	215	399	337	91	259	171
5	231	322	270	304	388	386	137	309	257
6	226	496	389	362	702	605	188	282	252
7	239	513	404	458	953	780	260	309	297
8	294	597	467	441	951	871	258	352	308
9	264	657	504	461	627	542	308	435	396
10	227	719	539	477	1084	896	240	470	366
11	264	787	608	486	1129	917	280	570	419
12	247	826	664	488	1203	1000	137	516	366
13	253	797	614	446	1284	1044	-	-	-
14	137	758	670	273	1381	1310	-	-	-
15	125	850	721	495	1882	1864	-	-	-

Table 3.4: Doppler velocities values (given in ms^{-1}) for MIT and EEV CCD's and median for each slit position on the first 3 days of observations.

3.7 Discussion

On a first view of the results, we can observe that the Doppler velocities computed for the EEV detector are higher that the MIT ones, on every observation day. The slit position 9 is the one which the central pixel coincides with the sub-Earth point, and the slit position 13 has its central pixel passing on the planet's equator. In each day of observations, we can note the presence of an equatorial jet at low latitudes (slit positions 11 to 15), where the average Doppler velocity measured along the slit is significantly higher (over 500ms^{-1}) than the much lower average velocities (below 300ms^{-1}) of higher latitudes (slit positions 4 to 10).

The MIT velocities are below 300 ms^{-1}, with the exception for the second day of observations. On the other hand, the EEV velocities reach above 500 ms^{-1} in almost every slit position in the first and second days. In comparison

with the first day data, the second day presents higher velocities, whereas the third day show slightly lower values. EEV velocities (and subsequently, also the median velocities) for low and average latitudes are well above the expected from the state of the art.

The composition of Saturn's atmosphere includes a considerable amount of methane (and in a lower degree, ammonia), the spectra where I based this work includes Fraunhofer lines from the back-scattered solar radiation, but also, Saturn's absorption lines from CH_4 and NH_3, and Earth-atmosphere's telluric lines as well. The line formation altitude is, in fact, a radiative transfer problem, and both methane and ammonia lines are formed in upper layers of Saturn's atmosphere.

An important feature that is clear from results is a discrepancy between MIT and EEV Doppler velocities. One reason for that is the different optical depth "covered" by each detector, since they cover different wavelength ranges (478 - 575 nm and 584 - 680 nm, respectively). Given that the optical depths surveyed are different, that corresponds to distinct pressure levels, and so, different altitudes for the two detectors.

Based on the detector coverage, the MIT CCD is more affected by the methane lines (and there is also a smaller contribution from the ammonia ones), changing the measured overall Doppler shifts. In many measurements, the MIT CCD detected some negative values for the Doppler winds, which may be some contribution from higher levels of the atmosphere that could rotate in the opposite direction of the upper layers.

On those layers, the velocities associated to this chemical compound are higher than the ones from the Fraunhofer lines contribution. That matches what we can see in our EEV and MIT detectors results because there are important rotovibration methane absorption bands (resolved in lines 619, 667 and 683 nm), ammonia absorption bands at 645 nm, and hydrogen (H_2) quadrupolar lines at 636.77 and 643.5 nm.

Seeing that the Doppler shifts from absorption lines differ from Fraunhofer lines, and that the line formation levels in the atmosphere (aerosol/cloud-model dependent) are higher than atmosphere for solar back-scattering altitude level, the contamination of absorption lines in the spectra produces a different velocity which explains the higher results measured by the EEV detector (478 - 575 nm). Please see, the "Prospects and future work" section, where I describe the next steps for resuming this work.

The values attained are in general agreement with previous results retrieved using cloud tracking (Sánchez-Lavega et al., 2007; García-Melendo et al., 2011; Hueso et al., 2012; Mousis et al., 2014). It is evident that the velocities are higher on the equatorial zone (System I), decrease with the latitude and are clearly lower at high latitudes (System II), as expected from previous measurements of cloud tracked winds.

Due to the Saturn's axis inclination in the line-of-sight of the observer of about $-26,1°$, as seen in figure 3.12, the slit is not placed at the parallel of the planet. The consequence is that, according to the spherical geometry, each slit position we are not looking at a single latitude but to a range of different latitudes which makes that the values for the Doppler winds have contributions from more than the latitude of the central pixel at the each slit offset location.

A final remark focus on the fact that we are not looking at the same region of Saturn's disk in all the observation days. Attending that the average rotation period is approximately 10h45m and that the first two days have a $\sim 24h$ separation, in that time Saturn completes approximately 2,25 rotations and so, on the second day we see the disk of Saturn with a $\sim 90°$ shift. On the third day (nine days after the first observation), Saturn has completed just a little more than 20 complete rotations, and so, we can assume that the instrument was looking at roughly the same regions as in the first day of observations.

Chapter 4

Conclusions and Outlook

4.1 Conclusions

This is the first time that Doppler velocimetry, based on long-slit spectroscopy, applied to the visible, enables a first attempt to collect the ground-based direct measurements of the instantaneous zonal winds of Saturn, across a wide range of latitudes and local times and to determine the presence of local variations relative to the average of the latitudinal profile of winds on the atmosphere of Saturn. However, it is crucial to state that, at this stage, I don't present this results as wind velocities yet, but as Doppler velocities.

The combination of the 8-meter class Very Large Telescope, UT2 with the UVES spectrograph allowed the retrieval of the solar Fraunhofer lines in Saturn's scattered spectrum with a spectral resolution of $\sim 10^5$ in the visible range. The Doppler velocities retrieved by the pipeline had a precision of a few ms^{-1} (but depending on the signal-to-noise ratio), however, as discussed before in the previous section, at this stage I can't claim that the Doppler velocities are, in fact, wind velocities. Certainly, the future steps in order to retrieve the true instantaneous zonal winds will propagate errors and final results will show lower precision. The results found are qualitatively in a good agreement with the most recent cloud tracking observations.

The fact that we are measuring instantaneous velocities will allow, in the future, the possibility to detect planetary waves, storms and, most importantly, spatial and temporal variability. Doppler velocities' preliminary results are promising but the determination of the wind velocity will however, require an accurate determination of the probed pressure levels and contributions from planetary absorption lines at different altitude levels.

4.2 Prospects and future works

In the near future, I intend to perform the appropriate subtraction of the spectra of the Saturn's rings from the spectra of Saturn itself, in order to obtain the contribution from the planetary absorption, leading to the obtainment of the spectra with only the back-scattered solar Fraunhofer lines. On the other hand, I will use the retrieved velocities of the inner and outer part of the rings with this velocimetry method, and I will compare with the values of this known keplerian velocities in order to have an extra confirmation of the robustness ans reliability of the method.

In the next steps, I will "feed" this velocimetry method, that I adapted for Saturn, with the spectra clean from the spurious contamination of methane (and other compounds such as ammonia and hydrogen). At that time, I will have the wind velocity results ready to publish. On the other hand, as a follow up of this study, I intend to use the spectra wit only the contribution from the planet (absorption lines) to feed again into the velocimetry pipeline, in order to retrieve velocities from a different pressure level (altitude), which will help to constrain the vertical wind sheer.

For that, I will need to take advantage of a Saturn's radiative transfer study/model as the one from Patrick Irwin, from Oxford University, shown in figure 4.1, in pursuance of estimating the altitude levels that will be sounding for that particular case of methane absorption.

Because this observations' run took place some months before the Cassini mission arrival to Saturn, I plan to use Saturn Cassini images, so I can obtain wind velocities by the method of cloud features tracked along the time (could tracking), to compare with the Doppler velocities retrieved. Our group possesses in this moment the cloud tracking tools, the Cassini data archive and the knowledge of how to dig in it.

I, myself, have learned the cloud tracking technique with Sánchez-Lavega team in the middle of June, 2016.

I have the intent and motivation to proceed my work on this subject, considering that this is a strong opportunity to collaborate with JUNO mission (I have received a support letter from its PI), intervene in the study of exoplanets and, most of all, further explore the uniqueness and the pioneer character of this research.

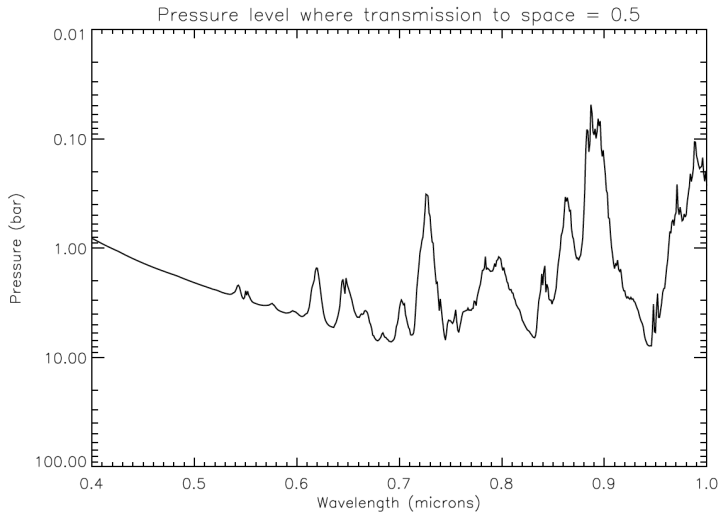

Figure 4.1: Saturn transmission at visible wavelengths with the respective atmospheric pressure levels trough the visible and near-infrared wavelengths. (Source: Patrick Irwin (Oxford University), private communication)

Bibliography

Anderson, J. D., Schubert, G., Saturn's gravitational field, internal rotation and interior structure. Science 317 (5843): 1384-1387, 2007.

Benton, Julius, Saturn and how to observe it. Astronomers' observing guides, 11th ed.. Springer Science & Business. p. 136. ISBN 1-85233-887-3, 2006.

Cain, Fraser, History of Saturn, Universe Today, 2008.

Civeit, T. et al., On measuring planetary winds using high-resolution spectroscopy in visible wavelengths, Astronomy and Astrophysics, volume 431, p. 1157-1166, 2005.

Connes, P., Absolute astronomical accelerometry, Astrophysics and Space Science (ISSN 0004-640X), volume 110, no. 2, p.211-255, 1985.

De Groot, Jan Jakob Maria, Religion in China: universism. A key to the study of Taoism and Confucianism, American lectures on the history of religions 10 (G. P. Putnam's Sons), p. 300, 1912.

Dekker, H., D'Odorico, S., Kaufer, A., Delabre, B., Kotzlowski, H., Design, construction, and performance of UVES, the *echelle* spectrograph for the UT2 Kueyen Telescope at the ESO Paranal Observatory, Proc. SPIE Vol. 4008, p. 534-545, Optical and IR Telescope Instrumentation and Detectors, Masanori Iye, Alan F. Moorwood; Eds, 2000.

Del Genio, A.D., R.K. Achterberg, K.H. Baines, F.M. Flasar, P.L. Read, A. SÃ¡nchez-Lavega, and A.P. Showman, 2009: Saturn atmospheric structure and dynamics. In Saturn from Cassini-Huygens. M.K. Dougherty, L.W. Esposito, and S.M. Krimigis, Eds. Springer-Verlag, 113-159, doi:10.1007/978-1-4020-9217-6_6.

Dorn, Reinhold J.; Beletic, James W., Cavadore, Cyril, Lizon, Jean-Louis, Optical detector systems of UVES: the *echelle* spectrograph for the UT2 Kueyen Telescope at the ESO Paranal Observatory, Proc. SPIE Vol. 4008,

p. 344-355, Optical and IR Telescope Instrumentation and Detectors, Masanori Iye, Alan F. Moorwood; Eds, 08/2000.

Dougherty, M.K., Esposito, L.W., Krimigis, S.M., Saturn from Cassini-Huygens, Saturn from Cassini-Huygens (Springer), 162, 2009.

Evans, James, The History and Practice of Ancient Astronomy, Oxford University Press, pp. 296-7, 1998.

Gabsi, Y. et al., Measuring Venus winds using the Absolute Astronomical Accelerometer: Solid super-rotation model of Venus clouds. Planetary and Space Science, volume 56, p. 1454-1466, 2008.

García-Melendo, E., Sánchez-Lavega, A., Pérez-Hoyos, S., Hueso, R., Saturn's wind profile from Cassini ISS images and its long term variability, id. EPSC2011-453, 2011

García-Melendo, E., Legarreta, J., Sánchez-Lavega, A., Non-linear simulations of Saturn's 2010 Great White Spot, id. EPSC2012-298, 2012

Hamilton, Calvin J., Voyager Saturn Science Summary, Solarviews, 1997.

Holton, J., An introduction to dynamic meteorology, (Academic Press), 2004.

Hueso R., Legarreta J., Rojas J.F., Peralta J., Pérez-Hoyos S., Del Río-Gaztelurrutia T. and Sánchez-Lavega A.: The Planetary Laboratory for Image Analysis (PLIA). Advances in Space Research, 46, 1120-1138, 2010.

Hueso R., Sánchez-Lavega, A., del Río-Gaztelurrutia T., Dynamics of Saturn's Great White Spot observed by Cassini ISS, European Planetary Science Congress 2012, id EPSC2012-235, 2012

Ingersoll, A.P., Beebe, R.F., Conrath, B.J., Hunt, G.E., Structure and dynamics of Saturn's atmosphere, University of Arizona Press, 1984

Karkoschka, Erich, Spectrophotometry of the Jovian Planets and Titan at 300 to 1000 nm wavelength: The Methane Spectrum, Icarus 111, p. 174-192, 1994.

Kostiuk, T. et al., Direct measurement of winds on Titan. Geophysical Research Letters, volume 28, p. 2361-2364, 2001.

Kostiuk, T. et al., Titan's stratospheric zonal wind, temperature, and ethane abundance a year prior to Huyghens insertion, Geophysical Research Letters, volume 32, p. 4, 2005.

Lewis, J. Physics and Chemistry of the Solar System, Elsevier Academic Press, 2004.

Luz, D. et al. Characterization of zonal winds in the stratosphere of Titan with UVES, Icarus, volume 179, p. 497-510, 2005a.

Luz, D. et al. Characterization of zonal winds in the stratosphere of Titan with UVES: 2. Observations coordinated with the Huygens Probe entry, Journal of Geophysical Research, volume 111, CiteID E08S90, 2006.

Luz, D., Courtin, R., Gautier, D., Lebreton, J.P., Witasse, O., Appourchaux, T., Kaufer, A., Ferri, F., Lara, L., Scientific Proposal-ESO, 2004.

Machado, P., Luz, D. Widemann, T., Lellouch, E., Witasse, O, Characterizing the atmospheric dynamics of Venus from ground-based Doppler velocimetry, Icarus, Volume 221, p. 248-261, 2012.

Machado, P., Widemann, T., Luz, D., Peralta, J., Wind circulation regimes at Venus' cloud tops : Ground-based Doppler velocimetry using CFHT/ESPaDOnS and comparison with simultaneous cloud tracking measurements using VEx/VIRTIS in February 2011, Icarus, 2014.

Martic, M. et al., Evidence for global pressure oscillations on Procyon. Astron. Astrophys., volume 351, p. 993, 1999.

Martic, M.; Lebrun, J.-C.; Schmitt, J.; Lebreton, J.-P.; Appourchaux, T., Feasibility demonstration of Titan wind measurement technique at OHP using absolute accelerometry method. Technical report, Observatoire de Haute Provence, 2001.

Moore, Patrick, The 1990 Great White Spot of Saturn, London: W.W. Norton & Company, pp. 176-215, 1992.

Moreno, F., Rodrigo R., Sánchez-Lavega, A., Molina, A., Spectroscopic observations of the $CH_4 - 6190$Åand $NH_3 - 6450$Åabsorption bands at different regions of the jovian disk, A&A, 74, 233-238, 1988

Mousis, O., Fletcher, L. N., Lebreton, J.-P., Wurz, P., CavaliÃ©, T., Coustenis, A., Courtin, R., Gautier, D., Helled, R., Irwin, P. G. J., Morse, A. D., Nettelmann, N., Marty, B., Rousselot, P., Venot, O., Atkinson, D. H., Waite, J. H., Reh, K. R., Simon, A. A., Atreya, S., AndrÃ©, N., Blanc, M., Daglis, I. A., Fischer, G., Geppert, W. D., Guillot, T., Hedman, M. M., Hueso, R., Lellouch, E., Lunine, J. I., Murray, C. D., O'Donoghue, J., Rengel, M., SÃ¡nchez-Lavega, A., Schmider, F.-X., Spiga, A., Spilker,

T., Petit, J.-M., Tiscareno, M. S., Ali-Dib, M., Altwegg, K., Bolton, S. J., Bouquet, A., Briois, C., Fouchet, T., Guerlet, S., Kostiuk, T., Lebleu, D., Moreno, R., Orton, G. S., Poncy, J., Scientific rationale for Saturn's in situ exploration, Planetary and Space Science, Volume 104, p. 29-47, 2014.

D'Odorico, Sandro; Cristiani, Stefano; Dekker, Hans; Hill, Vanessa; Kaufer, Andreas; Kim, Taesun; Primas, Francesca: Performance of UVES, the *echelle* spectrograph for the ESO VLT and highlights of the first observations of stars and quasars, Proc. SPIE Vol. 4005, p. 121-130, Discoveries and Research Prospects from 8- to 10-Meter-Class Telescopes, Jacqueline Bergeron; Ed,(2000).

Orton, G.S., Ground-Based Observational Support for Spacecraft Exploration of the Outer Planets, Earth, Moon, and Planets 105, 143-152, 2009.

Pater, I.; Lissauer, J., Planetary Sciences, Cambridge University Press, 2001.

Peralta, J., Hueso, R., Sánchez-Lavega, A., A reanalysis of Venus winds at two cloud levels from Galileo SSI images, Icarus, 190, 469-477, 2007.

Peralta, J., Sánchez-Lavega, A., López-Valverde, D., Luz, D., Machado, P., Venus's major cloud feature as an equatorially trapped wave distorted by the wind, Geophysical Research Letters, Volume 42, Issue 3, pp. 705-711, 2015.

Pérez-Hoyos, S., Sánchez-Lavega, A., French, R. G., J. F., Saturn's cloud structure and temporal evolution from ten years of Hubble Space Telescope images (1994-2003), Icarus 176 (1), 155-174, 2005.

Pérez-Hoyos, S.; Sánchez-Lavega, A.; French, R., Short-term changes in the beltzone structure of Saturn's Southern Hemisphere, Astronomy & Astrophysics, vol. 460, 641-645, 2006.

Sachs, A., Babylonian Observational Astronomy, Philosophical Transactions of the Royal Society of London (Royal Society of London), 276 (1257), 43-50 [45 & 48-9], 1974.

Sánchez-Lavega, A., Pérez-Hoyos, S.; Rojas, J. F.; Hueso, R.; French, R. G., A strong decrease in Saturn's equatorial jet at cloud level, Nature, 423, 623-625, 2003.

Sánchez-Lavega, A, Hueso, R., Pérez-Hoyos, S., The three-dimensional structure of Saturn's equatorial jet at cloud level, Icarus 187, 510-519, 2007.

Stevenson, D. J., Planetary Science: A new spin on Saturn, Nature 441, 34-35, 2006

Widemann, T. et al., New wind measurements in Venus lower mesosphere from visible spectroscopy, Planetary and Space Science, volume 55, p. 1741-1756, 2007.

Widemann et al., Venus Doppler winds at cloud tops observed with ESPaDOnS at CFHT, Planetary and Space Science, Volume 56, p. 1320-1334, 2008.

Young A., Is the Four-Day "Rotation" of Venus Illusory?, Icarus, volume 24, p. 1-10, 1975.

- http://www.nasa.gov/cassini
- http://www.jpl.nasa.gov/news/news.php?release=2011-203 (Retrieved 31 May, 2016)
- "Scientists Find That Saturn's Rotation Period is a Puzzle". NASA. 28 June 2004. Archived from the original on 21 August 2011 (Retrieved 23 June 2016)
- http://www.nasa.gov/mission_pages/cassini/media/cassini-062804.html (Retrieved 9 June, 2016)
- "Saturn south pole storm" - http://www.nasa.gov/images/content/162349main_pia08332-516.jpg (Retrieved 28 May, 2016)
- https://www.newscientist.com/article/dn9100-saturns-rotation-puts-astronomers-in-a-spin/ (Retrieved 9 June, 2016)
- http://cseligman.com/text/planets/saturnrot.htm (Retrieved 9 June, 2016)
- https://lightsinthedark.com/2013/12/04/cassinis-best-look-yet-at-saturns-crazy-hexagon/ (Retrieved 25 May, 2016)
- "Saturn wind speed" - http://www.gettyimages.pt/fotos/saturn-wind-speed (Retrieved 23 May, 2016)
- http://hendrix2.uoregon.edu/~imamura/121/lecture-13/jupiter_atmosphere.html (Retrieved 25 May, 2016)
- "Warm Polar Vortex on Saturn". Merrillville Community Planetarium. 2007. (Retrieved 28 May, 2016)
- "The Pioneer 10 & 11 Spacecraft". Mission Descriptions. (Retrieved 29 May, 2016)

- https://en.m.wkipedia.org - Pioneer 11 image of Saturn (Retrieved 29 May, 2016)
- "Missions to Saturn". The Planetary Society. 2007
- "Massive storm at Saturn's north pole". 3 News NZ. 30 April 2013
- Patrick Irwin (Oxford University), private communication

Appendix A - Data Results

4.2.1 First Day of Observations (20-04-2004)

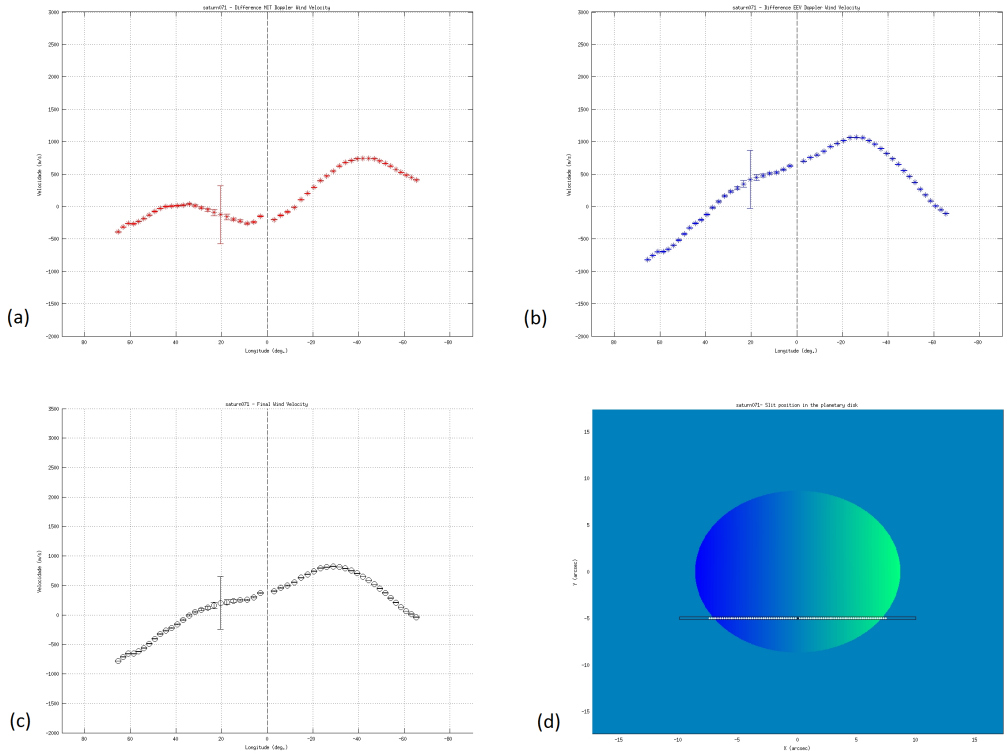

Figure 4.2: (a) MIT detector Doppler velocities along the slit position 4 ($\overline{v} = 116ms^{-1}$; (b) EEV detector Doppler velocities along the same slit position ($\overline{v} = 222ms^{-1}$); (c) Weighted average of the MIT and EEV Doppler velocities along the same slit position ($\overline{v} = 180ms^{-1}$); (d) Scheme of the position of the slit on the planetary disk.

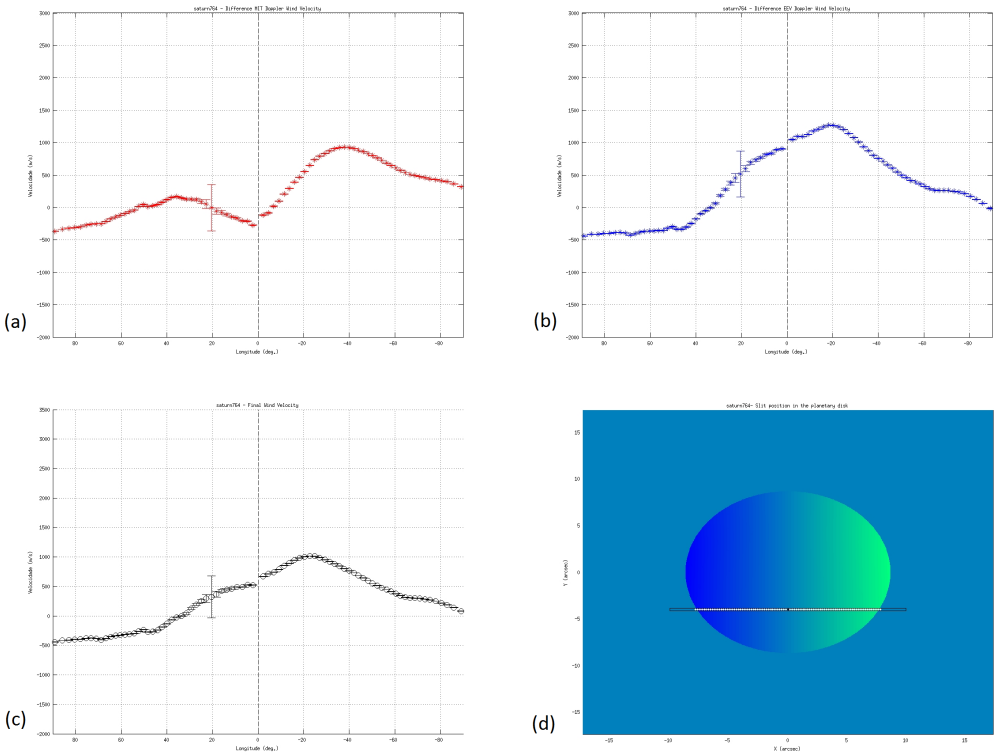

Figure 4.3: Same as above but for slit position 5. $\overline{v}_{MIT} = 231ms^{-1}$; $\overline{v}_{EEV} = 322ms^{-1}$; $\overline{v}_{med} = 270ms^{-1}$

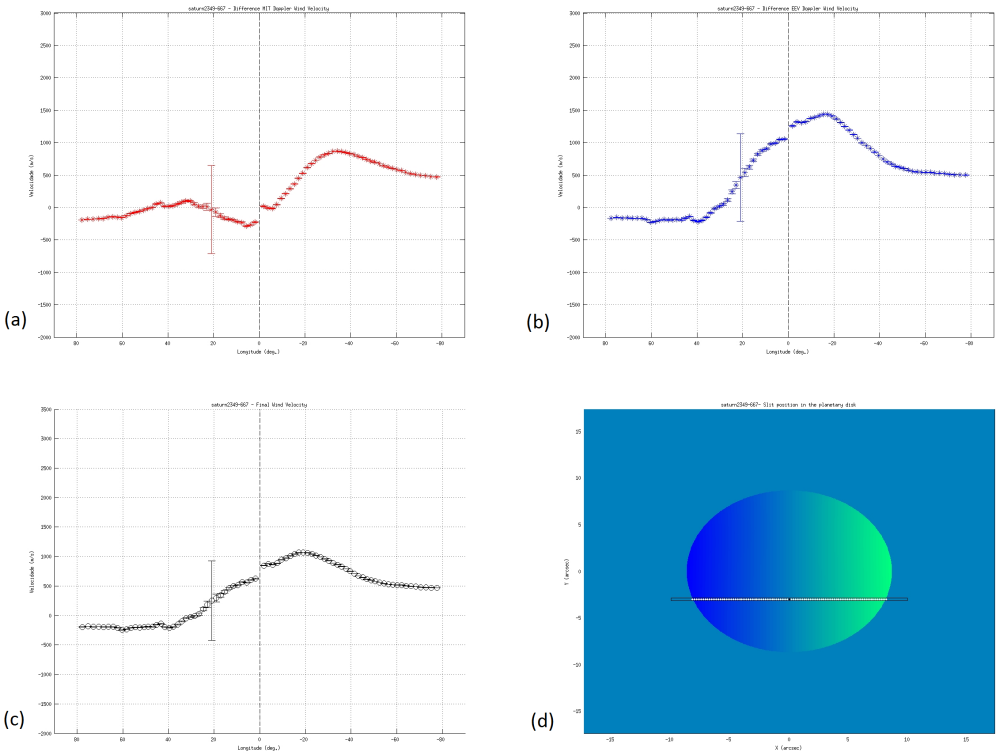

Figure 4.4: Same as above but for slit position 6.$\overline{v}_{MIT} = 226ms^{-1}$; $\overline{v}_{EEV} = 496ms^{-1}$; $\overline{v}_{med} = 389ms^{-1}$

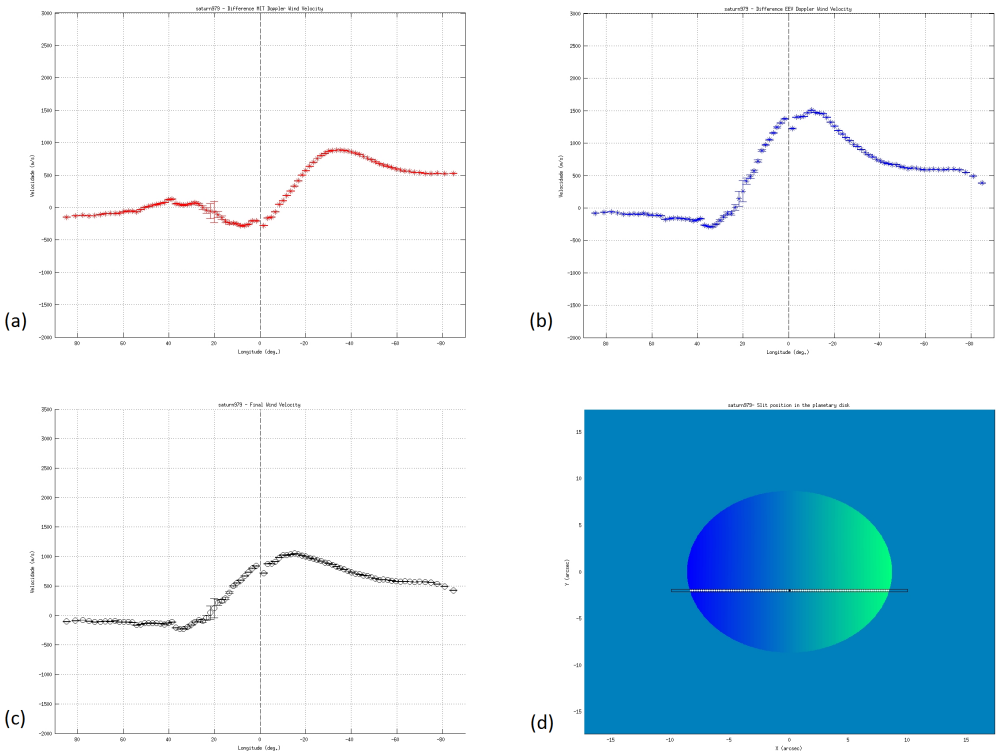

Figure 4.5: Same as above but for slit position 7. $\overline{v}_{MIT} = 239ms^{-1}$; $\overline{v}_{EEV} = 513ms^{-1}$; $\overline{v}_{med} = 404ms^{-1}$

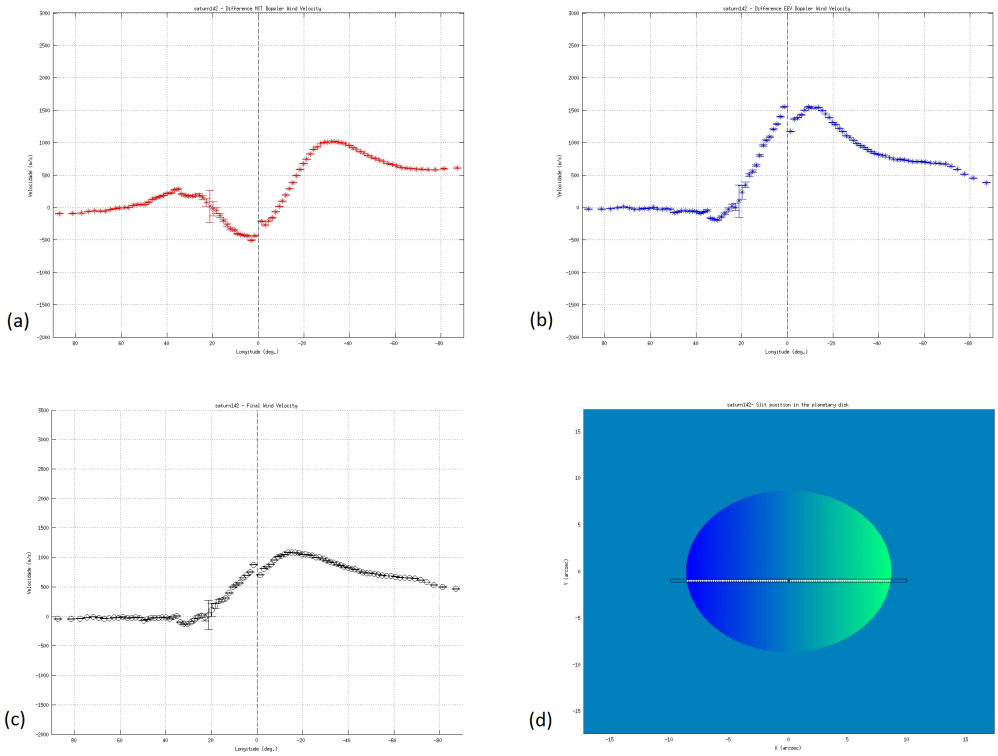

Figure 4.6: Same as above but for slit position 8. $\overline{v}_{MIT} = 294ms^{-1}$; $\overline{v}_{EEV} = 597ms^{-1}$; $\overline{v}_{med} = 467ms^{-1}$

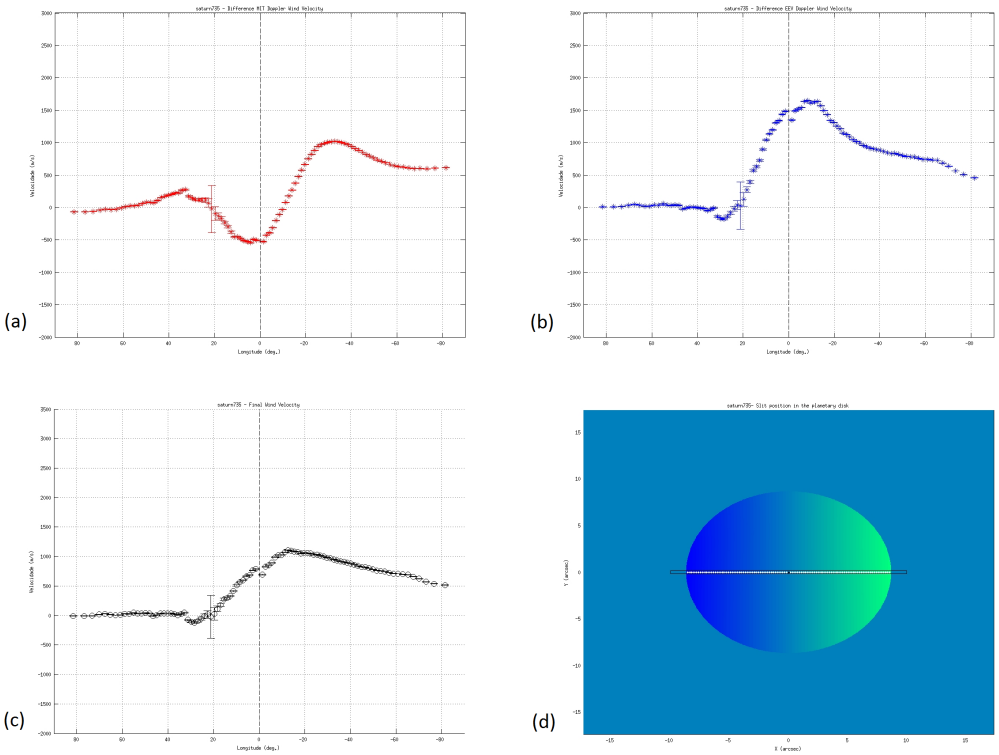

Figure 4.7: Same as above but for slit position 9. $\overline{v}_{MIT} = 264ms^{-1}$; $\overline{v}_{EEV} = 657ms^{-1}$; $\overline{v}_{med} = 504ms^{-1}$

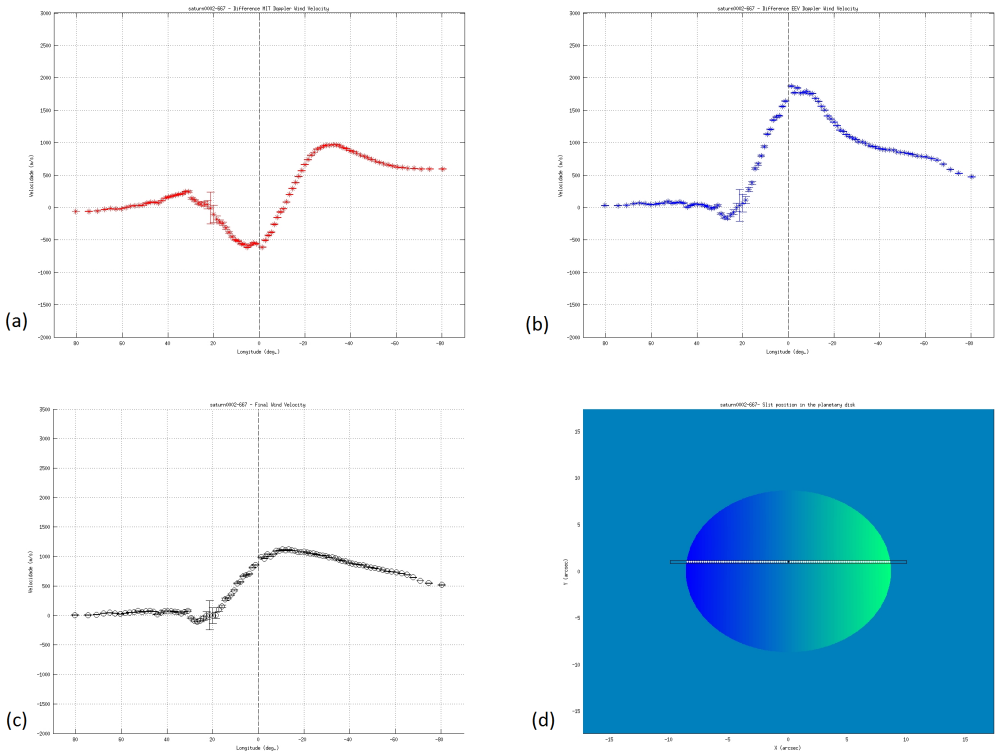

Figure 4.8: Same as above but for slit position 10. $\overline{v}_{MIT} = 227ms^{-1}$; $\overline{v}_{EEV} = 719ms^{-1}$; $\overline{v}_{med} = 539ms^{-1}$

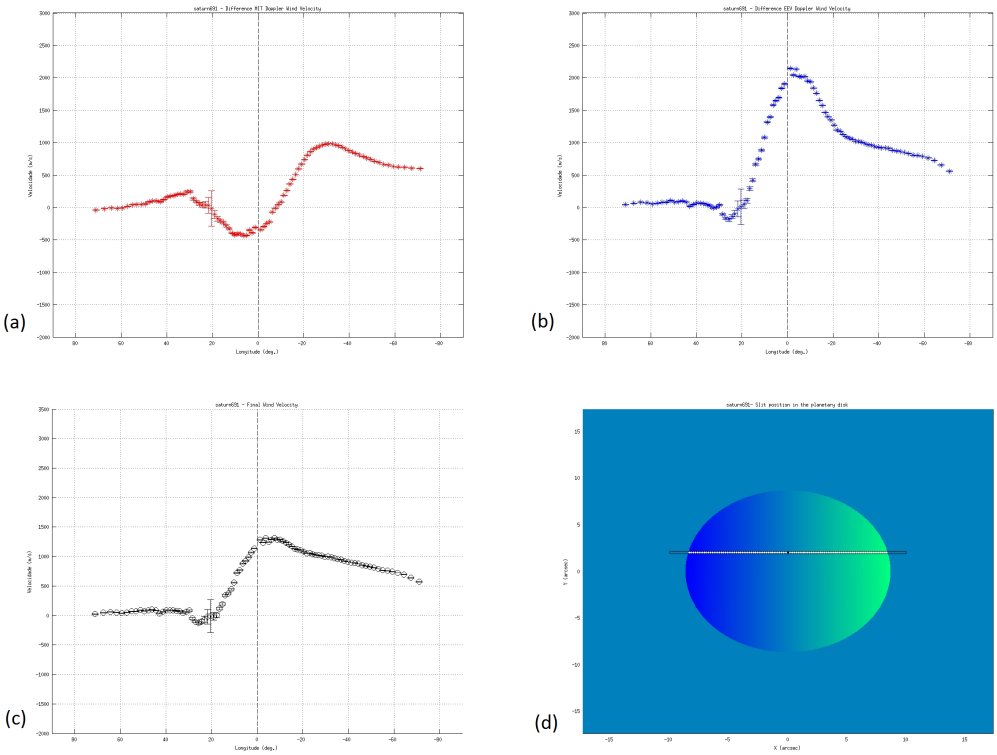

Figure 4.9: Same as above but for slit position 11. $\overline{v}_{MIT} = 264ms^{-1}$; $\overline{v}_{EEV} = 787ms^{-1}$; $\overline{v}_{med} = 608ms^{-1}$

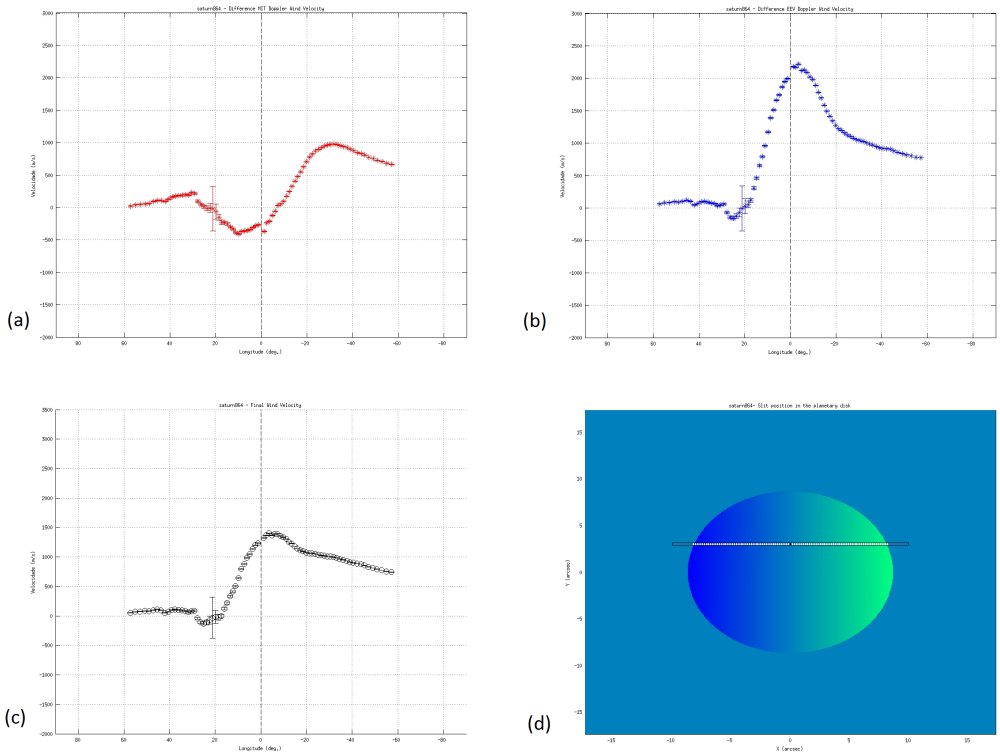

Figure 4.10: Same as above but for slit position 12. $\overline{v}_{MIT} = 247ms^{-1}$; $\overline{v}_{EEV} = 826ms^{-1}$; $\overline{v}_{med} = 664ms^{-1}$

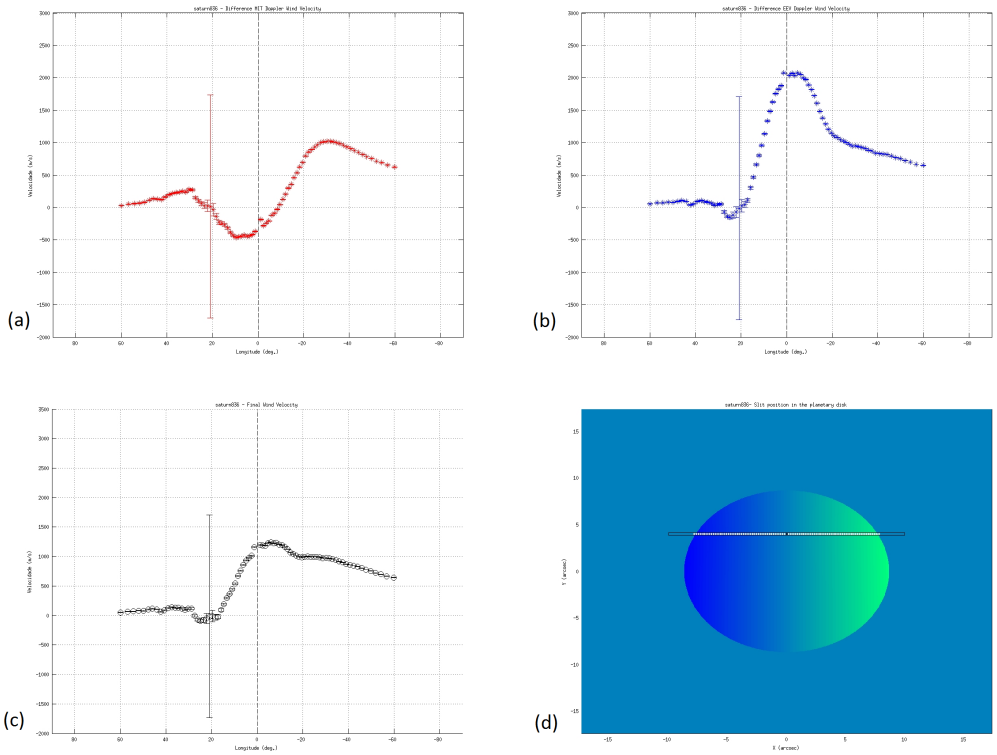

Figure 4.11: Same as above but for slit position 13. $\overline{v}_{MIT} = 253ms^{-1}$; $\overline{v}_{EEV} = 797ms^{-1}$; $\overline{v}_{med} = 614ms^{-1}$

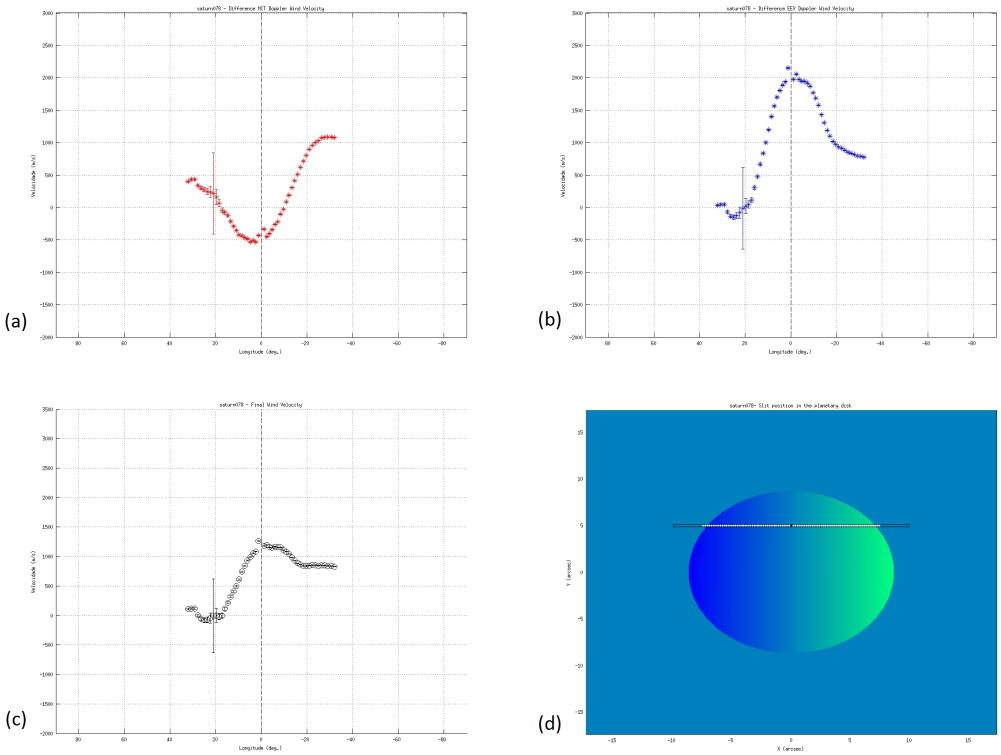

Figure 4.12: Same as above but for slit position 14. $\overline{v}_{MIT} = 137ms^{-1}$; $\overline{v}_{EEV} = 758ms^{-1}$; $\overline{v}_{med} = 670ms^{-1}$

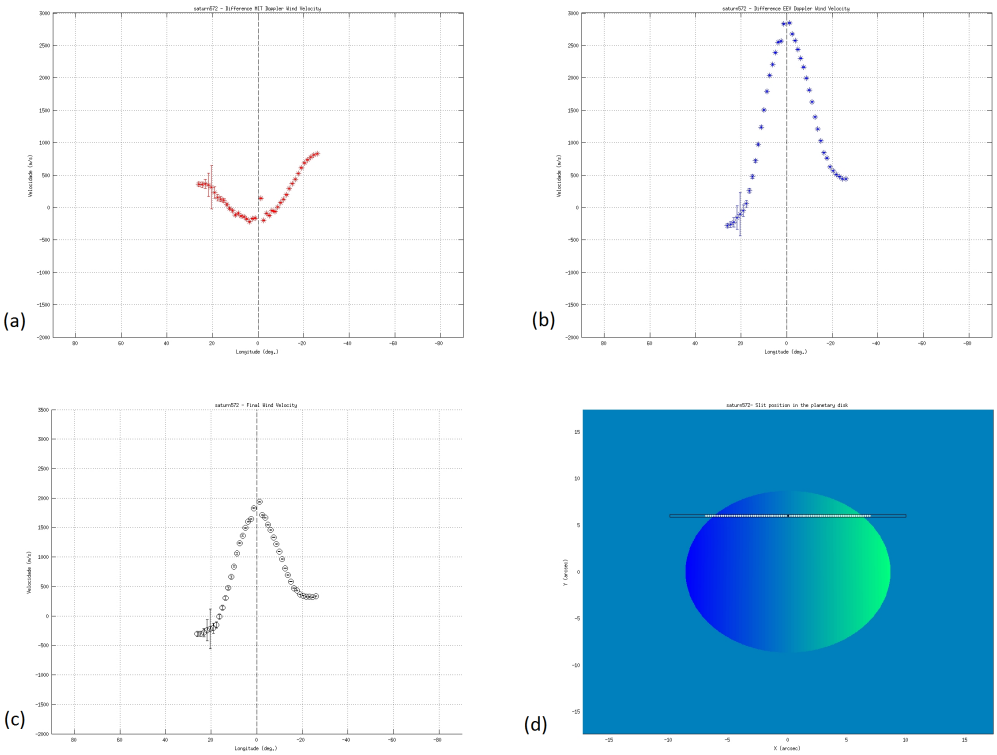

Figure 4.13: Same as above but for slit position 15. $\overline{v}_{MIT} = 125ms^{-1}$; $\overline{v}_{EEV} = 850ms^{-1}$; $\overline{v}_{med} = 721ms^{-1}$

4.2.2 Second Day of Observations (21-04-2004)

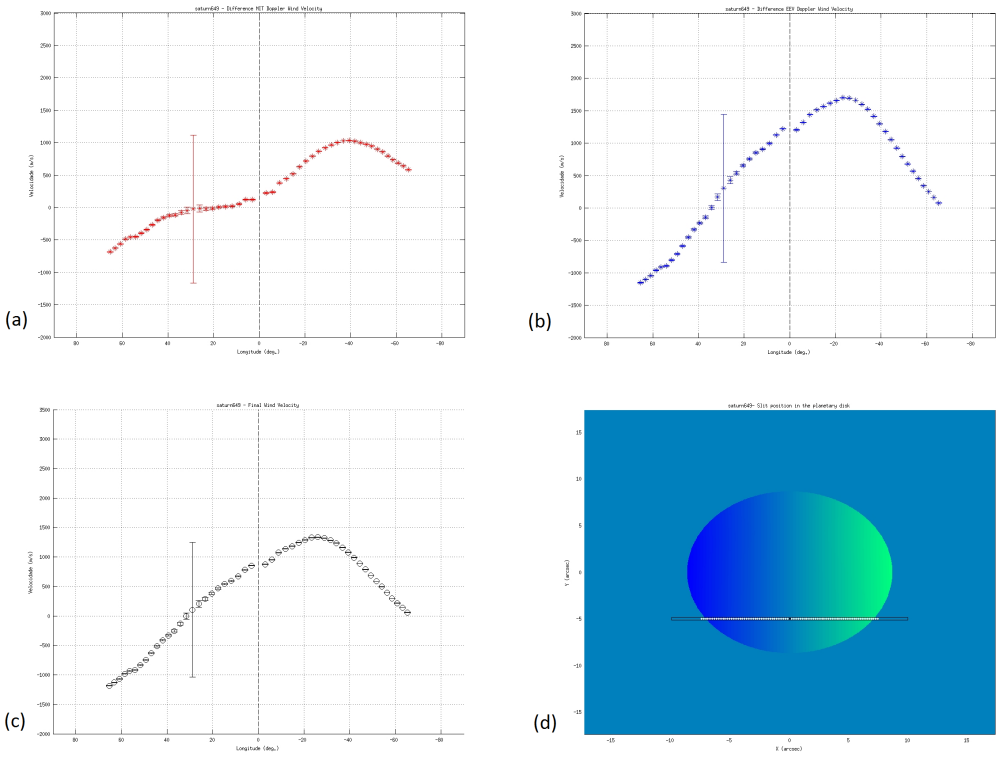

Figure 4.14: Same as above but for the second day of observations and slit position 4. $\overline{v}_{MIT} = 215ms^{-1}$; $\overline{v}_{EEV} = 399ms^{-1}$; $\overline{v}_{med} = 337ms^{-1}$

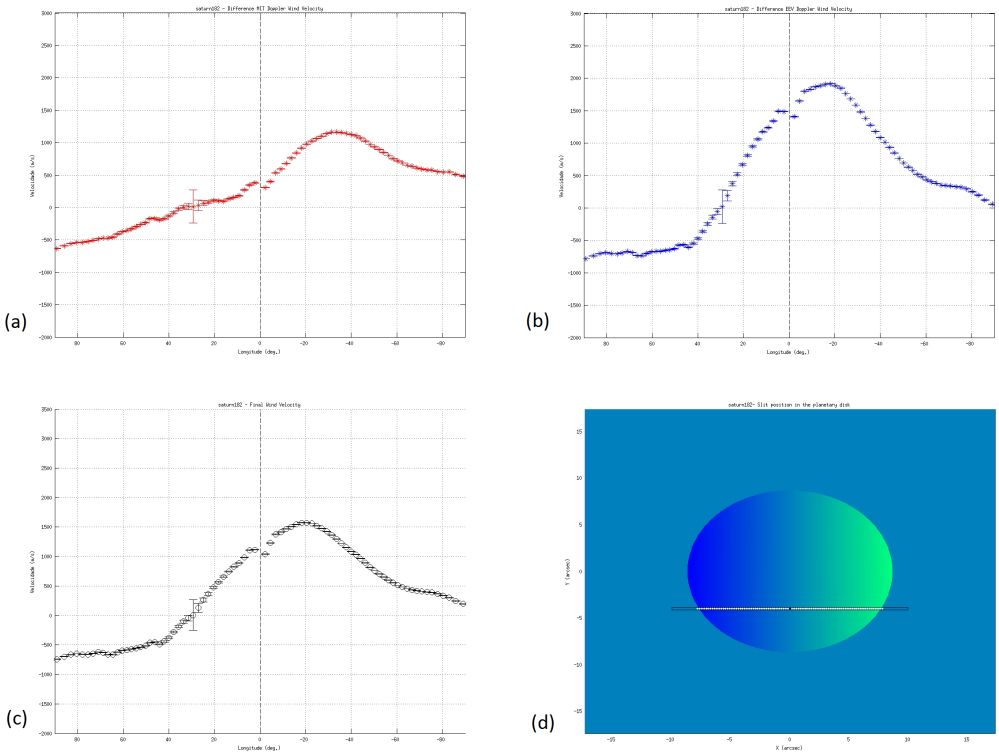

Figure 4.15: Same as above for slit position 5. $\overline{v}_{MIT} = 304ms^{-1}$; $\overline{v}_{EEV} = 388ms^{-1}$; $\overline{v}_{med} = 386ms^{-1}$

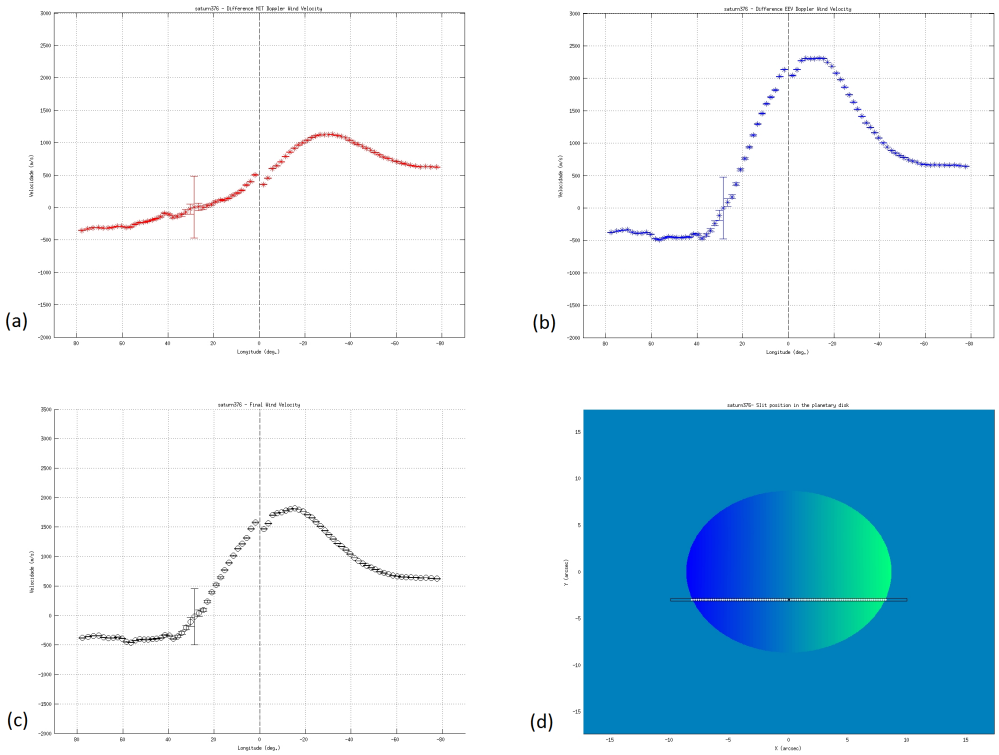

Figure 4.16: Same as above for slit position 6. $\overline{v}_{MIT} = 362ms^{-1}$; $\overline{v}_{EEV} = 702ms^{-1}$; $\overline{v}_{med} = 605ms^{-1}$

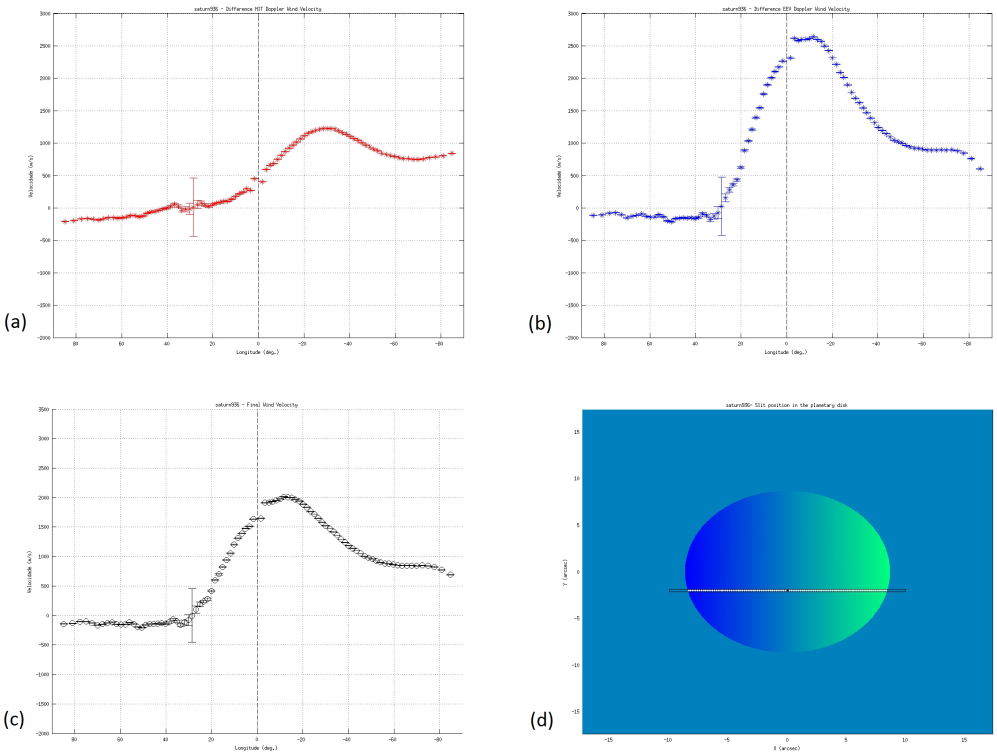

Figure 4.17: Same as above but for slit position 7. $\overline{v}_{MIT} = 458ms^{-1}$; $\overline{v}_{EEV} = 953ms^{-1}$; $\overline{v}_{med} = 780ms^{-1}$

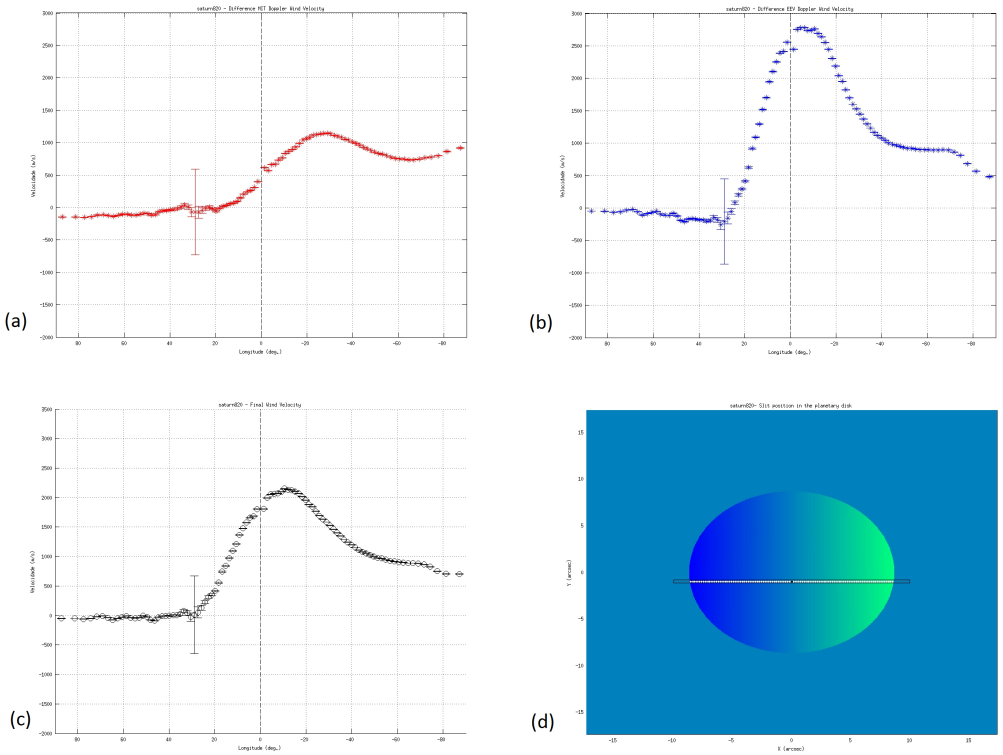

Figure 4.18: Same as above but for slit position 8. $\overline{v}_{MIT} = 441ms^{-1}$; $\overline{v}_{EEV} = 951ms^{-1}$; $\overline{v}_{med} = 871ms^{-1}$

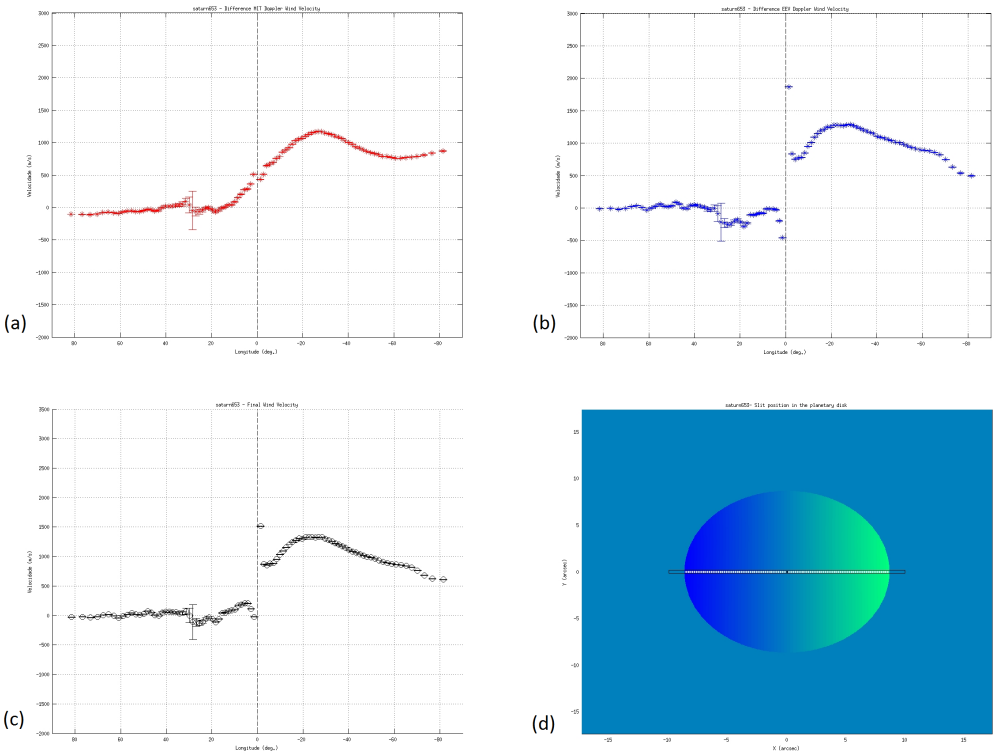

Figure 4.19: Same as above but for slit position 9. $\overline{v}_{MIT} = 461ms^{-1}$; $\overline{v}_{EEV} = 627ms^{-1}$; $\overline{v}_{med} = 542ms^{-1}$

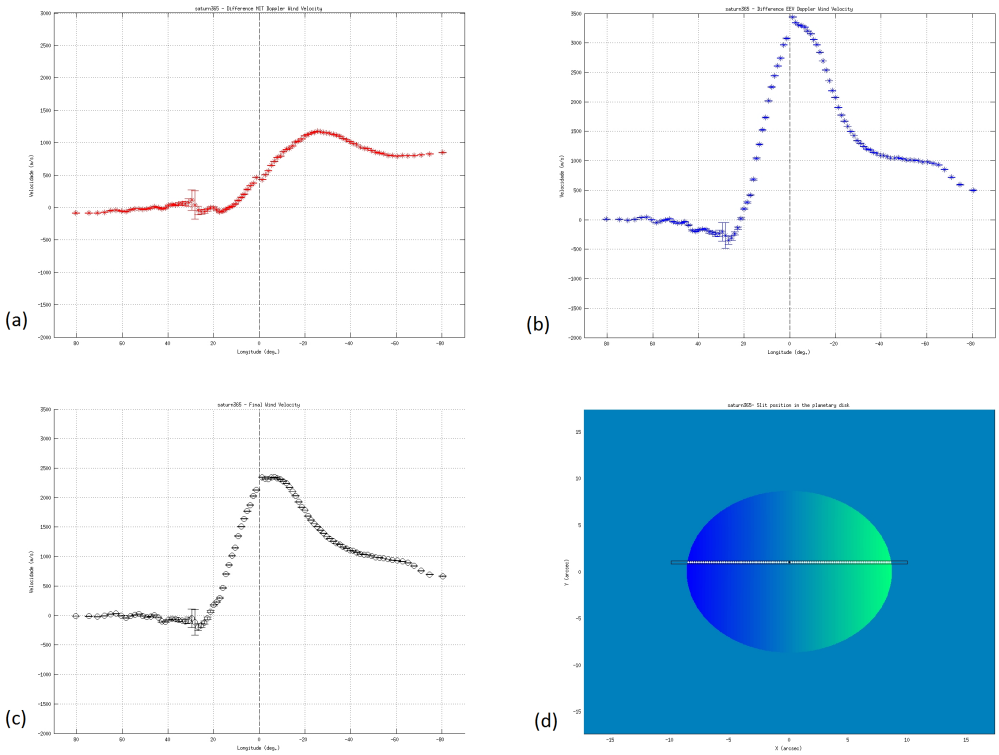

Figure 4.20: Same as above but for slit position 10. $\overline{v}_{MIT} = 477ms^{-1}$; $\overline{v}_{EEV} = 1084ms^{-1}$; $\overline{v}_{med} = 896ms^{-1}$

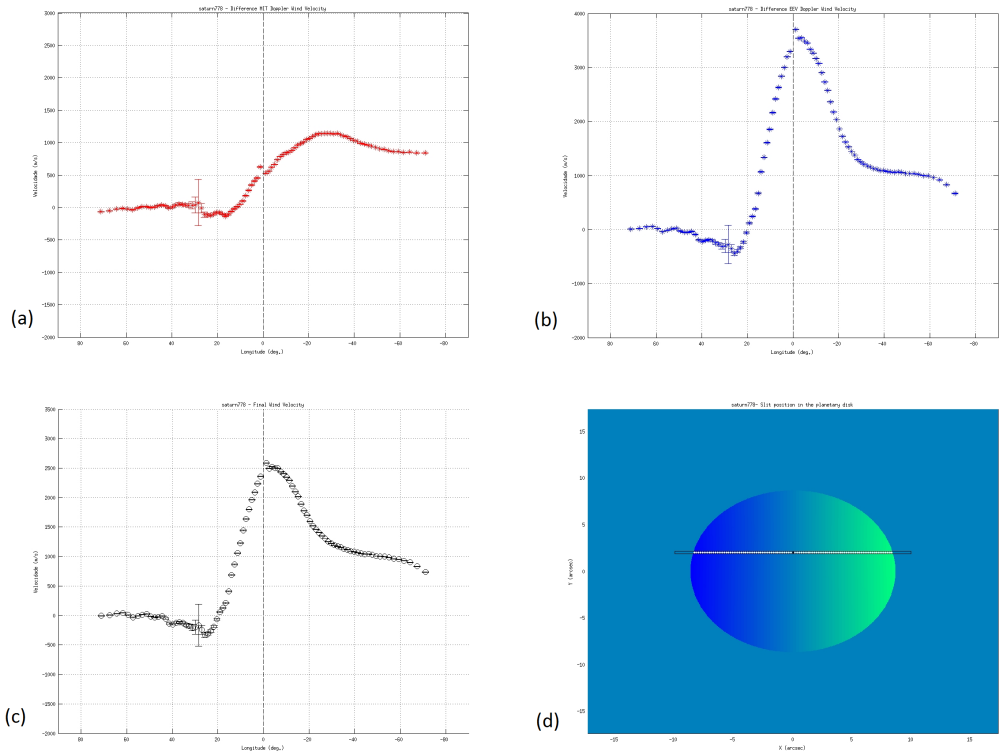

Figure 4.21: Same as above but for slit position 11. $\overline{v}_{MIT} = 486ms^{-1}$; $\overline{v}_{EEV} = 1129ms^{-1}$; $\overline{v}_{med} = 917ms^{-1}$

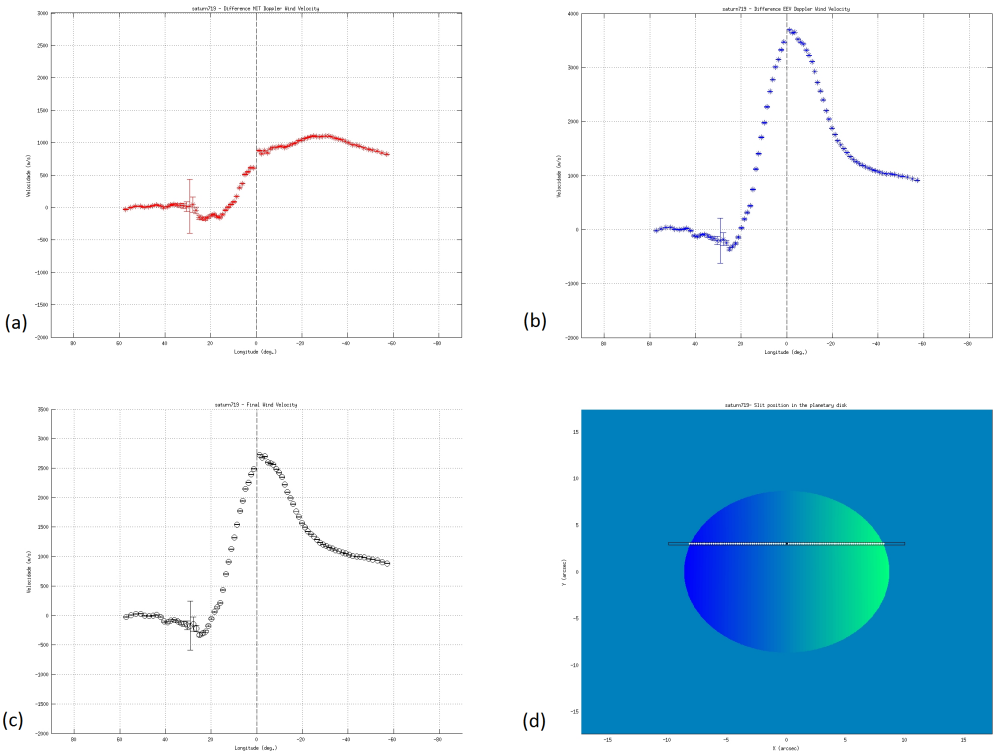

Figure 4.22: Same as above but for slit position 12. $\overline{v}_{MIT} = 488ms^{-1}$; $\overline{v}_{EEV} = 1203ms^{-1}$; $\overline{v}_{med} = 1000ms^{-1}$

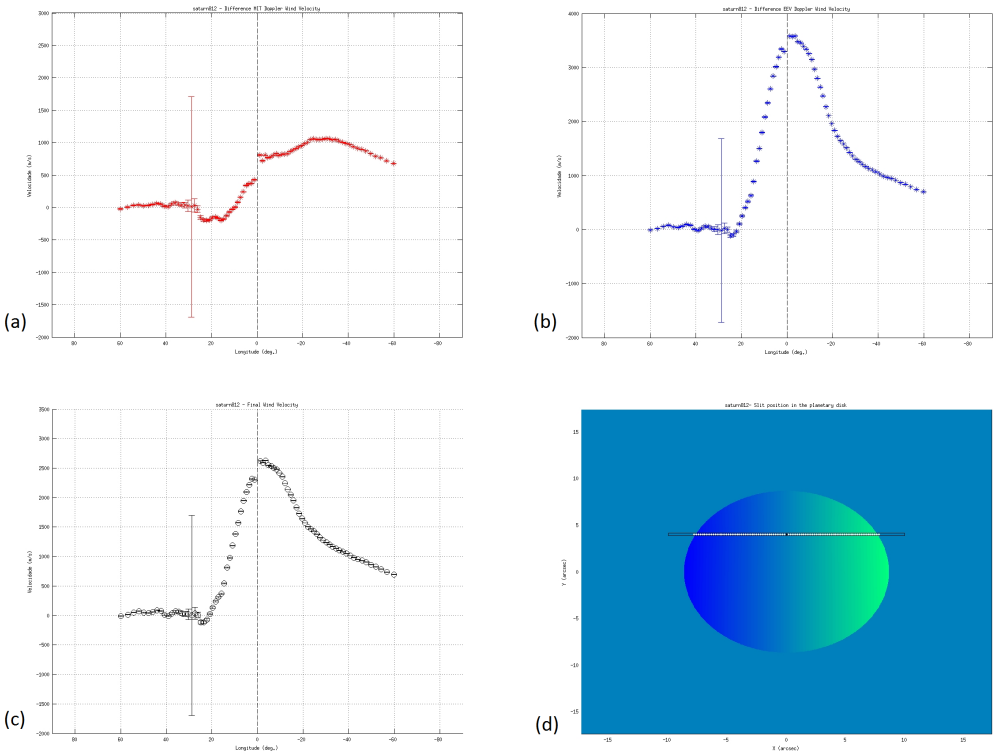

Figure 4.23: Same as above but for slit position 13. $\overline{v}_{MIT} = 446ms^{-1}$; $\overline{v}_{EEV} = 1284ms^{-1}$; $\overline{v}_{med} = 1044ms^{-1}$

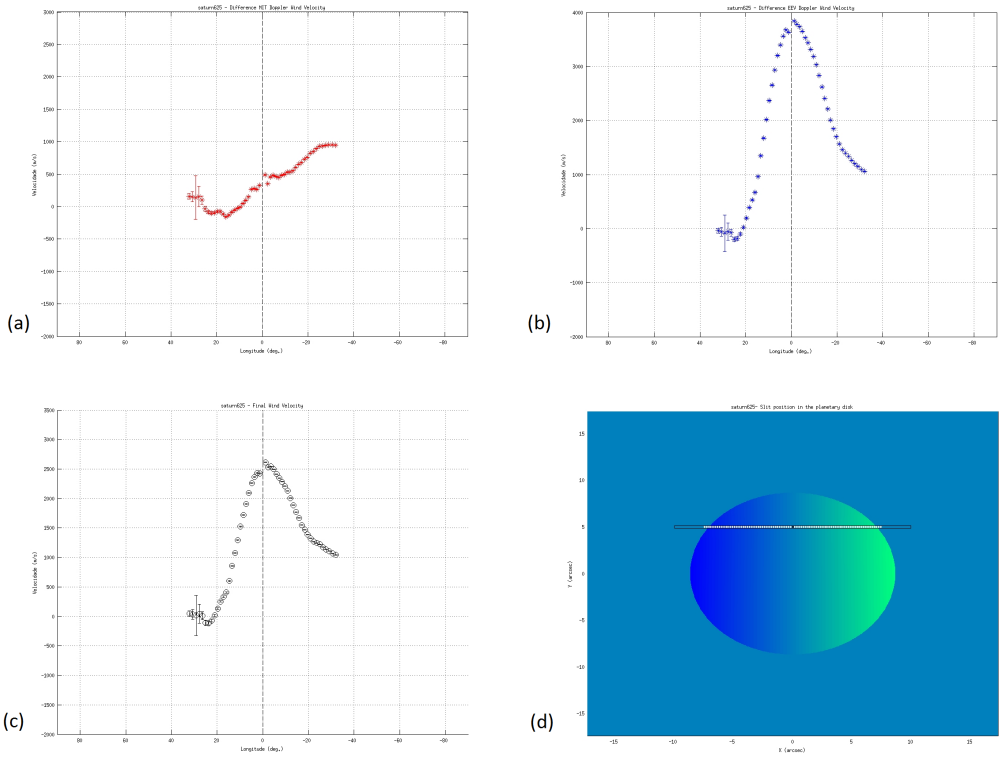

Figure 4.24: Same as above but for slit position 14. $\overline{v}_{MIT} = 273ms^{-1}$; $\overline{v}_{EEV} = 1381ms^{-1}$; $\overline{v}_{med} = 1310ms^{-1}$

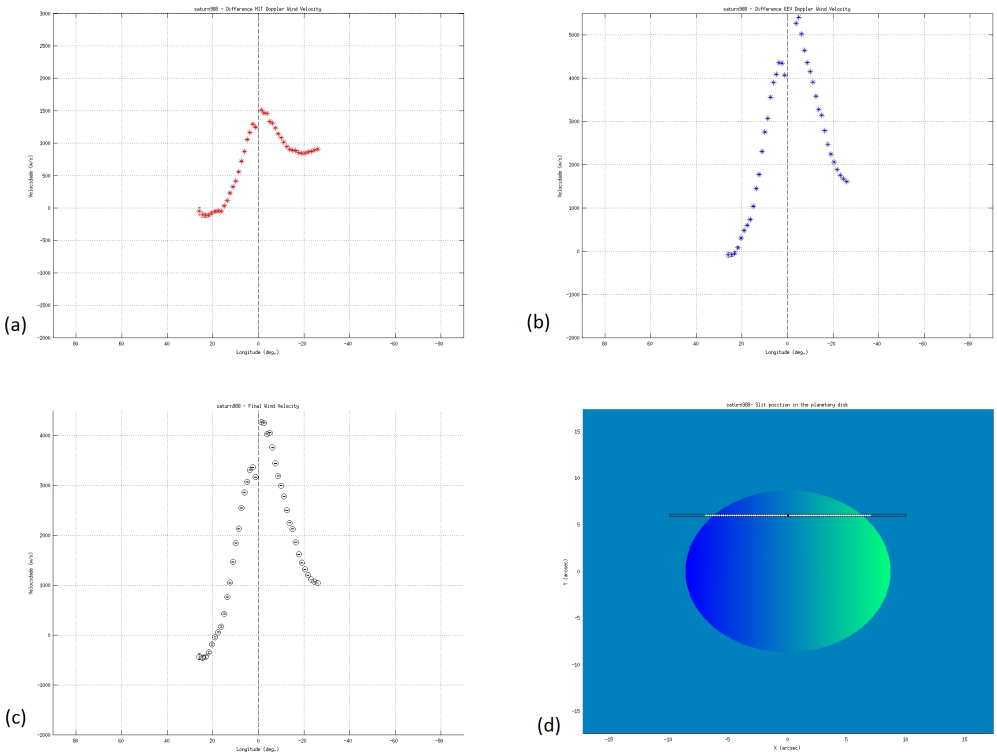

Figure 4.25: Same as above but for slit position 15. $\overline{v}_{MIT} = 495ms^{-1}$; $\overline{v}_{EEV} = 1882ms^{-1}$; $\overline{v}_{med} = 1864ms^{-1}$

4.2.3 Third Day of Observations (29-04-2004)

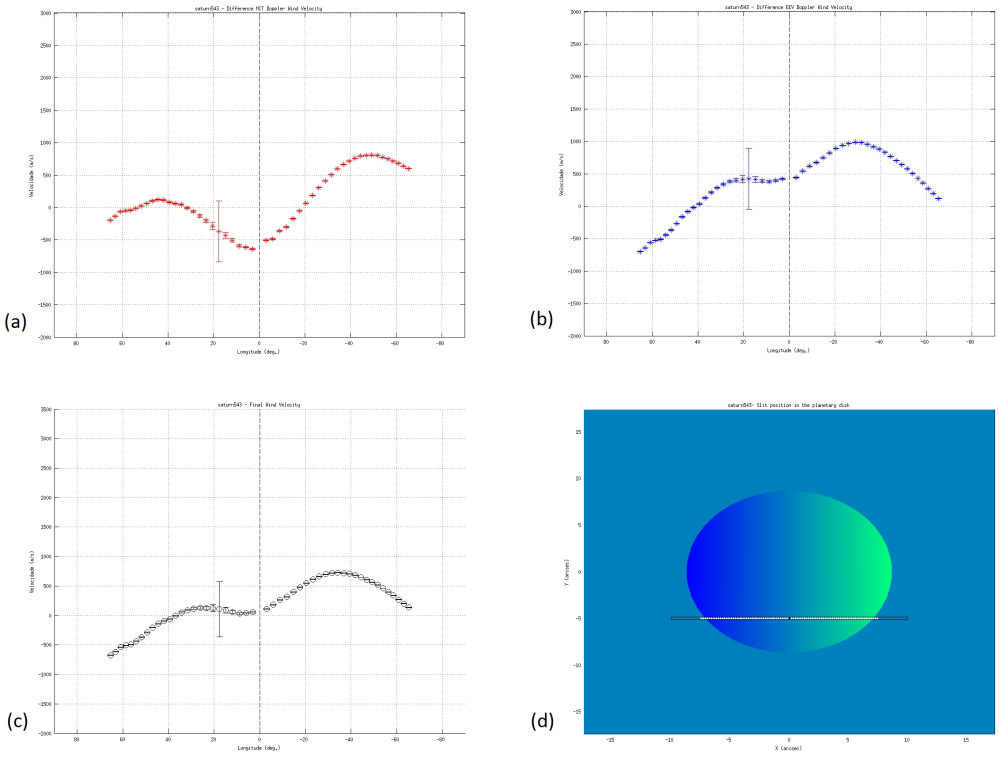

Figure 4.26: Same as above but for the third day of observations and for slit position 4. $\overline{v}_{MIT} = 91ms^{-1}$; $\overline{v}_{EEV} = 259ms^{-1}$; $\overline{v}_{med} = 171ms^{-1}$

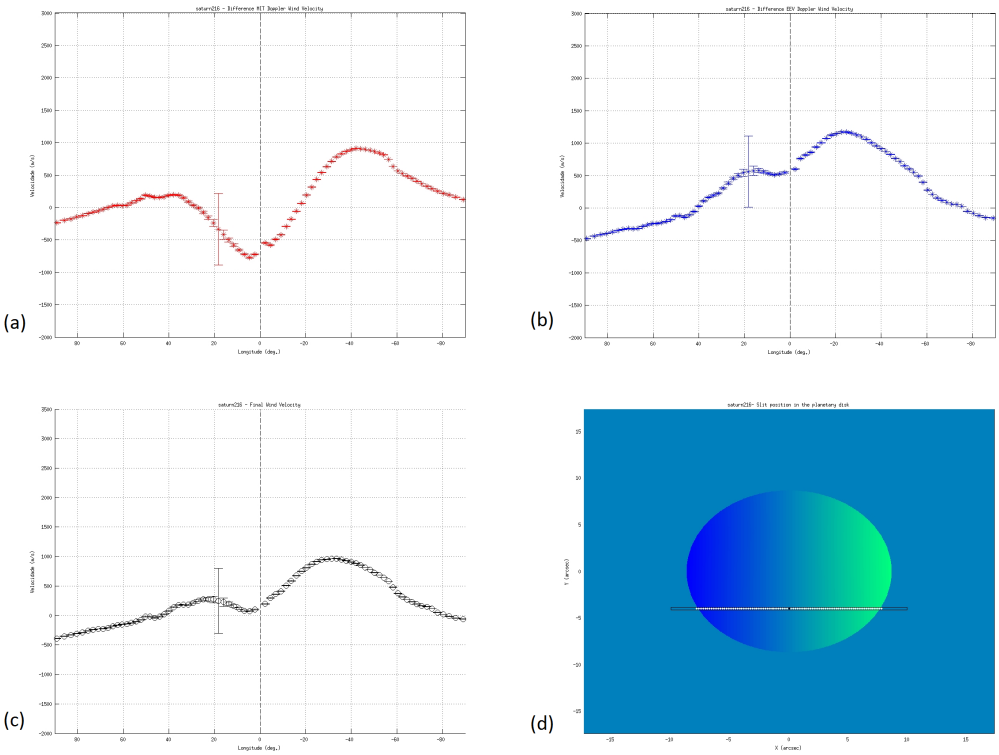

Figure 4.27: Same as above but for slit position 5. $\overline{v}_{MIT} = 137ms^{-1}$; $\overline{v}_{EEV} = 309ms^{-1}$; $\overline{v}_{med} = 257ms^{-1}$

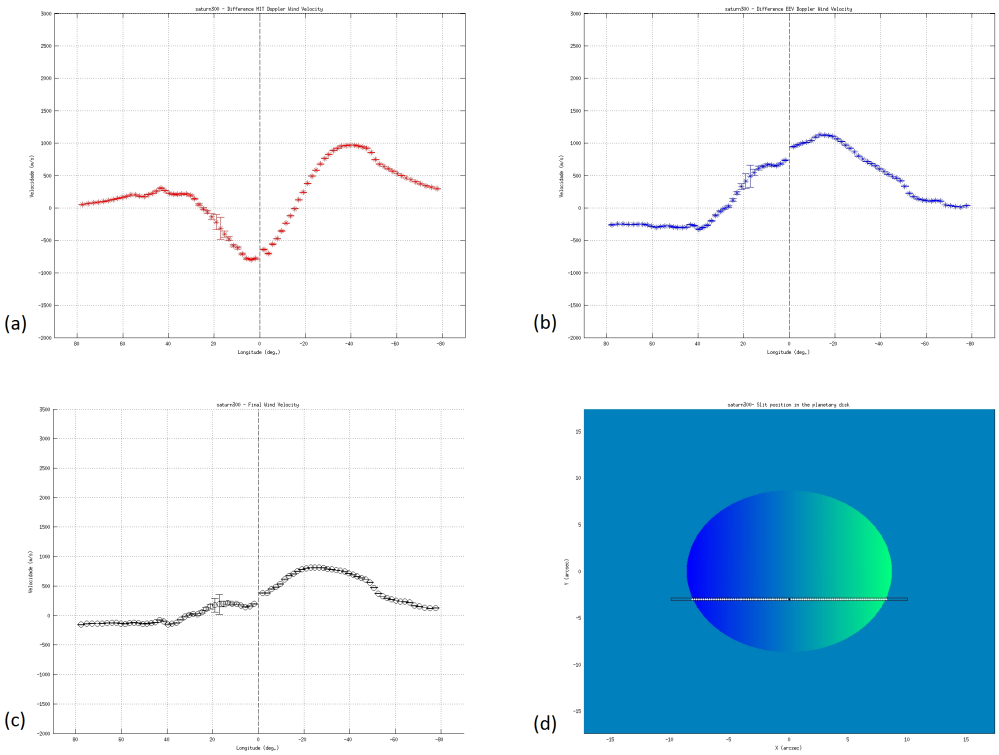

Figure 4.28: Same as above but for slit position 6. $\overline{v}_{MIT} = 188ms^{-1}$; $\overline{v}_{EEV} = 282ms^{-1}$; $\overline{v}_{med} = 252ms^{-1}$

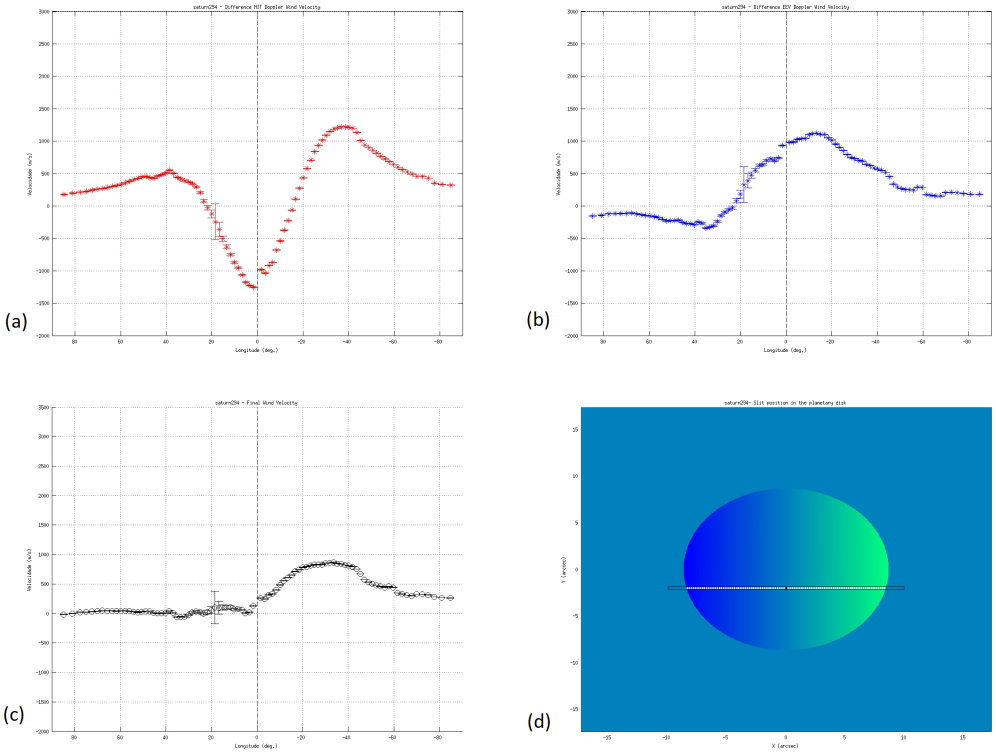

Figure 4.29: Same as above but for slit position 7. $\overline{v}_{MIT} = 260ms^{-1}$; $\overline{v}_{EEV} = 309ms^{-1}$; $\overline{v}_{med} = 297ms^{-1}$

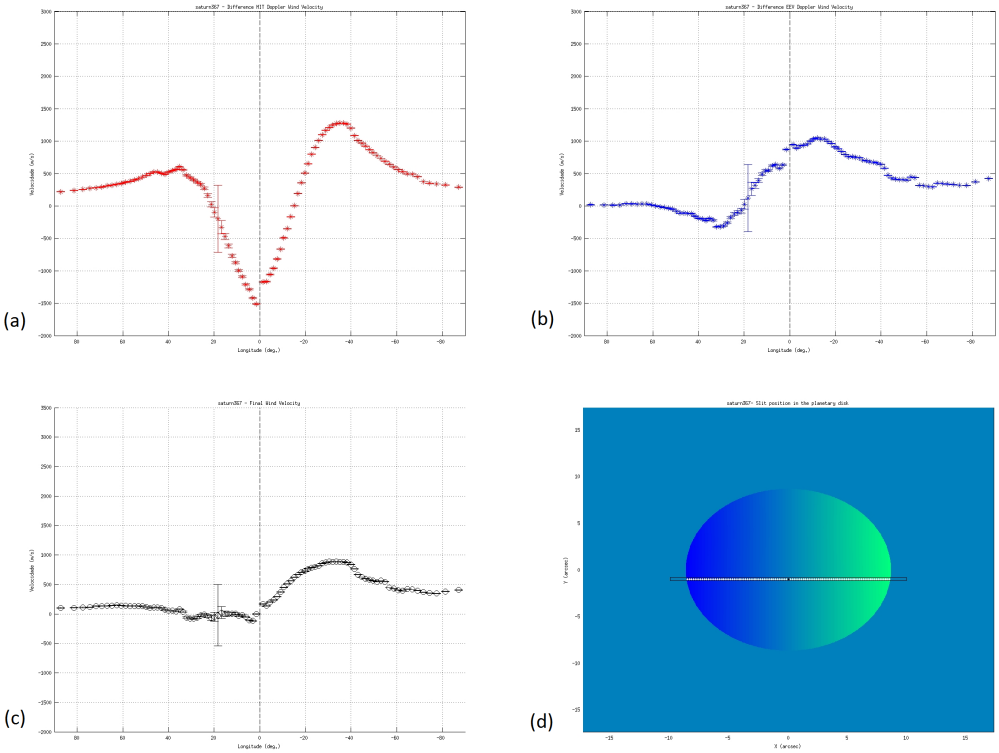

Figure 4.30: Same as above but for slit position 8. $\overline{v}_{MIT} = 258ms^{-1}$; $\overline{v}_{EEV} = 352ms^{-1}$; $\overline{v}_{med} = 308ms^{-1}$

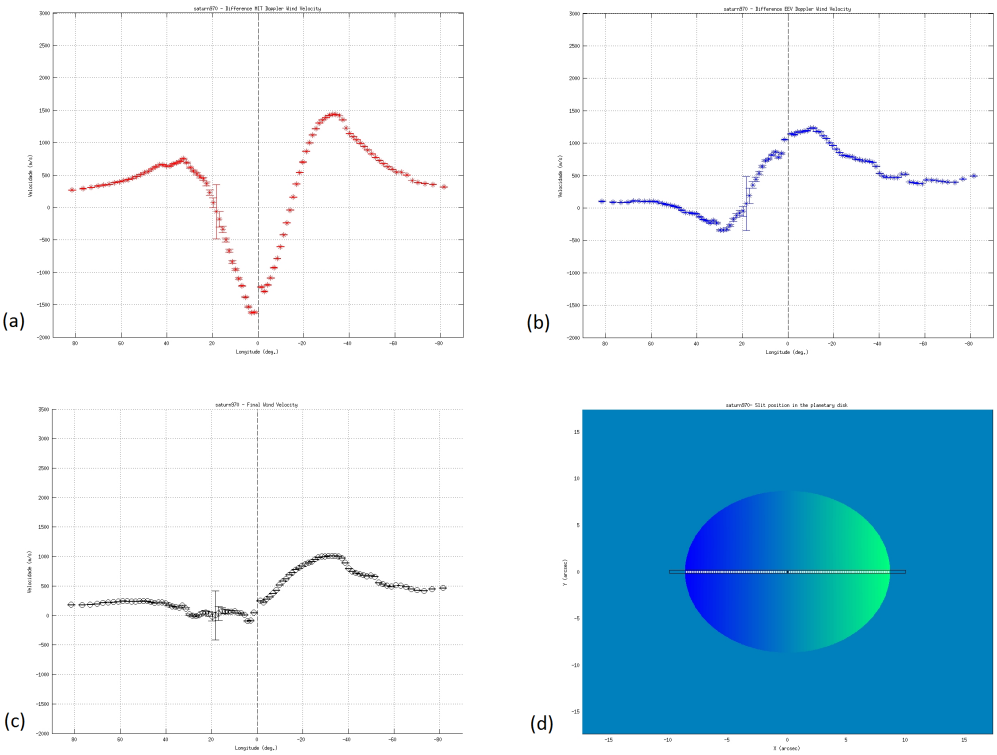

Figure 4.31: Same as above but for slit position 9. $\overline{v}_{MIT} = 308ms^{-1}$; $\overline{v}_{EEV} = 435ms^{-1}$; $\overline{v}_{med} = 396ms^{-1}$

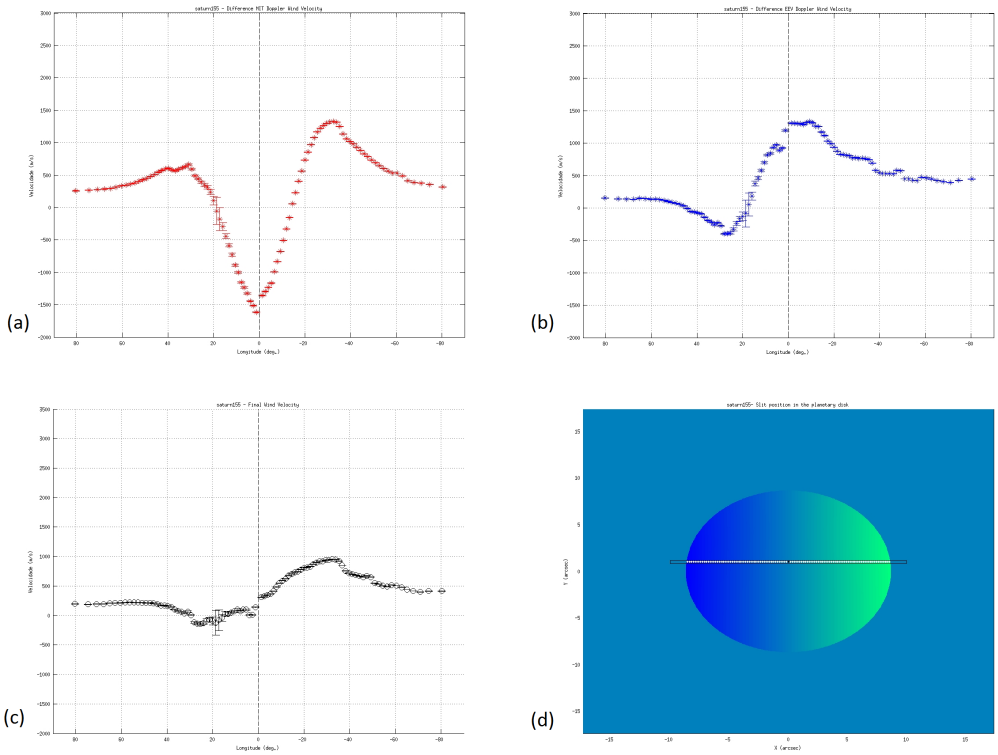

Figure 4.32: Same as above but for slit position 10. $\overline{v}_{MIT} = 240ms^{-1}$; $\overline{v}_{EEV} = 470ms^{-1}$; $\overline{v}_{med} = 366ms^{-1}$

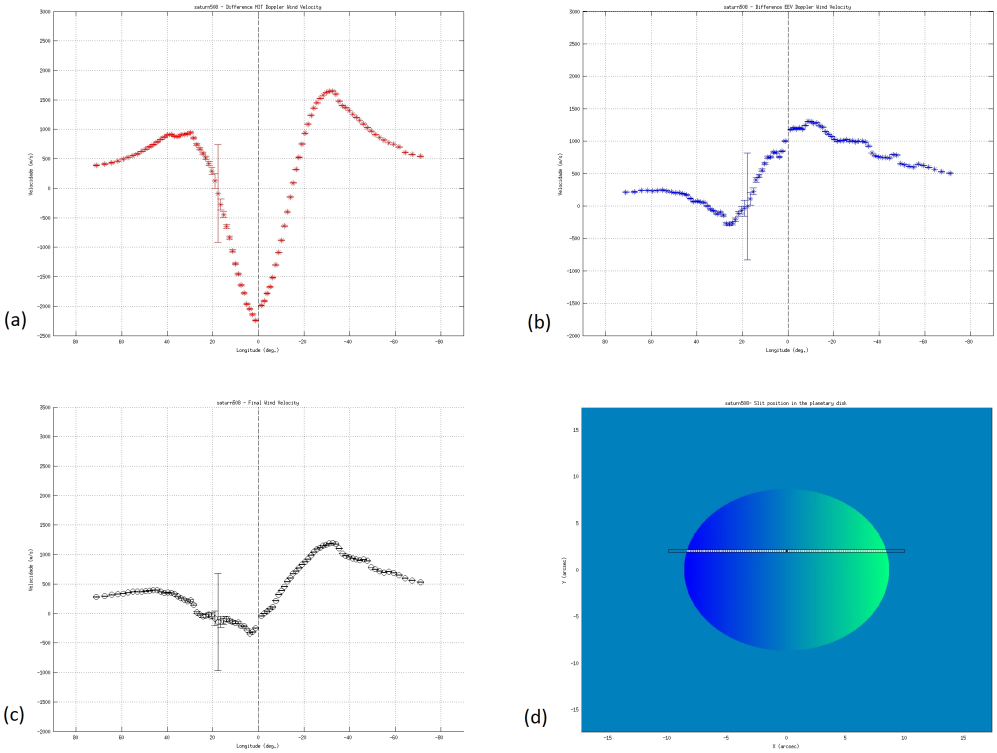

Figure 4.33: Same as above but for slit position 11. $\overline{v}_{MIT} = 280ms^{-1}$; $\overline{v}_{EEV} = 570ms^{-1}$; $\overline{v}_{med} = 419ms^{-1}$

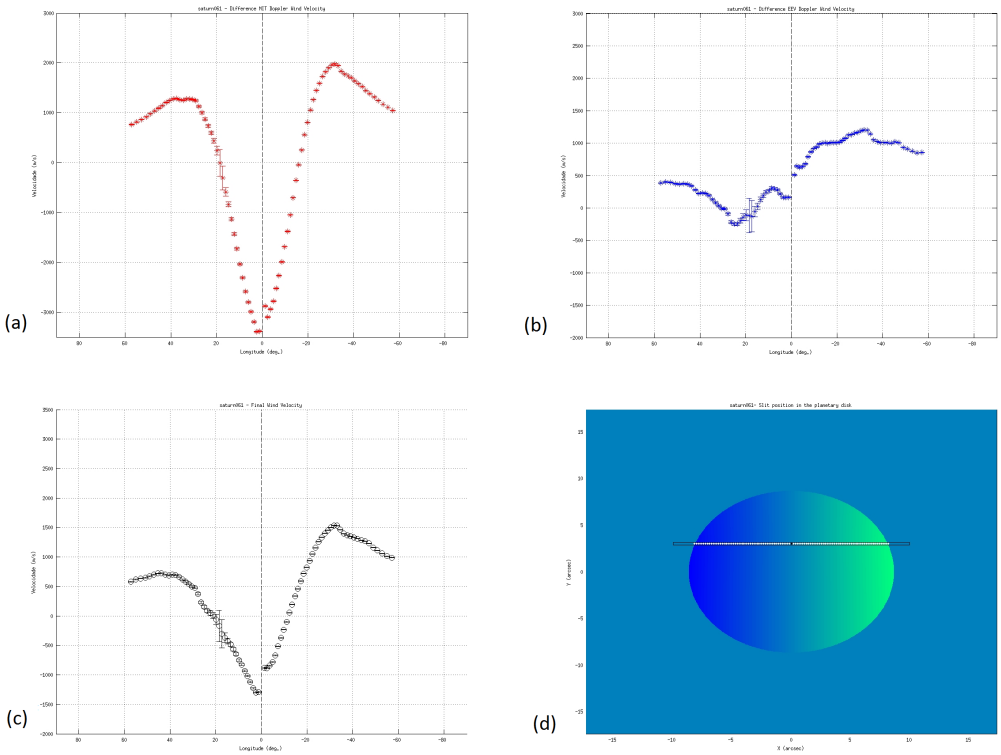

Figure 4.34: Same as above but for slit position 12. $\overline{v}_{MIT} = 137ms^{-1}$; $\overline{v}_{EEV} = 516ms^{-1}$; $\overline{v}_{med} = 366ms^{-1}$

Appendix B - MATLAB scripts

The archive given by Dr. Pedro Machado, is based on a MATLAB software package called "WIND", developed by Thomas Civeit and dedicated to spectroscopic measurements of planetary winds. This package consisted in a series of main folders which we organized according to the scheme displayed in figure 4.35.

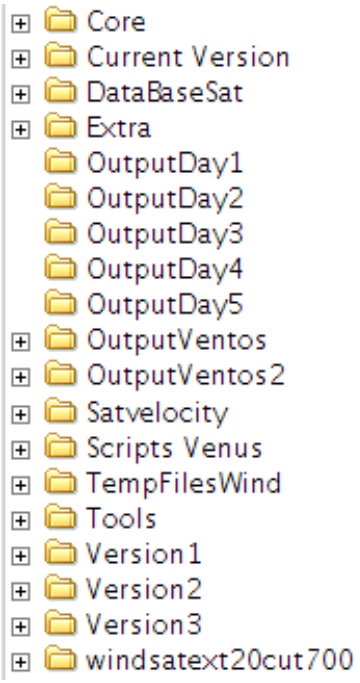

Figure 4.35: Organization structure of the folders containing the MATLAB scripts used on this work and the output files.

The contents inside each folder are the following:

- **Core** - Each function performs a single task required during the data reduction. Some of them use external functions which can be found in the "Tools" folder.

- ***wind_check_sat.m*** - Check the existence and readability of the files, compute the master median frames of the *bias* and *flat field* frames and copy the files by using the *eso2fits* program.
- ***wind_import.m*** - Imports, formats and saves data in the working directory as ".mat" files. The files will be loaded after from the back-up and not from the original ".fits" file. This way, they can be easily opened and used.
- ***wind_map.m*** - Determine the *echelle* order locations. The procedure first performs an image segmentation in order to detect the peaks of intensity, then it fits the order traces with polynomial of degree 2. The mapping must be preferably perform on both the order definition frame (to compute the map) and the science frame (to compute the offset of the map).
- ***wind_scat.m*** - Estimates the scattered light and sky emission on the CCD by performing inter-order measurements and interpolation. The procedure obviously needs to know the order locations.
- ***wind_x2d.m*** - Extract a two-dimensional spectrum from each order. This step can be performed without interpolation in the cross-dispersion direction (nearest pixel value), or by selecting a linear, spline, or piecewise cubic Hermite interpolation.
- ***wind_lcurv.m*** - The function estimates the slit image curvature by using an optimum weight algorithm. The number of items in the Taylor serie expansion can be set from 2 (*i.e.* Connes algorithm) to 4, that corresponds to a "Taylor" parameter values equals to 1, 2 or 3 in the procedure.
- ***wind_wave.m*** - The procedure fits the line positions given by the calibration table with a polynomial of degree 2, in order to compute the dispersion solution.
- ***wind_doppler.m*** - The procedure is similar to wind_curv.m but computes Doppler shits. Then, the dispersion relation (polynomial coefficients previously computed) is required. The value of the "Taylor" parameter can be set to 1 or 2 (3 hasn't been implemented yet).
- ***wind_multidop.m*** - This function allows one to compute spatial velocity changes. It uses the same optimum weight algorithm than wind_doppler.m but considers adjecent peers of spectra (reference + shifted) along the slit. The number of peers around the slit center is tunable.

  - ***wind_ vmax.m*** - The procedure allows the retrieval of the maximum Doppler shift along the planet's disc, assuming an East-West symmetry which can be set be a parameter (3σ for instance). Note that this procedure does not suit quickly-rotating large target bodies such as Saturn.
  - ***wind_ plot.m*** - Plot the results and export the corresponding postscript and ".jpg" files. The figures consist in estimates of the scattered light, the slit image curvature, the Doppler shifts relative to the target's center, the differential Doppler shifts at different regions and the irradiance profile.

- **Extra** - Contains additional procedures that are not required to reduce the data but can be useful. For instance:

  - ***showmap.m*** plots in the same figure a frame (science/flat field/lamp) and the order map. In addition, it can plot a window around the order locations, in order to find the best width for the extraction window (especially for Saturn). The known bad pixels are also plotted,
  - ***slopefit.m*** fits the slope in the central part of the "velocity curve" provided by *wind_ doppler.m*, by using a linear regression. The number of central values is tunable. Note that is better to use *wind_ multidop.m* to measure such a quantity.
  - ***s2fried.m*** Converts a seeing angle value (in arcsec) into a Fried parameter value (in meter). It takes the wavelength and the elevation angle into account.
  - ***modelfun.m*** whose procedure performs simulations of the measurements.
  - ***makeccdmask.m*** creates a UVES (red arm) CCD bad pixel mask.
  - ***makeesp.m*** creates a set of synthetic shifted spectra, the central spectrum can be selected as the reference for instance. It is useful to test the optimum weight algorithm.

- **Tools** - Auxiliary scripts that can be used for intermediate calculations, such as:

  - ***cosmic.m*** is responsible to detect cosmic hits by using median filtering.
  - ***findsym.m*** that finds the symmetry center (x0, y0) of a data.
  - ***getkval.m*** that gets the keyword value in a fits header.

- ***maskline.m*** makes a mask to remove unwanted lines or special features.
- ***orderDiff.m*** computes the relative distance between the lamp center and the target center.
- ***polyfit3.m*** fits a polynomial of degree N to the data in a least-squares sense.
- ***sumshift.m*** makes the sim of Doppler shifts assuming a $1/\sigma^2$ weight.

- **DataBaseSat** - This is one of the most important folders. It gathers all the data retrieved from the observations and it is organized according to the type of files (as seen in figure 4.36). For each day of observations we have:
  - a set of 5 *bias* frames;
  - a set of 5 *flat field* frames;
  - 1 *lamp* frame;
  - 1 *order definition* frame;
  - 1 *science* frame;
  - a set of *viwer* frames (one for each position of the UVES slit, depending on the day of observations);
  - 1 *wavelenght calibration* file containing 2 tables (for the Lower and Upper CCDs);

  and a generic *mask* frame.

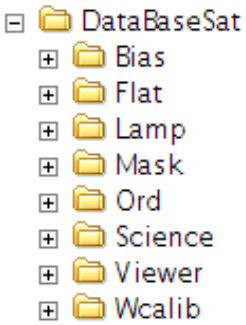

Figure 4.36: Organization structure of the DataBaseSat folder containing the input files.

- **Scripts Venus** - Original scripts used to study the dynamics of Venus atmosphere, on which the modifications/adaptations were made.

- **Current Version** - Adapted scripts which drive the overall processing by selecting a list of data reduction steps. The adaptation of the scripts was a step-by-step procedure, so the previous versions were stored in folders "Version 1", "Version 2" and "Version 3".

  - ***obsDatabase.m*** - Created database which contains all the required data in order to process the observations (the path of the data, some instrument settings, target's diameter, ...)
  - ***wind_ saturn.m*** - This is the function that is called from the MATLAB command window. It sets the directory input and output paths, loads the database and runs the data reduction (done by wind_check_sat.m and wind_main.sat) for the selected observations.
  - ***wind_ main_ sat.m*** - This procedure is the core of the data reduction since it defines which steps must be performed sequentially: import files, map the *echelle* order locations, estimate scattered light, extract spectra, compute the Doppler shifts and finally plot the results.

- **OutputDay** - We have created 5 folders, one for each observation day, were the images computed by *wind_ saturn.m* and *wind_ main_ saturn.m* are saved.

- **TemoFileswind** - Folder were are stored the temporary files created trough the processes of the main and core scripts.

- **windsatext20cut700** - Folder in which all the *.dop* (in *.mat*, *.eps* and *.jpg* formats are stored from *wind_ saturn.m* and used in the main script present in "Satvelocity" folder.

- **Satvelocity** - Set of scripts responsible for the second phase of data reduction in which, based on the *.dop* files, the position of slit relative to the sub-earth point and the coordinates of each pixel of the slit's active window, compute the CCD's velocities as a function of the local time.

  - ***ventoSatmed.m*** - Loads the data base and the .dop files created previously to compute the de-projection factor for every pixel of the active window and make plots of:

- the velocities and Doppler shifts from the center of the slit as a function of the pixels; the position of the slit on the planet's view at the observations;

- the Doppler shifts from the center as a function of the local time;

- the Doppler wind velocities of both MIT and EEV CCD's (after the de-projection factor has been applied) as a function of the local time;

- the comparison and differences between the values above and the modelizations made for each slit based on the best data from the *state of the art*;

- the average (MIT and EEV) Doppler wind velocity as a function of the local time.

  - ***convolveSat4h.m*** - script called at the beginning by *ventoSatmed.m* in order to obtain the latitude, local time and the de-projection factor for each pixel and plot the slit's position on the planetary disk.

  - ***getlatlon.m*** - function called by *convolveSat4h.m* that calculates the latitude and "longitude" (local time) of the position of a given pixel.

- **OutputVentos** - Folder in which ***ventoSatmed.m*** saves the computed images for the initial case, where we used the data from all the pixels of the active window of the slits.

- **OutputVentos2** - Folder in which ***ventoSatmed.m*** saves the computed images for the reduced active window case.